# Sulfide enrichment at an oceanic crust-mantle transition zone: Kane Megamullion (23°N, MAR)

**Jakub Ciazela[1,2,3*], Juergen Koepke[1], Henry J.B. Dick[4], Roman Botcharnikov[1,5], Andrzej Muszynski[2], Marina Lazarov[1], Stephan Schuth[1], Bartosz Pieterek[2], Thomas Kuhn[6]**

[1] *Institut für Mineralogie, Leibniz Universität Hannover, Callinstr. 3, 30167 Hannover, Germany*

[2] *Institute of Geology, Adam Mickiewicz University, ul. Bogumiła Krygowskiego 12, 61-680 Poznań, Poland*

[3] *Space Research Center, Polish Academy of Sciences, ul. Kopernika 11, 51-622 Wrocław, Poland*

[4] *Department of Geology and Geophysics, Woods Hole Oceanographic Institution, MS #8, McLean Laboratory, Woods Hole MA 02543-1539, USA*

[5] *Institute für Geowissenschaften, Johannes Gutenberg Universität Mainz, J-J-Becher-Weg 21, 55128 Mainz, Germany*

[6] *Bundesanstalt für Geowissenschaften und Rohstoffe, Stilleweg 2, 30655 Hannover, Germany.*

** corresponding author: jc@cbk.pan.wroc.pl, phone: +48 71 3378 094, fax: + 48 71 372 93 72*

**KEYWORDS*:***

Crust-mantle boundary, sulfides, chalcophile elements, melt-mantle interaction, oceanic core complexes

**ABSTRACT:**

The Kane Megamullion oceanic core complex located along the Mid-Atlantic Ridge (23°30’N, 45°20’W) exposes lower crust and upper mantle directly on the ocean floor. We studied chalcophile elements and sulfides in the ultramafic and mafic rocks of the crust-mantle transition and the mantle underneath. We determined mineralogical and elemental composition and the Cu isotope composition of the respective sulfides along with the mineralogical and elemental composition of the respective serpentines. The rocks of the crust-mantle transition zone (i.e., plagioclase harzburgite, peridotite-gabbro contacts, and dunite) overlaid by troctolites are by one order of magnitude enriched in several chalcophile elements with respect to the spinel harzburgites of the mantle beneath. Whereas the range of Cu concentrations in spinel harzburgites is 7-69 ppm, the Cu concentrations are highly elevated in plagioclase harzburgites with a range of 90-209 ppm. The zones of the peridotite-gabbro contacts are even more enriched, exhibiting up to 305 ppm Cu and highly elevated concentrations of As, Zn, Ga, Sb and Tl. High Cu concentrations show pronounced correlation with bulk S concentrations at the crust-mantle transition zone implying an enrichment process in this horizon of the oceanic lithosphere. We interpret this enrichment as related to melt-mantle reaction, which is extensive in crust-mantle transition zones. In spite of the ubiquitous serpentinization of primary rocks, we found magmatic chalcopyrites [$CuFeS_2$] as inclusions in plagioclase as well as associated with pentlandite [$(Fe,Ni)_9S_8$] and pyrrhotite [$Fe_{1-x}S$] in polysulfide grains. These chalcopyrites show a primary magmatic $\delta^{65}Cu$ signature ranging from -0.04 to +0.29 ‰. Other chalcopyrites have been dissolved during serpentinization. Due to the low temperature (<300 °C) of circulating fluids chalcophile metals from primary sulfides have not been mobilized and transported away but have been trapped in smaller secondary sulfides and hydroxides. Combined with the Cu deposits documented in the crust-mantle transition zones of various ophiolite complexes, our results indicate that the metal enrichment, increased sulfide modes, and potentially formation of small sulfide deposits could be expected globally along the petrological Moho.

## 1. INTRODUCTION

Sulfide ores are the major source of many base and precious metals (Ag, As, Au, Bi, Cd, Cu, Ge, In, Mo, Pb, Rh, Se, Tl, Zn; U.S. Geological Survey, 2016). Industry demand (e.g., building construction, electrical components, transportation equipment) for these metals is growing dramatically, which is causing surface reserves to shrink. To estimate the subsurface resources of the above metals, it is necessary to understand the distribution of sulfides throughout the lithosphere.

The estimated mode of sulfide in the primitive mantle is between 0.07 vol.% (Fellows and Canil, 2012) and 0.10 vol.% (Harvey et al., 2016). Sulfides melt in relatively low temperatures during partial melting of the mantle (Hart and Gaetani, 2006; Zhang and Hirschmann, 2016). The depleted mantle is thus poorer in sulfides than the primitive mantle (Lee et al., 2012). The crust in return is enriched in sulfides with respect to both the depleted and primitive mantle (Lorand et al., 2013; Patten et al., 2013; Harvey et al., 2016).

On the other hand, many studies performed over the last few decades indicate that a reaction between the mantle and melt ascending through the lithosphere is another magmatic process that strongly affects sulfide distribution (Lorand and Luguet, 2016). In a reaction of melt with a depleted mantle, the melt, typically enriched with sulfur and chalcophile elements, impregnates the mantle with sulfides. This process belongs to melt refertilization processes (e.g., Niu, 2004). Examples of melt refertilization involving sulfides have been found in mantle xenoliths (Wang et al., 2009; Michalak and Nowak, 2010; Chen et al., 2014; Bukała et al., 2015), orogenic peridotites (Garuti et al., 1984; Lorand, 1989a; 1989b), and abyssal peridotites (Rehkämper et al., 1999; Luguet et al., 2003). Although melt-mantle reaction may occur deep within the mantle (Kelemen et al., 2000), it seems to be most prominent at the crust-mantle boundary (Jousselin et al., 1998; Kelemen et al., 2000). Typical products of such reactions are dunites (Dick, 1977a; 1977b; Kelemen, 1990; Jousselin et al., 1998; Braun and Kelemen, 2002), and often olivine-rich troctolites (Suhr et al., 2008; Drouin et al., 2009; 2010; Sanfilippo et al., 2013; 2015) or plagioclase peridotites (Dick, 1989; Rampone et al., 1997; Piccardo et al., 2007; Tamura et al., 2008; Dick et al., 2010). These rocks typically form the crust-mantle transition zone, which can be from several meters to over 2 km thick (Karson et al., 1984; Benn et al., 1988; Boudier and Nicolas, 1995; Canales et al., 2000; Nicolas et al., 2000; Bosch et al., 2004; Nedimović et al., 2005). It forms a heterogeneous zone between the lower crust and the upper mantle on a global scale. Due to extensive refertilization processes, the crust-mantle transition zone, and not the crust, could be the layer that is richest in sulfides in the entire lithosphere.

Unfortunately, little material from the crust-mantle transition zones is available. The crust-mantle transition on land is only accessible via ophiolites, which represent the remnants of the ancient oceanic lithosphere tectonically emplaced onto continental margins. In the northern part of the world's largest ophiolites in Oman, dunites of the Moho transition zone are often rich in igneous sulfides (Negishi et al. 2013). In addition, sulfide deposits of economic importance have been found in the crust-mantle transition zones of several ophiolites including Oman and Troodos (Panayiotou, 1978; Akinci, 2009; Begemann et al., 2010; Saalmann and Laine, 2014; 2015). The sulfide deposits, however, are seen as late secondary formations (Goettler et al., 1976). Whether or not primary sulfides had been formed may be unclear due to the ophiolites' complex history. Subduction-related processes with an additional period of magmatic activity (Dilek and Furnes, 2014), and post-emplacement supergene processes most likely overprint the original sulfide occurrence.

Alternatively, crust-mantle transition zones are exposed on the ocean floor. Although a typical thickness of the fast-spreading oceanic crust is 6-7 km (Klein, 2003), the slow-spreading oceanic crust is usually thinner by 2-4 km than the fast-spread oceanic crust (Nicolas, 1995; Cannat, 1996; Muller, 1997). In addition, the lower oceanic crust and mantle along slow-spreading ridges are often exposed on the surface of the ocean floor along detachment faults. Detachment faults are long-lived low-angle normal faults that form during waning periods of magmatism along slow-spreading ridges (Dick, 1981; Tucholke and Lin, 1994; Cann et al., 1997; Tucholke et al., 1998; for an overview see Ciazela et al., 2015). The footwall of a detachment fault that exposes the lower crust or mantle is defined as an oceanic core complex (OCC). Crust-mantle transition zones exposed on the ocean floor are well-documented in three OCCs. The most extensively sampled crust-mantle transition zone is located at the Kane Megamullion

OCC along the Mid-Atlantic Ridge (MAR; Dick et al., 2010). The other two are located at the Atlantis Bank along the Southwest Indian Ridge (SWIR; Dick et al., 2015) and at the Uraniwa Hills along the Central Indian Ridge (Sanfilippo et al., 2015; 2016). Ultramafic rocks in all the three OCCs are heavily serpentinized. Therefore, primary sulfide modes in the local rocks cannot be determined.

In this study, to trace the fate of primary sulfides we focus on chalcophile metals (Cu, Zn, As, Sb, Tl, Pb, Ga, Se, Ge, Bi, Ag, Au, Ni) and sulfur concentrations both in rocks and minerals of the Kane Megamullion crust-mantle transition zone (i.e., plagioclase harzburgite, peridotite-gabbro contacts, and dunite). We find a strong enrichment of most chalcophile elements within the crust-mantle transition zone. Using petrological indicators (i.e., inclusions in plagioclase, and pyrrhotite-chalcopyrite-pentlandite assemblages after monosulfides) and the Cu isotopic signature of chalcopyrites, we show that the observed enrichment of chalcophile elements was caused by a primary magmatic process.

## 2. GEOLOGICAL SETTING AND PETROGENESIS OF THE STUDIED SAMPLES

### 2.1. Geological setting

The Kane Megamullion OCC is located south of the Kane Fracture Zone (23°30’N, 45°20’W) on the MAR (Fig. 1). Between 3.3 Ma and 2.1 Ma, rifting caused the formation of a detachment fault at the base of the rift valley wall exposing a ~900 km$^2$-large plutonic footwall on the ocean floor west of the spreading axis at a depth of ~3 km below sea level. The OCC is 40 km long in a N-S direction and 23 km wide in a E-W direction (Dick et al., 2008). In conjunction with a dozen of smaller OCCs, the Kane Megamullion forms a triangular core complex terrain with one vertex at the Kane Fracture Zone – MAR inside corner, and the other two vertices ~150 km to the west along the transform fault, and 100 km to the south along the MAR (Cann et al., 2015). Ocean Drilling Program (ODP) Expeditions 109 and 153 have drilled in seven sites (i.e., 669-670, and 920-924, respectively) in the eastern part of this terrain close to the MAR (Fig. 1), yielding mostly peridotite and gabbro (Detrick et al., 1988; Cannat et al., 1995).

The predominance of plutonic rocks in the Kane Megamullion is well documented over the entire complex by sampling the detachment fault surface as well as outward facing high-angle normal fault scarps and slide-scar headwalls (Tivey et al., 2004; Dick et al., 2008; Dick et al., 2010; Hansen et al., 2013). Two independent gabbro bodies are located in the northern and southern parts of the complex: one at Babel Dome and one at the Adam-and-Eve Dome complex (Canales et al., 2008). These two gabbro bodies are divided by a peridotite massif composed of the Abel and Cain Domes in the central part of the complex (Dick et al., 2008; Xu et al., 2009). The southern gabbro body lies above troctolites, dunites, and harzburgites (Dick et al., 2008). This suite of rocks represents the oceanic crust-mantle transition zone that we investigate here.

### 2.2. Petrogenesis of the studied samples

In this study, we compare the residual mantle samples represented by spinel harzburgites with the melt-modified mantle samples represented by plagioclase peridotites, mantle-gabbro contacts and dunites (Fig. 2). The detailed petrographic description of these rocks is provided by Dick et al. (2010). Plagioclase-free spinel harzburgites are typical serpentinized abyssal peridotites. They are similar to protogranular harzburgites from many ophiolites with an average pyroxene grain size of ~4 mm. Most spinels show Cr-numbers (molar Cr/(Al+Cr) x 100) of 28 to 35 indicating a degree of mantle melting on a level of 11-14% (Dick et al. 2010).

The plagioclase harzburgites represent former residual mantle subsequently impregnated by a trapped or transient mid-ocean ridge basalt (MORB)-like melt. About 14% of the Kane Megamullion harzburgites contain accessory plagioclase but modal plagioclase is only <2%. Considering that normative plagioclase in MORB is between 55% and 60%, only <4% of trapped melt would be needed to yield peridotites with <2% plagioclase. Such a small amount of trapped melt could not, however, explain the low forsterite (Fo) content (down to 78.6) of the olivine rims in these plagioclase peridotites. Transient and not trapped melt are thus more likely to form the plagioclase peridotites (Dick et al., 2010).

Peridotite-gabbro contacts represent sections of peridotite within 2 cm from margins of gabbroic or troctolitic veins. They represent yet higher degree of melt modification than the plagioclase harzburgites as displayed by visible halos (Fig. 2) and low Fo contents on olivine rims (Dick et al., 2010). Our dunites are also interpreted as products of melt-rock reaction as in ascending melts the phase field of olivine expands at the expense of pyroxene (Dick et al., 2010).

Local hydrothermal products discussed in Section 5.4 are composed of either hydrothermally altered breccias from mounds, or chalks associated with hydrothermal Fe-Mn precipitates. Both are products of mostly low-temperature (<100°C), or occasionally higher-temperature (>100°C) hydrothermal venting (Kaim et al., 2012; Tucholke et al. 2013). In addition, some hydrothermal products are covered by hydrogenous Fe-Mn precipitates on their surface (Tucholke et al., 2013).

## 3. METHODS

### 3.1. Sample collection

The Kane Megamullion OCC was investigated with extensive magnetic, bathymetric, and sampling surveys during R/V Knorr Cruise 180, Leg 2 (Tivey et al., 2004; Dick et al., 2008). Samples were collected by 25 dredges, and 8 Jason II ROV dives. A total of 2,666 kg of rock were recovered, mostly comprising peridotite, dunite, gabbro, diabase, and basalt. A representative suite of 19 spinel harzburgites, 4 plagioclase harzburgites, 3 peridotite-gabbro contacts, 1 dunite, and 1 olivine websterite (Table 1) were selected from the headwalls of a large landslip and high-angle normal faults that cut below the detachment fault damage zone.

### 3.2. Whole-rock analyses

The major elements were analyzed with X-ray Fluorescence (XRF) spectroscopy at the Bundesanstalt für Geowissenschaften und Rohstoffe (BGR) in Hannover, Germany. To fuse beads for analysis, 1 g of sample powder and 5 g $LiBO_2$ were mixed and melted for 20 min at 1200°C. The fused beads were analyzed with a wavelength dispersive PANalytical AXIOS X-ray spectrometer equipped with a rhodium X-ray tube. More than 100 international standards are used for the calibration of the X-ray spectrometer. Data get automatically internally corrected for matrix effects and spectral interferences using the de Jongh method. The relative uncertainty is in a range of 1-2 relative percent. The volatile concentrations were estimated as loss-on-ignition (LOI) by heating the samples in a muffle furnace for 10 min at 1030°C (Table 1).

An ELTRA CS 800 carbon-sulfur analyzer (Institut für Mineralogie, Leibniz Universität Hannover) was used to determine the sulfur concentrations. The analytical procedure is described by Lissner et al. (2014). Six to eight blanks were analyzed per analytical session, and the means of the blanks that were measured before and after a sample measurement were subtracted from the results. The limit of detection calculated as three standard deviations of the blank is 6 ppm S. Six sample replicates indicate an average precision of 11.8% (double relative standard deviation; 2 RSD) ranging from 1-5% in sulfur-rich samples to 20-30% in sulfur-poor samples. Sixteen analyses of the 033-1 reference material (Bundesanstalt für Materialprüfung, Germany) yielded a sulfur concentration of 217 ± 12 ppm. This implies an external precision of 11.1% (2 RSD). Given the certified sulfur content of the 033-1 reference material is 215 ± 22 ppm (2 SD), our sulfur data are marked by a high analytical accuracy and improved precision.

The concentrations of chalcophile elements were determined by a combination of instrumental neutron activation analysis (INAA), and inductively coupled plasma mass spectrometry (ICPMS) techniques, both conducted by Activation Laboratories Ltd., Ontario, Canada with the Ultratrace 5 analytical package. The ICPMS equipment used for this package was a Perkin Elmer-SCIEX ELAN 6000. Before the analysis, the samples were digested in a sequence of perchloric, hydrofluoric, hydrochloric, and nitric acids. Gold is expected to be distributed heterogeneously, which is described as the “nugget effect” (Lorand et al., 2010). To provide reliable results for Au, up to 30 g of powder was used for INAA. Standards and measurement conditions are described in the Ultratrace 5 - Total Digestion - ICPMS, INAA subsection of the Methods section of the Actlab website (www.actlabs.com). Detection limits are given in Table 2.

### 3.3. Electron microprobe analysis

The major element composition of primary and secondary minerals were determined using a Cameca SX100 EPMA at the Institut für Mineralogie, Leibniz Universität Hannover, Germany. Standards include native metals (Cu, Co), pyrite (S and Fe), wollastonite (Si and Ca), albite (Na), orthoclase (K), and synthetic NiO, $Cr_2O_3$, $Al_2O_3$, $TiO_2$, $Fe_2O_3$, MgO, and $Mn_3O_4$. A sample current of 15 nA and an acceleration voltage of 15 kV were used for all analyses. Raw data were corrected using the standard “PAP” procedure (Pouchou and Pichoir, 1991). A focused beam was used for primary minerals. A defocused beam of 10 µm was applied to serpentines as was proposed in several studies of serpentines (e.g., Andreani et al., 2007, 5 µm; Kodolányi and Pettke, 2011, 10 µm). However, few analyses were performed with a focused beam and the results indicate no systematic difference using different beam sizes. A sample current of 200 nA and a dwelling time of 5 to 15 ms were used for X-ray mapping.

### 3.4. Laser Ablation - Inductively Coupled Plasma Mass Spectrometry

#### 3.4.1. Trace element microanalysis

For the trace element analyses, we used an Element XR (Thermo Scientific, Germany) fast-scanning sector field ICPMS coupled to a femtosecond laser ablation (fs-LA) system (Solstice, Spectra-Physics, USA) at the Institut für Mineralogie, Leibniz Universität Hannover, Germany. The laser unit operates in the deep UV at 194 nm and produces energy pulses of 70–90 mJ in the fourth harmonic. This ultrashort pulsed laser avoids elemental fractionation at the sample site and minimizes matrix effects (Horn et al., 2006; Horn and Von Blanckenburg, 2007; Horn, 2008; Albrecht et al., 2014). We limited the rate of oxide formation by tuning the ICPMS to a low ThO/Th (typically 0.25% for this study). The laser beam had a diameter of 60 µm for the standards and non-sulfides (when possible). Smaller beam diameters down to 5 µm were used for sulfides (Table A.1 in Appendix A). The repetition rate was 10 Hz for the standards and it was variable for the samples, typically 20-40 Hz for silicates and oxides, and 10-40 Hz for sulfides. Ablated particles were transported by He carrier gas. Then, Ar was admixed to the He carrier gas before entering the ICPMS unit. The NIST 610 reference material was used as an external standard. The $SiO_2$, Ni, and Cu concentrations of the minerals determined by EPMA were used as internal standards for quantification. For data reduction, including drift correction, we used the Matlab-based SILLS program (Guillong et al., 2008).

### 3.4.2. Copper isotope microanalysis

The $^{65}Cu/^{63}Cu$ ratio of the samples and reference materials were measured using the aforementioned fs-LA system coupled to a Neptune Plus (Thermo Scientific, Germany) multi-collector-ICPMS. Measurements were performed in low-resolution mode. In addition to the two Cu isotopes, four Ni isotopes ($^{60}Ni$, $^{61}Ni$, $^{62}Ni$ and $^{64}Ni$) were simultaneously measured. For the Ni source, we used 1 ppm Ni NIST SRM 986 standard solution, which was added via a quartz glass spray chamber (double pass Scott design) and a PFA micro-flow nebulizer (uptake rate ~100 µl/min). The measured $^{62}Ni/^{60}Ni$ was used for the internal instrumental mass bias correction. For a detailed description, see Lazarov and Horn (2015).

Samples have been measured against the NIST SRM 976 Cu-metal standard and are reported as $\delta^{65}Cu$ (i.e., deviation $^{65}Cu/^{63}Cu$ from NIST SRM 976 expressed in ‰) . In addition, the cpy2 chalcopyrite from Lazarov and Horn (2015) was measured as an unknown to verify if the laser energy was set to the appropriated level and if the obtained $\delta^{65}Cu$ values agree with the values for the solution reported by Lazarov and Horn (2015). All reference materials and samples were ablated along lines. A spot diameter of 40 µm and laser repetition rates of 5 Hz and 10 Hz for the NIST SRM 976 and cpy2, respectively, resulted in signal intensities of ~10 V on mass 65. However, the Kane Megamullion chalcopyrites are very small and need to be measured with aperture sizes of 10 to 20 µm. Consequently, the laser repetition rates were increased to a maximum of 100 Hz during the sample measurements to match the signal intensities between the reference materials and samples. Still some of the sample measurements were performed at low Cu intensities (~1 V on $^{65}Cu$). Molecular interferences induced by a sulfide matrix such as $(^{32}S^{33}S)^+$ or $(^{32}S^{16}O^{17}O)^+$ on $^{65}Cu$ can be significant at such low intensities. The cpy2 standard was therefore measured with similarly low Cu intensities four times. The resulting $\delta^{65}Cu$ values matched within error the $\delta^{65}Cu$ values obtained by measuring the cpy2 standard with higher intensities (Table 3).

Even at low Cu signal intensities, the cpy2 standard showed a double relative standard error (2 RSE) <0.1‰ (Table 3). Due to the small sizes of chalcopyrites in the samples, and a high laser-repetition rate, an individual analysis consisted of only ~20 cycles with a cycle integration time of 1.05 s. Hence, the 2 RSE of $\delta^{65}Cu$ attains a maximum of 0.18‰ in our study. The overall RSE for samples is calculated by the propagation of the within-run RSEs of a sample and its two bracketing standards (see also the caption for Table 3).

## 4. RESULTS

### 4.1. Petrographic characteristic of sulfide assemblages

At the Kane Megamullion OCC, peridotites are partially to fully serpentinized, and primary sulfides (chalcopyrite [$CuFeS_2$], pyrrhotite [$Fe_{1-x}S$], and pentlandite [$(Fe,Ni,Co)_9S_8$]) are commonly replaced by secondary sulfides (secondary pentlandite, pyrite [$FeS_2$], violarite [$FeNi_2S_4$], millerite [NiS], godlevskite [$Ni_9S_8$], and heazlewoodite [$Ni_3S_2$]). Primary sulfides are thus rare and only occur in the melt-modified mantle rocks. Pyrrhotite is the predominant primary sulfide (Table 4). When chalcopyrite and primary pentlandite occur they coexist with pyrrhotite. Chalcopyrite is sometimes altered to a Fe-Cu hydroxide, and primary pentlandite is occasionally weathered to violarite. In other assemblages, pentlandite occurs as a secondary phase along with heazlewoodite, godlevskite, and millerite. These secondary assemblages are also rare in the depleted harzburgites and more abundant in the melt-modified mantle rocks. In the three spinel harzburgites investigated in thin sections we found only two sulfide grains (Table 4).

Thin sections of samples 21-9 and 19-11 have linear contact zones between peridotite and gabbro veins (2 mm and 15 mm wide zone, respectively; Fig. 3). By using reflected light microscopy, we have estimated the abundance of large (>40 µm) sulfides in these contact zones to be ~3.3 grains/$cm^2$. The abundance decreases to ~0.3 grains/$cm^2$ in the background peridotite (Fig. 3a). No large sulfide grains occur in the gabbro veins. The abundances of medium-sized sulfides (10-40 µm) are ~13 grains/$cm^2$ for the contact zone (orange boxes II and III on Fig. 3a), ~4 grains/$cm^2$ for the background peridotite (orange box I on Fig. 3a) and ~2 grains/$cm^2$ for the gabbro veins (orange box IV on Fig. 3a). In addition, we X-ray mapped three 20-to-60-$mm^2$-large areas (one is presented on Fig. 3b-c) crossing the contact zones in both thin sections. The S distribution map (Fig. 3b) shows that <10-µm sulfides are yet more abundant than the medium-sized sulfides. The main crystallization front of all the sulfides is ~1 mm wide, and is located on the margins of the contact zones adjacent to the mafic veins (Fig. 3b).

### 4.2. Bulk-rock major-element compositions

Most of the peridotites studied here are heavily serpentinized, which is often the case for abyssal peridotites (Luguet et al., 2003; Boschi et al., 2006; Miller, 2007; Klein and Bach, 2009; Morishita et al., 2009). This is also reflected in a high LOI content of our peridotites (Table 1) ranging from 4.9 to 16.2 wt% (Table 1). Harzburgite $SiO_2$ contents vary between 37.6 and 42.2 wt%. The Mg-number, defined as molar $Mg/(Mg + Fe) \times 100$, spans a narrow range of 87 to 90 for most of the harzburgites. Our LOI values, $SiO_2$ contents, and Mg-numbers are similar to their ranges for abyssal peridotites known from the literature, which are 5-15 wt%, 34-46 wt%, and 0.88-0.92, respectively (Luguet et al., 2003; Boschi et al., 2006; Paulick et al., 2006; Morishita et al., 2009).

The peridotite-gabbro contacts show high modal iron oxides resulting in high bulk-rock FeO contents and low Mg-numbers (42-64) in comparison to typical mantle values. The $Al_2O_3$, CaO and $P_2O_5$ contents are elevated in the peridotite-gabbro contacts compared to the spinel harzburgites (Table 1, Fig. 4). Such $Al_2O_3$, CaO and $P_2O_5$ enrichments are not evident in the bulk plagioclase harzburgites (Table 1, Fig. 4), although they are observed in the plagioclase harzburgite serpentines *in situ* (Table B.1 in Appendix B). This irregular enrichment of $Al_2O_3$, CaO, and $P_2O_5$ in the plagioclase peridotites is probably due to inhomogeneous melt percolation and/or post-magmatic serpentinization (Section 5.5).

### 4.3. Bulk-rock trace-element contents

The chalcophile element contents of the serpentinized spinel harzburgites (Table 2) are in the compositional range of primitive mantle estimates (Sun, 1982; McDonough and Sun, 1995) and most fresh peridotites from orogenic and ophiolitic massifs (Garuti et al., 1984; Lorand, 1989a; Lorand, 1991; Lorand et al., 1993) (Fig. 5). Notably, our chalcophile element contents are higher than those found in peridotites from the Atlantis Massif OCC. Boschi et al. (2006) reported average concentrations of 13 ppm Cu, 36 ppm Zn, and 2 ppm Ga for 24 serpentinized peridotites from the Atlantis Massif OCC. These values are by 54%, 57% and 25% lower than the average concentrations of 28 ppm Cu, 84 ppm Zn and 2.5 ppm Ga in the Kane Megamullion serpentinized spinel harzburgites. The Atlantis Massif peridotites have been, however, highly deformed in the detachment fault damage zone. The corresponding peridotites from the damage zone of the Kane Megamullion detachment fault are also depleted in chalcophile elements, with a mean Cu concentration of 15 ± 5 ppm (2 RSE). Due to tectonically induced alteration, the latter peridotites are considered as non-representative and discarded from further discussion in this study. The serpentinized depleted spinel harzburgites from the 15°20’ Fracture Zone along the MAR also show lower Cu content (4 ppm; Marchesi et al., 2013) compared to the Kane Megamullion serpentinized depleted spinel harzburgites. In this case, however, the reason for the low Cu concentration is the higher degree of partial melting (15-20%) in the 15°20’ Fracture Zone harzburgites (Marchesi et al., 2013).

The mean sulfur concentration of 184 ppm in the Kane Megamullion spinel harzburgites is within the sulfur content range (150-330 ppm) of fresh orogenic peridotites. The Kane harzburgites, however, show a broader range of 32 to 561 ppm S (Table 2). In addition, harzburgite 114-9, which has been further altered to talc, falls below this range with no detectable sulfur.

All chalcophile elements except for Bi and Ni are enriched in the melt-modified peridotites compared to the spinel harzburgites representing depleted mantle. This difference is most pronounced for Cu and Zn (Table 2; Fig. 4; Fig. 6). The mean concentrations of Cu and Zn are 294 and 354 ppm in the peridotite-gabbro contacts, and 131 and 91 ppm in the plagioclase harzburgites, respectively. In contrast, spinel harzburgites contain only 28 ppm Cu and 84 ppm Zn (Table 2, Fig. 4). The depleted harzburgites contain on average more Ni (1631 ppm), than the melt-modified mantle (1360 ppm), even if the Ni-poor brecciated dunite 113-41 is not taken into account (Fig. 4). The low Ni content here could have been caused by veining related to brecciation of this dunite in a calcium carbonate matrix. Miller et al. (2011) have demonstrated that limestone systems are effective at removing Ni from circulating fluids. Therefore, Ni from 113-41B could have been lost to the calcium carbonate during fluid circulation. We determined that the Ni concentration in the associated calcium carbonate was 89 ppm Ni, which matches enhanced Ni contents (25-740 ppm) from ultramafic-hosted carbonates from the equatorial MAR (Bonatti et al., 1974). In contrast, marine limestones not associated with ultramafic rocks contain only 3 to 20 ppm Ni (Barber, 1974).

In addition to the rocks of the crust-mantle transition zone, we have determined chalcophile element contents in eight local seafloor hydrothermal products previously documented by Tucholke et al. (2013). These contain up to 3500 ppm Cu, 1150 ppm Zn, 795 ppm Pb, and 570 ppm As (Table C.1 in Appendix C), and are further discussed in Section 5.4

### 4.4. Major-element compositions of sulfides

Sulfur, Ni, Fe, Cu and Co contents of pentlandite, millerite, godlevskite, and heazlewoodite, violarite, chalcopyrite, pyrrhotite, and pyrite have been measured using EPMA. The pentlandite is the only Kane Megamullion sulfide mineral that occurs both in the depleted and the refertilized mantle. Notably, the refertilized mantle pentlandites are Co-rich with respect to an average pentlandite (0.6 wt% Co; see Table D.1 in Appendix D). The average Co content is 1.8 wt% for the pentlandites from the plagioclase harzburgites and 1.9 wt% for the pentlandites from the peridotite-gabbro contacts, with one pentlandite containing 8.1 wt% Co. The Ni/(Ni+Fe) molar ratio is typically between 0.44 and 0.51 (90% of the population), but the full range spreads from 0.34 to 0.59. A similar range of the Ni/(Ni+Fe) ratio (0.38-0.58) was observed by Misra and Fleet (1974) ins pentlandites associated with pyrrhotite and chalcopyrite in several magmatic sulfide deposits in Canada. Interestingly, many of the pentlandites showing extreme Ni/(Ni+Fe) values occur in the sample 21-7 peridotite-gabbro contact.

In addition, we observed a gradient of sulfide Ni-content in the group of pentlandites, heazlewoodites, godlevskites, and millerites located across the peridotite-gabbro contact in sample 21-9 (Fig. 7a). Two sulfides from the gabbro side of the contact contain 69 wt% Ni, seven sulfides from the middle of the contact zone contain between 32 and 39 wt% Ni, and five sulfides from the peridotite side of the contact 31 to 32 wt% Ni. The clear Ni gradient is thus observable, from higher-Ni sulfides in the gabbro to lower-Ni sulfides in the peridotites.

Altogether four violarites, all replacing pentlandites, have been found in two of the samples studied in thin sections. Three violarites occur in olivine websterite 5-31B, and show a stoichiometric Ni/(Fe+Ni) ratio of 0.66-0.69 and a relatively low Co content (0.5-0.6 wt%). One violarite occurs in the sample 21-7 peridotite-gabbro contact, showing a higher Co content (1.2 wt%) and a non-stoichiometric Ni/(Fe+Ni) molar ratio of 0.52. Notably, the violarites retained the compositional features from the original pentlandites since the refertilized peridotite pentlandites also show a non-stoichiometric Ni(Fe+Ni) ratio, and higher Co contents than the depleted peridotite pentlandites.

The Kane Megamullion chalcopyrites show nearly stoichiometric (i.e., 0.47-0.52) ratios of Cu/(Cu+Fe). The metal/sulfur ratio is however slightly higher than the stoichiometric ratio of 1 (Table D.1 in Appendix D). Here, the Ni contents range from 0.0 to 3.9 wt%. The highest Ni contents are likely caused by fine-scale intergrowths of associated pentlandite (e.g., Fig. 8b). Nickel was also detected in 14 of 75 analyzed pyrrhotites with a maximum of 0.6 wt%, where neither Cu nor Co are present on a wt% level. Pyrrhotites exhibit a typical metal/sulfur ratio of 0.83 to 1.00. Few outliers with 1.02 and 0.76 have also been found.

### 4.5. Chalcophile element contents of sulfides

We measured Ni in pyrrhotite and chalcopyrite, Cu in pyrrhotite and Ni sulfides, as well as Zn, Ga, Ge, As, Se, Ag, Cd, Sb, Te, Tl, Pb and Bi in all the sulfides using fs-LA-ICPMS (Table A.1 in Appendix A; Fig. 9).

Pentlandite is the only sulfide phase that is abundant both in the depleted and the refertilized portions of the mantle. Notably, pentlandites from the refertilized peridotites are enriched in chalcophile elements with respect to the pentlandites from the depleted peridotites (Fig. 9c). For example, Cu contents are typically <200 ppm in the depleted peridotites pentlandites and up to ~1000 ppm in the pentlandites from peridotite-gabbro contacts. Two pentlandites from the peridotite-gabbro contact show even >2000 ppm Cu. We think, however, that these Cu contents were enhanced by small chalcopyrites that were hidden under the surface of the pentlandites and have been ablated together. Elevated Zn contents have also been found in these pentlandites (54 and 151 ppm). Otherwise, the Zn content is very low in pentlandites, typically below 35 ppm. One pentlandite from a peridotite-gabbro contact, however, contains 512 ppm Zn, which is likely a value inherent to this pentlandite and not an intergrowth. Arsenic is typically below 35 ppm in the depleted peridotite pentlandites. Some grains from peridotite-gabbro contacts, however, contain up to 1028 ppm As. The Pb concentrations in pentlandites are variable but generally much higher than those in the pyrrhotites and chalcopyrites, exceeding 20 ppm in many grains, especially in the peridotite-gabbro contact from sample 21-9. Pentlandites from the spinel harzburgites typically contain between 4 and 31 ppm Te. Two sulfides from a peridotite-gabbro contact have elevated Te concentrations (49 and 139 ppm). Antimony is generally high in the pentlandites from the peridotite-gabbro contact. However, due to the small sizes of these pentlandites we were able to determine Sb concentrations (3.2, 4.2, and 12 ppm) in only three grains. Outside the contact zone, Sb is barely distinguishable from the detection limit.

In addition, we analyzed in detail the gradient of sulfide Cu content in the nickeliferous sulfides (pentlandite, heazlewoodite, millerite, and godlevskite) from sample 21-9 in relation to their distribution around the peridotite-gabbro contact. Notably, the sulfide Cu contents are related to the location of sulfides and the Ni concentrations (Fig. 7b). Two higher-Ni sulfides located on the gabbro side of the contact contain only 1 ppm Cu. Seven sulfides from the middle of the contact zone, containing between 32 and 39 wt% Ni, show high Cu concentrations of 71 to 405 ppm. Five lower-Ni sulfides from the peridotite side of the contact contain 5 to 14 ppm Cu. Therefore, a clear "Cu peak" is observable in the middle of the contact zone, associated with the intermediate Ni concentrations.

Pyrrhotite and chalcopyrite occur only in the refertilized peridotites. In pyrrhotites, Cu is present as a trace element with a median of 61 ppm and a maximum of 1268 ppm. Zinc and Se are also abundant, but never above 100 ppm. Thallium is an element typical for pyrrhotite (Table A.1 in Appendix A; Fig. 9), and detectable in most of the grains, typically on a level of 0.2 to 8 ppm. Lead is typically <1 ppm, but there are two pyrrhotite grains with values of 6.3 and 13 ppm. Arsenic is usually below the detection limit of ~5 ppm, but it is abundant in several grains with a maximum of 128 ppm.

Ten chalcopyrite grains have been measured for chalcophile element concentrations. The chalcopyrites are either adjacent to pentlandite or contain small intergrowths of pentlandite. Thus, no analysis returned a completely pure chalcopyrite signal. The least contaminated analysis still shows 1.6 wt% Ni (Table A.1 in Appendix A; Fig. 9). In comparison, only 0.2 wt% Ni have been detected by EPMA, which has a higher resolution than the LA technique. We can thus assume that approximately 1.4 wt% of the Ni derives from a pentlandite intergrowth. Nickel accounts for ~32% wt% in a typical pentlandite. These two assumptions imply that about 4% of the pentlandite and 96% of the chalcopyrite were consumed in this ablation crater. Such a minor amount of pentlandite can only affect the measured concentrations of Co (176 ppm) and perhaps Pb (3.0 ppm). The concentrations of Zn (859 ppm), Cd (13 ppm), Ga (3.8 ppm), Se (138 ppm), and Bi (1.5 ppm) in pentlandites are too low to effectively contaminate chalcopyrites. A value of 859 ppm for Zn well represents the spectrum of values obtained in the nine other chalcopyrite analyses (127, 362, 397, 881, 891, 1304, 1481, 1528, 1691 ppm). The Cd content of 13 ppm is also consistent with several other chalcopyrites that contain from 10 to 20 ppm Cd. The Cd concentration is, however, below the detection limits in few other grains.

### 4.6. Chalcophile element contents of matrix minerals

Chalcophile elements were measured in matrix minerals along a laser ablation profile composed of 18 parallel lines across the peridotite-gabbro contact 21-9T (Fig. 10). These lines were placed in order to avoid larger sulfides and oxide phases. They should thus mostly represent the silicate matrix (i.e., lizardite, antigorite, chrysotile, tremolite, chlorite, and prehnite, see Figs. 4, 6, and Figs. B.1 and B.2 in Appendix B).

The silicates of the peridotite-gabbro contact are enriched in most of the chalcophile elements with respect to the silicates of the peridotite and of the gabbro vein. This enrichment occurs in a narrow zone, as typically visible only in one of the laser ablation lines. Considering the distance between lines is ~250 µm, the width of this enrichment front is <500 µm. Most of the elements including Cu, Pb and Ge are enriched in the part of the contact zone directly abutting to the gabbro (Fig. 10). Cobalt and Au are most enriched ~500 µm away from the margin of the gabbro towards the peridotite, and Sb is the most enriched ~1 mm away from the gabbro towards the peridotite. Two exceptions are Zn and As. Zinc is enriched in the contact zone but on the gabbro side. Arsenic is largely enriched in two sites, one corresponding to the Cu, Pb, and Ge enrichment front, and one corresponding to the boundary between the chlorite and prehnite zones on the gabbro side of the contact (Fig. 10).

In addition to the LA-ICPMS profile through the matrix minerals of the peridotite-gabbro contact, we measured the chalcophile element contents in matrix minerals of the plagioclase and spinel harzburgites. Matrix minerals from the plagioclase peridotites contain more chalcophile elements with respect to the matrix minerals of the spinel harzburgites but less than the matrix minerals of the peridotite-gabbro contacts (Table B.1 in Appendix B and Fig. 11).

### 4.7. Isotopic composition of Cu in chalcopyrites

To further constrain the sulfide-forming processes we measured Cu isotopes in the largest four chalcopyrites in the 21-7 peridotite-gabbro contact. Independent of a variable analytical error (up to 0.18‰; Table 3), the $\delta^{65}$Cu signatures of all the four chalcopyrites fall in a range of -0.04 to +0.29‰ (Section 5.1).

## 5. DISCUSSION

### 5.1. Evidence for melt refertilization

The mean of 28 ppm Cu found in the Kane Megamullion spinel harzburgites is close to typical depleted mantle values (Garuti et al., 1984; Lorand, 1989a; 1991; Lorand et al., 1993; Fig. 5). The entire range for the spinel harzburgites investigated here is however from 7 to 69 ppm Cu. Such a large range of Cu concentrations is typical for mantle samples (Jagoutz et al., 1979; Niu, 2004), and may result from partial alteration of primary sulfides (Lorand, 1990) or simply a nugget effect. Note that 30 mg of peridotite with 30 ppm Cu contains only five as much Cu as a 30-µm-large spherical chalcopyrite (~0.5 µg) with 35 wt% Cu. A random inclusion or omission of such a chalcopyrite in a 30-mg-large analytical sample implies thus a difference of ~20% in the measured Cu concentration. In the case of our study, the higher Cu concentrations might also be caused by melt-rock reaction. One example is sample 19-11, which is composed of a spinel harzburgite and a gabbro vein. Although both the vein and its halo (subsample 19-11B) were cut out from the spinel harzburgite (subsample 19-11A), the melt-rock reaction might have reached beyond the halo, for example along smaller apophyses, and enriched the spinel harzburgite in Cu.

The pairs of Cu and S concentrations in the spinel harzburgites scatter around the section of mantle depletion curve limited by 6% and 17% (Fig. 6) representing the minimum and maximum mantle melting degrees at the Kane Megamullion (Dick et al., 2010). The start of this theoretical depletion curve (Fig. 6) is anchored at the primitive mantle values of 30 ppm Cu and 250 ppm S from McDonough and Sun (1995). The S and Cu concentrations in the peridotite residue derived from differing degrees of melting have been calculated by a fractional melting model of Lee et al. (2012), assuming a temperature of 1400 °C, a pressure of 2 GPa, and an oxygen fugacity buffered by quartz-fayalite-magnetite. Note that Cu is incorporated into melt slower than S (Fig. 6). In contrast to S, a portion of Cu inventory is controlled by spinel with a partition coefficient of 0.2 and silicates (i.e., olivine, orthopyroxene, clinopyroxene) with partition coefficients between 0.034 and 0.048 (Lee et al., 2012).

The range of Cu-S compositions observed in the melt-modified mantle could be explained by impregnation of previously depleted harzburgites with Cu-rich sulfides (Fig. 6). The correlation between Cu and S concentrations shows a coefficient of determination ($R^2$) of 0.66 in the group of melt-modified mantle rocks, whereas little correlation is found amongst the spinel harzburgites. All seven melt-modified mantle rocks exhibit high Cu values ranging from 88 to 294 ppm Cu. This is remarkable as in the primitive mantle the Cu concentration is estimated as 30 ± 12 ppm (Sun, 1982). A primitive MORB melt formed from a sulfur-depleted mantle source can contain >150 ppm Cu (Lee et al., 2012). We found 157 ppm Cu (Table 2) and abundant chalcopyrite associated with pyrrhotite and pentlandite (Tables 3, 4, and A.1) in an olivine websterite hosted by harzburgite. Dick et al. (2010) interpreted this olivine websterite to likely represent a frozen melt.

In principle, the enrichment of the chalcophile elements in the crust-mantle transition zone could result from primary magmatic or secondary hydrothermal processes. To distinguish between these processes we use the measured Cu isotopic compositions of analyzed chalcopyrites. The $\delta^{65}$Cu range (-0.04 to +0.29‰; Table 3) we found is entirely within the terrestrial $\delta^{65}$Cu range for igneous rocks (Fig. 12) typically reported as -0.3 to 0.3 ‰ (Larson et al., 2003; Ben Othman et al., 2006; Ikehata and Hirata, 2012; Liu et al., 2015), and exceptionally as -0.6 to 0.4‰ (Zhu et al., 2000). In contrast, the terrestrial $\delta^{65}$Cu range for non-igneous rocks is >9‰ (Larson et al., 2003; Mathur et al., 2010; Mathur and Fantle, 2015). For example, $\delta^{65}$Cu of peridotites metasomatized by LREE-enriched fluids varies from -0.6 to 1.8‰ (Savage et al., 2014; Liu et al., 2015). The $\delta^{65}$Cu signature of seawater ranges from 0.5 to 1.4‰ (Vance et al., 2008). Considering that seawater is an agent during serpentinization, copper sulfides formed of the seawater-derived Cu would have the higher $\delta^{65}$Cu values than the Kane Megamullion chalcopyrites. The $\delta^{65}$Cu signature of Cu-rich minerals in supergene systems overlaps the igneous signature extending to much higher and much lower values (Mathur et al., 2009; 2010; 2012; Mirnejad et al., 2010; Mathur and Fantle, 2015). This is the case for both the enrichment zone ($\delta^{65}$Cu of −6 to +8‰) and the leached zone (-9 to +2‰; Mathur and Fantle, 2015) of supergene systems. The only sulfide type that shows a similar range of $\delta^{65}$Cu to the igneous sulfides is the group of marine sedimentary sulfides (-0.1 to +0.4‰; Maréchal et al., 1999; Rouxel et al., 2004). The relatively narrow $\delta^{65}$Cu range we find is thus likely of magmatic origin (Fig. 12). Although the narrow range itself cannot entirely exclude a fluid-metasomatism or even supergene origin, the probability of those is relatively low. This can be demonstrated using probability density functions of normal distributions anchored on literature data. For example, the probability for one sample showing $\delta^{65}$Cu of -0.1 to 0.3‰ to be of fluid-metasomatism origin (with a mean of 0.15‰ $\delta^{65}$Cu, and an SD of 0.4‰ $\delta^{65}$Cu based on Liu et al. (2015) data for 32 samples) is ~38%, and for a set of four samples only ~2%. The probability for these samples to be of supergene origin is clearly yet lower.

The obtained $\delta^{65}$Cu signatures of -0.04 to 0.29‰ could also result from mixing of two different components. For example, a combination of altered mantle and seawater could produce the reported $\delta^{65}$Cu values, despite neither of these individual reservoirs having a $\delta^{65}$Cu of -0.04 to 0.29‰ (Fig. 12). A mixing scenario is often proposed for bulk rock signatures, which can preserve various processes that all contribute to one bulk signature. However, $\delta^{65}$Cu signatures were measured in cogenetic chalcopyrites. Yielding such a mixed $\delta^{65}$Cu signature in cogenetic chalcopyrites would then require a Cu-rich seawater (the first endmember) to enter a serpentinized mantle elsewhere, dissolve local secondary copper phases (the second endmember), and precipitate the chalcopyrites afterwards during the ascent of seawater to the surface. Such a scenario cannot be completely excluded but it is not supported by the petrographic features of our chalcopyrites that survived as inclusions in silicate phases (Fig. 8a) or in larger sulfide grains (Fig. 8b). The chalcopyrites in the polysulfide grains show exsolution textures with pentlandite and remain in close association with pyrrhotite (Fig. 8b), hence suggesting formation from a sulfide liquid. The wide range of (Ni/(Ni+Fe) we observe in these pentlandites (Section 4.4) is typical for high-temperature sulfides (Kaneda et al., 1986), which further supports their magmatic origin. Similar pyrrhotite-pentlandite-chalcopyrite assemblages that exsolved from a sulfide liquid are found in many magmatic sulfide deposits (Ballhaus and Sylvester, 2000; Mao et al., 2008; Song et al., 2009; Dare et al., 2010; Prendergast, 2012) and are common in the mantle (Kiseeva et al., 2017; Vaughan and Corkhill, 2017). Such magmatic sulfides are also known also from abyssal peridotites (Luguet and Lorand, 1999).

Magmatic pyrrhotite-pentlandite-chalcopyrite assemblages occur not only in the melt-modified mantle but also in the residual mantle. In the residual mantle, however, pentlandite predominates (Garuti et al., 1984), which contrasts with our sulfides dominated by pyrrhotite (Table 4 and Fig. 8b). A MORB-like melt has the potential to yield Fe-rich monosulfides, which then exsolve to polysulfide grains with predominant pyrrhotite. Sulfide globules from MORBs are composed of 44 wt% Fe, 11 wt% Ni, 7 wt% Cu, and 38 wt% S (Francis, 1990). Similar sulfides are ubiquitous in the world's most extensively sampled *in situ* section of the lower oceanic crust at Atlantis Bank as revealed in long ODP Holes 735B (Miller and Cervantes, 2002) and U1473A (Ciazela et al., 2016; Pieterek et al., 2017; Ciazela et al., 2017a). Higher modes of pyrrhotite than pentlandite, and chalcopyrite, have also been found in the melt-modified mantle from ODP Site 1268 (Miller, 2007). Other authors pointed out the close association of pentlandite and chalcopyrite in the melt-modified abyssal peridotites (Luguet et al., 2003; Seyler et al., 2007; Marchesi et al., 2013), which is revealed also in our study (Fig. 8b). Studies of mantle xenoliths indicate that chalcopyrite in the residual sulfides occurs mainly in sulfide rims. In contrast, in the sulfides delivered by percolating melt chalcopyrite may occur in the middle of sulfide grains (Alard et al., 2002; Wang et al., 2009) as is the case for the Kane Megamullion (Fig. 8b). In addition, sulfide melt may occasionally be rich in Cu allowing chalcopyrite to dominate the sulfide grains (Wang et al., 2009; cf. Fig. 8a). The Kane Megamullion magmatic sulfides from the melt-modified mantle are thus likely formed due to melt percolation, and could not be residual as already demonstrated by the enhanced high bulk-rock Cu and S contents of the melt-modified mantle rocks (Fig. 6).

The moderate enrichment of other chalcophile elements in the melt-modified peridotites can also be explained by impregnation with a Cu-rich monosulfide. Chalcopyrite can contain Zn, Se, Cd, Pb, Au, and Ag as trace elements. For example, magmatic chalcopyrites from Sudbury in Canada contain 370-1100 ppm Zn, 3-6 ppm Cd, 30-150 ppm Se, and 2-8 ppm Pb (Dare et al., 2011). The Kane Megamullion chalcopyrites contain up to 1700 ppm Zn and 20 ppm Cd (Section 4.5). Pentlandite and pyrrhotite also contribute to the high budget of some trace elements. Kane Megamullion pentlandites, especially those which occur at the peridotite gabbro-contact (Fig. 9c), are considerably enriched in Co, As, Ge and Te (Fig. 9). Pyrrhotite is usually enriched in Tl and As (Fig. 9a).

### 5.2. Mechanism of melt refertilization

Melt refertilization of the mantle peridotites seems to be a process that occurs over a broad range of pressures and temperatures within the suboceanic and subcontinental mantle. Sulfides are documented in many high pressure (up to 2.5 GPa) mantle xenoliths that experienced melt metasomatism (Lorand et al., 2003; Wang et al., 2009; Michalak and Nowak, 2010; Chen et al., 2014; Bukała et al., 2015). The metasomatic sulfides in xenoliths can be distinguished by their interstitial positions and radiogenic $^{187}Os/^{188}Os$ (Alard et al., 2002; Harvey et al., 2011; 2016). A lower pressure range is recorded in some refertilized orogenic mantle sections (Rehkämper et al., 1999). In addition, melt metasomatism yields sulfides in abyssal peridotites (Rehkämper et al., 1999; Luguet et al., 2003; Alard et al., 2005; Miller, 2007; Seyler et al., 2007). These sulfides are also interstitial, and may show radiogenic $^{187}Os/^{188}Os$ (Harvey et al., 2006; Burton et al., 2012) and potentially radiogenic $^{207}Pb/^{204}Pb$ (Burton et al., 2012).

Considering this broad spectrum of tectonic settings likely encompassing a broad range of pressures and temperatures, neither pressure nor temperature seems to be a key factor responsible for melt refertilization of chalcophile elements in the mantle. Instead, a decreasing Fe content is consistent with lowering the level of sulfur concentration at sulfide saturation (SCSS; Haughton et al., 1974; O'Neill and Mavrogenes, 2002; Tsujimura and Kitakaze, 2005; Ariskin et al., 2013), and could play a major role for sulfide precipitation from percolating melt. Iron loss is likely efficient in narrow melt channels (Ciazela et al., 2017b), where Fe in melt is buffered by the exchange reaction with large amount of olivine and pyroxene on conduit walls (Dick and Natland, 1996). Sulfide crystallization on a scale of the crust-mantle transition zone may though require a more extensive mechanism. Other researchers proposed that the Fe loss results from olivine (Luguet and Lorand, 1999) or spinel (Luguet et al., 2003) crystallization. Melt-rock reaction to form dunite consumes pyroxene, while precipitating olivine, or forms it by incongruent dissolution of orthopyroxene (Kelemen et al., 1995). The most prominent example of such dunite can be found in the Oman ophiolite (Braun and Kelemen, 2002), where dunite constitutes most of the Moho transition zone (MTZ). The MTZ can be several to several hundred meters thick. The thickest MTZ occurs above mantle diapirs (Boudier and Nicolas, 1995). These sections of MTZ are considered to be major collecting zones for mantle melts (Godard et al., 2000). More than 20 sites of ancient Cu excavations have been found at the MTZ of the Oman ophiolite (Begemann et al., 2010). Although Cu has been partially redeposited by secondary processes (Goettler et al., 1976; Begemann et al., 2010), the data from our study and the characteristic distribution of the ancient mining sites imply that the first stage of Cu enrichment may have been magmatic. In the ophiolitic peridotites from the Lanzo massif in Italy, dunitic bands that are a product of melt percolation in the mantle are enriched in Cu (Lorand et al., 1993). Notably, the mean Cu concentration of 14 Kane Megamullion dunites and olivine-rich troctolites formed after dunites (Dick et al., 2010; Sanfilippo et al., 2015) is 118 ± 17 ppm Cu (1 SE). This is four times higher than the average for our spinel harzburgites.

Considering that melt-mantle reaction seems to be most extensive within the crust-mantle transition zones as suggested by the distribution of reactive dunite (Jousselin et al., 1998; Kelemen et al., 2000), we expect a global peak of chalcophile element concentrations at the crust-mantle boundary. However, we suppose that the degree of enrichment in chalcophile elements depends on tectonic setting. The most enhanced chalcophile element concentrations may occur at the crust-mantle boundaries at the sections of slow-spreading oceanic lithosphere with higher thickness and lower temperature. Here, the degree of refertilization reflected in amount of plagioclase peridotites is the highest (Dick, 1989). Furthermore, where the crust-mantle boundary is shallow, conductive cooling brought by hydrothermal circulation accelerates melt solidification upon its reaction with the mantle (Ciazela et al., 2017b). In addition, the Kane Megamullion mantle is heavily serpentinized, and contains up to 15 wt% $H_2O$ (Table 1), which may be partially stored in the serpentinized peridotites already before melt-mantle reaction. A serpentinite-melt reaction is suggested by the high water content of the Kane Megamullion MORBs (Ciazela et al., 2017b) and a distinct zone of contact metamorphism in sample 21-9. Here, approaching the contact with the gabbro, lizardite is replaced by antigorite and then tremolite (Fig. 7 and Section 5.5). The wet gabbro solidus at a pressure of 0.2 GPa is only 840°C (Collins et al., 2016) and ~15 wt% $H_2O$ in the surrounding serpentinites is likely sufficient to saturate even large amount of melts. Water can be released into the melt once antigorite breaks down which occurs at a temperature of ~520 °C at 0.2 GPa (Ulmer and Trommsdorff, 1995). The water lowers the solidus temperature of the melt-mantle reaction allowing an even larger amount of melt to react with the conduit walls, and consequently a yet more efficient Fe loss (Ciazela et al., 2017b). This is probably the reason why the Cu content of the Kane Megamullion refertilized mantle is so elevated (up to 300 ppm) with respect to the refertilized mantle sections reported elsewhere (e.g., 50 ppm Cu reported by Lorand et al. 2013).

### 5.3. Mantle-melt reaction affects the Cu budget in the oceanic crust

The effect of the melt-mantle reaction on the Cu budget of a melt can be considered on a local, regional or global scale. To estimate this effect on a local scale, we compare the Cu concentrations of a single gabbroic vein that reacted with the mantle to the Cu concentrations within an average massive gabbro that underwent no or a limited reaction with the mantle. The 2-cm-wide olivine gabbro vein in sample 21-9 (Fig. 3a) contains 15 ppm Cu. In contrast, the massive olivine gabbro and troctolites from the Kane Megamullion OCC contain on average 82 ppm Cu. A similar average Cu content (74 ppm) is shown by the fresh massive olivine gabbro from the 810-m deep Hole U1473 at the Atlantis Bank OCC (Ciazela et al., 2016; Dick et al., 2016). Assuming the massive gabbro would be free of any melt-mantle interaction, the Cu loss from a vein succumbed to an extensive reaction with the mantle would be thus ~80%.

The effect of melt-mantle reaction on a regional scale can be estimated from the Cu concentrations in MORBs that extensively interacted with the mantle. Ciazela et al. (2017b) showed that MORBs from the Kane Megamullion and a broader area of the entire Kane Fracture Zone between 22 and 25°N along the MAR (Bryan et al., 1981) were subjected to extensive interaction with the mantle. Due to this interaction, the MORBs have left behind ~50% of their initial Cu load during the ascent through the mantle and crust-mantle transition zone (Ciazela et al., 2017b).

The effect of melt-mantle reaction on the global scale may be estimated from the mass balance between primitive MORBs representing the bulk oceanic crust, and their products, that is erupted MORBs representing the upper crust, and gabbro cumulates representing the lower crust. The primitive MORBs probably contain 100-120 ppm Cu (Jenner and O'Neill, 2012; Lee et al., 2012). Erupted MORBs show a global average Cu concentration of 81 ± 25 ppm (White and Klein, 2013). Taking a ratio of 1:2 between basalts and gabbro we could thus expect 125 ± 12 ppm Cu in the gabbro cumulates. This is however not the case as the global average gabbro Cu concentration is 71 ± 19 ppm (Coogan, 2014). This discrepancy implies that 20 to 62% of the Cu load would be precipitated below the crust, for example at the crust-mantle transition or melt-modified mantle rocks below. Although this global estimate is likely lower than the regional estimate of 50% for the Kane Megamullion, it is still considerably high.

### 5.4. Crust-mantle transition zones and related sulfide ore deposits

In addition to the southern Oman ophiolite (Section 5.2), large sulfide deposits are mined in the crust-mantle transition zones of the Outokumpu Ophiolite in Finland, the Troodos Ophiolite in Cyprus, and the Taurids Ophiolite in Turkey. The Outokumpu ore district in Finland is spatially related to dunites and serpentinites of the Outokumpu Ophiolite (Saalmann and Laine, 2014; 2015). The nature of the primary Cu enrichment at the Outokumpu Ophiolite is not entirely clear due to complex on-land processes after the obduction of the ophiolite. The recent petrogenetic models indicate, however, a proto-ore Cu enrichment at the slow-spread mantle-dominated lithosphere (Peltonen et al., 2008) similar to that of the Kane Megamullion. Furthermore, Peltonen et al. (2008) demonstrated that the mantle was extensively metasomatized already before the obduction.

Sulfide enrichment at the crust-mantle boundary of the Troodos ophiolite is easier to interpret as post-obduction processes did not obscure the primary processes to the same extent as at the Outokumpu Ophiolite. The Cu-Ni-Fe-Co sulfide ores from the Limassol Forest Plutonic Complex in Troodos occur within dunites of the local crust-mantle transition zone (Panayiotou, 1978). The sulfide ores are associated with magmatic podiform chromite deposits (Panayiotou, 1978; Panayiotou, 1980), which typically form through peridotite-melt reaction (Arai and Miura, 2015). Similar to the Kane Megamullion, the Limassol Forest primary sulfides are composed of pyrrhotite, troilite, chalcopyrite and pentlandite exsolved together from a sulfide liquid. Although the sulfides occur within the ultramafic rocks, the sulfide Cu/Ni and Pt/Pd are similar to those from magmatic sulfides hosted within gabbroic intrusions (Foose et al., 1985). This further suggests the first step of ore-formation was related to melt-mantle reaction. As is also seen in abyssal peridotites, hydrothermal processes related to serpentinization redistributed primary sulfides and perhaps yielded additional chromites (ferrichromites rims accreted on chromite cores) and sulfides (formation of secondary pentlandite after decomposition of olivine) (Thalhammer et al., 1986).

Sulfide deposits associated with magmatic podiform chromites have also been found at the Ergani mine in the Taurids Ophiolite in Turkey (Bamba, 1976). These deposits have been completely reworked by hydrothermal processes and pyrite currently predominates. However, relictic pyrrhotite-pentlandite-chalcopyrite polysulfides co-existing with the chromites (Akinci, 2009) suggest a magmatic pre-enrichment. In fact, four of five Cu mineralization fields from this region lie at the contact between massive serpentinites and crustal rocks; the fifth one is located only 200 m from such a contact (Akinci, 2009). The high spatial relationship of all the aforementioned sulfide deposits to the crust-mantle transition zones is thus likely caused by melt-mantle reaction.

If penetrated by high-temperature hydrothermal fluids sulfide-rich crust-mantle transition zones might represent source rocks for overlying hydrothermal sulfide deposits on the surface. This seems to be the case for the hydrothermal Aarja sulfide deposits in the northern Oman Ophiolite. Negishi et al. (2013) demonstrated that sulfide-rich dunite from the Moho transition zone is the most likely source of metals and S in the Aarja sulfide deposits. They revealed the same nearly-mantle S isotope signature in both the sulfide groups.

At the Kane Megamullion OCC, several hydrothermal vents have been documented by Tucholke (2013). Their hydrothermal products are highly enriched in all the chalcophile elements (Section 4.3; Table C.1 in Appendix C). A fossil provannid gastropod found in the associated sediments indicates that this hydrothermal venting contained high-temperature fluids in the past (Kaim et al., 2012). The Kane Megamullion crust-mantle transition zone might be the source rock for these hydrothermal products as it is easy for the hydrothermal fluids to access the crust-mantle transition zone. These zones of magmatic enrichment related to melt refertilization might be one of the reasons why large massive sulfide deposits form mostly at the slow spreading ridges and not at the fast spreading ridges (Hannington et al., 2011). Many seafloor massive sulfides in the recent oceans, including the largest and those with the highest Cu grade (Petersen and Hein, 2013; Hein et al., 2013), are hosted in the peridotite-dominated lithosphere with a thin and heterogeneous crust (Gràcia et al., 2000; Kelley et al., 2001; Petersen et al., 2009; Pertsev et al., 2012; Kostitsyn et al., 2013; Tucholke et al., 2013; Andreani et al., 2014; Ciazela et al., 2015), where melt-mantle reaction is likely more enhanced (Ciazela et al., 2017b). In on-land prospecting, the search for chalcophile deposits seeks regions with both an appropriately enriched source rock, and a mechanism for concentrating those elements in a deposit. Until now explanations for the massive sulfide deposits at slow-spreading ridges have emphasized the hydrothermal systems associated with long-lived faults needed to build large deposits, but having the appropriate source rocks is demonstrably as important. Our work shows that the latter exists in the crust-mantle transition zones at slow spreading ridges where it is brought to shallow levels by detachment faulting.

### 5.5. Effect of low-temperature alteration.

The melt-modified peridotite Cu/S are too high to be reproduced by simple sulfide impregnation even if the sulfides are Cu-rich (Fig. 6). Such high Cu/S imply that sulfur was partially lost from the melt-modified mantle rocks due to later low-temperature processes. Desulfurization commonly occurs during mantle serpentinization (Delacour et al., 2008a; Wittke et al., 2016). Specifically, higher mobilization of sulfur than chalcophile elements during serpentinization has been documented in the Cemetery Ridge peridotites, Arizona, USA (Wittke et al., 2016). Here, sulfur declines by a factor of 5 to 10 between the most fresh and the most serpentinized harzburgites, whereas the concentrations of chalcophile elements remain at the same level (Wittke et al., 2016). An additional loss of sulfur seems to be caused by subsequent talc alteration of serpentinized peridotites (Section 4.3; cf. Paulick et al., 2006; Harvey et al., 2014).

Serpentinization leads to alteration of primary sulfide minerals. For example, pentlandite is commonly altered to heazlewoodite and magnetite, and potentially godlevskite and awaruite (Klein and Bach, 2009). Serpentinization seems to cause faster dissolution of chalcopyrite, which is never retained in the presence of heazlewoodite in our samples (Table 4). In contrast, chalcopyrite is often retained when pentlandite is altered to violarite (Table 4). This may be related to weathering-related aerated oxidizing conditions, in which violarite is typically formed (Watmuff, 1974).

Due to ubiquitous serpentinization the elevated concentrations of chalcophile elements (Table 2) do not match with the low chalcopyrite modes in the melt-modified peridotites (Table 4). Copper and chalcophile elements have been incorporated into other minerals. Some Cu is retained in Fe-Cu hydroxides formed after chalcopyrites. One of them documented in the 21-7 peridotite-gabbro contact (Fig. 8b) contains 13 wt% Cu and only 0.3 wt% S. Similar hydroxides but with lower Cu and higher S contents were found in altered mantle xenoliths by Lorand (1990).

The Fe-Cu hydroxides are, however, too scarce to account for the entire high Cu budget of the melt-modified mantle zone in the Kane Megamullion. Searching for alternatives we investigated matrix minerals of peridotite-gabbro contacts and some plagioclase peridotites that are enriched in $Al_2O_3$, CaO and $P_2O_5$ (Section 4.6; Table B.1 in Appendix B). This enrichment is likely owed to melt-mantle reaction. Using X-ray mapping (Fig. 3b-c) we detected a dense front of S-rich phases along peridotite-gabbro contacts in samples 21-9 (Fig. 3b) and 19-11. Although the trace element composition of only a few of the largest secondary grains could be determined (Co and Cu-rich pentlandites; Fig. 7), the laser ablation profile of the matrix minerals show that most chalcophile elements are enriched at this zone (Fig. 10). The same is true for the matrix measurements of plagioclase peridotites (Fig. 11; Table B.1 in Appendix B). Using the ore microscope and electron microprobe we investigated the area abutting the lines of the laser profile with the highest chalcophile element concentrations. We found abundant submicron-to-5-µm diameter pentlandites that likely cause the high chalcophile element LA-ICPMS signal detected in this area (Fig. 10). The high signal results from two factors. Firstly, pentlandites occur more densely here. Secondly, all chalcophile element concentrations are enhanced in these pentlandites (Table A.1 in Appendix A), and their Pb, Bi, Cu, As and Te contents (Fig. 9c) are up to one order of magnitude higher than in pentlandites elsewhere.

Secondary sulfides and post-sulfide phases are known from other serpentinized peridotites. In abyssal peridotites from ODP Hole 1274A near to the 15°20’ Fracture Zone along the MAR, Marchesi et al. (2013) found heazlewoodite, jaipurite (CoS), awaruite ($Ni_3Fe$), wairauite (CoFe), and native copper that replaced magmatic pentlandite and chalcopyrite. At the Kane Megamullion, not only secondary pentlandites (Fig. 9c) but also heazlewoodite, millerite and godlevskite (Fig. 9b) seem to follow the trace element pattern of primary pentlandites. In addition, the secondary Ni sulfides contain considerable amount of Bi and Cu (Fig. 9), which have probably been inherited from former chalcopyrites dissolved during serpentinization.

Chalcophile metals seem thus to be retained in submicron phases, including secondary sulfides, metal hydroxides, and potentially native metals or alloys, embedded in the matrix of low-temperature silicate minerals. Tiny sulfides (Alt and Shanks, 2003; Delacour, 2008b; Marchesi et al., 2013), alloys (Lorand et al., 2010; Marchesi et al., 2013), and native Cu grains (Luguet et al., 2003; Seyler et al., 2007; Marchesi et al., 2013) embedded in serpentine matrices are commonly reported in abyssal serpentinized peridotites.

The entrapment of chalcophile elements in secondary phases *in situ* is likely caused by the fact that fluids <350 °C are unable to maintain significant concentrations of metals, including Zn and Cu (Seewald and Seyfried, 1990). The only high temperature alteration we found is the narrow zone of contact metamorphism between the mafic vein and the peridotite in sample 21-9. Here, tremolite (Fig. 10) is proximal to the vein and is followed by the symplectite of Al and Fe-rich antigorite and chrysotile identified by X-ray Diffraction (XRD) (Figs. 4 and 7 and Fig E.1 in Appendix E). Otherwise, the most common alteration phases are prehnite in gabbro and lizardite in peridotite identified by XRD (Fig. E.2 in Appendix E), which are both low-temperature silicates. Lizardite in <0.8 GPa is typically stable at <280 °C (O'Hanley and Wicks, 1995; Evans, 2004; Schwartz et al., 2013) and prehnite is stable between 150 and 300 °C (Bucher and Grapes, 2011). Therefore, most of the chalcophile metals have not been transported away neither from the peridotite nor from the peridotite-gabbro contacts. Similarly, MORBs altered to low-temperature facies retain primary contents of all chalcophile elements (Bach et al., 2003; Alt et al., 2010).

## 6. CONCLUSIONS

1. The crust-mantle transition zone exposed in the Kane ocean core complex is highly enriched in chalcophile metals. This enrichment is most pronounced along centimeter-scale peridotite-gabbro contacts but is spread throughout the entire zone as documented in the plagioclase harzburgites and dunites. Copper, As, Zn, Sb, and Tl are typically enriched by one order of magnitude, whereas the enrichment of Ga, Pb, and Se is modest. Nickel, which is largely controlled by olivine, and Bi are the only two chalcophile elements that show no sign of enrichment at the crust-mantle boundary.
2. The enrichment in chalcophile metals is related to the crystallization of sulfides during extensive melt-mantle reaction throughout the transition zone. Importantly, partial dissolution of sulfides during serpentinization does not mobilize the metals from the rocks. The portion of chalcophile elements that was released from primary sulfides has been trapped in submicron secondary sulfides, hydroxides and perhaps native metals embedded in the silicate matrix.

3. Our results combined with Cu deposits documented in the crust-mantle transition zones of various ophiolites may indicate that the enrichment of chalcophile elements could be expected globally along the oceanic crust-mantle boundary.
4. The crystallization of sulfides from melt interacting with peridotite can influence melt evolution. The precipitation of sulfides is caused by lowering sulfur concentration at sulfide saturation upon FeO loss during melt-mantle reaction, which could not be achieved by fractional crystallization processes alone. We estimate that 20% to 80% of the chalcophile metal inventory in a melt can be lost from the melt during reaction with mantle peridotite. This is a significant loss determining further melt evolution and should be considered in melt modelling.

## ACKNOWLEDGEMENTS

We thank an anonymous reviewer, A. Sanfilippo, and editor W. Bach for their thorough and insightful comments. In addition, we would like to acknowledge D. Jousselin from Université de Lorraine, F. Boudier from Université de Montpellier, F. Ridolfi, J. Feige, F. Holtz, M. Albrecht, F. Tramm, E. Wolff, C. Zhang and T. Gärtner from the Leibniz Universität Hannover, A. Bruns and F. Korte from the Federal Institute for Geosciences and Natural Resources in Hannover, S. Humphris, B. Tucholke and F. Ji from the Woods Hole Oceanographic Institution, and M. Ciążela, J. Nowak and A. Żelaźniewicz from the Institute of Geological Sciences of the Polish Academy of Sciences in Wroclaw. This research was funded by a *Diamond Grant* of the Polish Ministry of Science and Higher Education (DI2012 2057 42 to J. Ciazela), and partly supported by grants of the U.S. National Science Foundation (OCE1434452 and OCE 1637130 to H.J.B. Dick), and the German Science Foundation (Bo2941/4-1 to R. Botcharnikov).

## REFERENCES

Akinci Ö. T. (2009) Ophiolite-hosted copper and gold deposits of southeastern Turkey: Formation and relationship with seafloor hydrothermal processes. *Turkish J. Earth Sci.* **18**, 475–509.

Alard O., Griffin W. L., Pearson N. J., Lorand J. P. and O'Reilly S. Y. (2002) New insights into the Re-Os systematics of sub-continental lithospheric mantle from in situ analysis of sulphides. *Earth Planet. Sci. Lett.* **203**, 651–663.

Alard O., Luguet A., Pearson N. J., Griffin W. L., Lorand J.-P., Gannoun A., Burton K. W. and O'Reilly S. Y. (2005) In situ Os isotopes in abyssal peridotites bridge the isotopic gap between MORBs and their source mantle. *Nature* **436**, 1005–1008.

Albrecht M., Derrey I. T., Horn I., Schuth S. and Weyer S. (2014) Quantification of trace element contents in frozen fluid inclusions by UV-fs-LA-ICP-MS analysis. *J. Anal. At. Spectrom.* **29**, 1034.

Alt J. C. and Shanks W. C. (2003) Serpentinization of abyssal peridotites from the MARK area, Mid-Atlantic Ridge: Sulfur geochemistry and reaction modeling. *Geochim. Cosmochim. Acta* **67**, 641–653.

Alt J. C., Laverne C., Coggon R. M., Teagle D. A. H., Banerjee N. R. and Morgan S. (2010) Subsurface structure of a submarine hydrothermal system in ocean crust formed at the East Pacific Rise, ODP/IODP Site 1256. *Geochemistry, Geophys. Geosystems* **11**, Q10010.

Andreani M., Mével C., Boullier M. and Escartín J. (2007) Dynamic control on serpentine crystallization in veins: Constraints on hydration processes in oceanic peridotites. *Geochemistry, Geophys. Geosystems* **8**, 1–57.

Andreani M., Escartin J., Delacour A., Ildefonse B., Godard M., Dyment J., Fallick A. E. and Fouquet Y. (2014) Tectonic structure, lithology, and hydrothermal signature of the Rainbow massif (Mid-Atlantic Ridge 36°14’N). *Geochemistry, Geophys. Geosystems* **15**, 3543–3571.

Arai S. and Miura M. (2015) Podiform chromitites do form beneath mid-ocean ridges. *Lithos* **232**, 143–149.

Ariskin A. A., Danyushevsky L. V., Bychkov K. A., McNeill A. W., Barmina G. S. and Nikolaev G. S. (2013) Modeling solubility of Fe-Ni sulfides in basaltic magmas: The effect of nickel. *Econ. Geol.* **108**, 1983–2003.

Bach W., Bernhard P. E., Hart S. R. and Blusztajn J. S. (2003) Geochemistry of hydrothermally altered oceanic crust: DSDP/ODP Hole 504B - Implications for seawater-crust exchange budgets and Sr- and Pb-isotopic evolution of the mantle. *Geochemistry, Geophys. Geosystems* **4**, 40–55.

Ballhaus C. and Sylvester P. (2000) Noble Metal Enrichment Processes in the Merensky Reef, Bushveld Complex. *J. Petrol.* **41**, 545–561.

Bamba T. (1976) Ophiolite and related copper deposits of the Ergani mining district, southeastern Turkey. *Bull Min. Res Explor Inst Turk* **86**, 36–50.

Barber C. (1974) Major and trace element associations in limestones and dolomites. Chem. Geol. 14, 273–280.

Begemann F., Hauptmann A., Schmitt-Strecker S. and Weisgerber G. (2010) Lead isotope and chemical signature of copper from Oman and its occurrence in Mesopotamia and sites on the Arabian Gulf coast. *Arab. Archaeol. Epigr.* **21**, 135–169.

Ben Othman D., Luck J. M., Bodinier J. L., Arndt N. T. and Albarede F. (2006) Cu–Zn isotopic variations in the Earth's mantle. *Geochim. Cosmochim. Acta* **70**, A46.

Benn K., Nicolas A. and Reuber I. (1988) Mantle-crust transition zone and origin of wehrlitic magmas: Evidence from the Oman ophiolite. *Tectonophysics* **151**, 75–85.

Bonatti E., Emiliani C., Ferrara G., Honnorez J. and Rydell H. (1974) Ultramafic-carbonate breccias from the equatorial Mid Atlantic Ridge. *Mar. Geol.* **16**, 83–102.

Bosch D., Jamais M., Boudier F., Nicolas A., Dautria J. M. and Agrinier P. (2004) Deep and high-temperature hydrothermal circulation in the Oman ophiolite - Petrological and isotopic evidence. *J. Petrol.* **45**, 1181–1208.

Boschi C., Früh-Green G. L., Delacour A., Karson J. and Kelley D. S. (2006) Mass transfer and fluid flow during detachment faulting and development of an oceanic core complex, Atlantis Massif (MAR 30°N). *Geochemistry, Geophys. Geosystems* **7**, Q01004.

Boudier F. and Nicolas A. (1995) Nature of the Moho Transition Zone in the Oman Ophiolite. *J. Petrol.* **36**, 777–796.

Braun M. G. and Kelemen P. B. (2002) Dunite distribution in the Oman Ophiolite: Implications for melt flux through porous dunite conduits. *Geochemistry Geophys. Geosystems* **3**, 1–21.

Bryan W. B., Thompson G. and Ludden J. N. (1981) Compositional variation in normal MORB from 22°–25°N: Mid-Atlantic Ridge and Kane Fracture Zone. *J. Geophys. Res.* **86**, 11815.

Bucher K. and Grapes R. (2011) *Petrogenesis of Metamorphic Rocks*., Springer Science & Business Media.

Bukała M., Puziewicz J., Ntaflos T. and Wojtulek P. (2015) Preliminary data on sulfides from mantle xenoliths from Wilcza Góra and Krzeniów basanites (SW Poland). *Geophys. Res. Abstr.* **17**, EGU2015–4339.

Burton K. W., Cenki-Tok B., Mokadem F., Harvey J., Gannoun A., Alard O. and Parkinson I. J. (2012) Unradiogenic lead in Earth's upper mantle. *Nat. Geosci.* **5**, 570–573.

Canales J. P., Detrick R. S., Lin J., Collins J. A. and Toomey D. R. (2000) Crustal and upper mantle seismic structure beneath the rift mountains and across a nontransform offset at the Mid-Atlantic Ridge (35°N). *J. Geophys. Res.* **105**, 2699–2719.

Canales J. P., Tucholke B. E., Xu M., Collins J. A. and DuBois D. L. (2008) Seismic evidence for large-scale compositional heterogeneity of oceanic core complexes. *Geochemistry, Geophys. Geosystems* **9**, Q08002.

Cann J. R., Blackmann D. K., Smith D. K., McAllister E., Janssen B., Mello S., Avgerinos E., Pascoe A. R. and Escartin J. (1997) Corrugated slip surfaces formed at ridge-transform intersections on the Mid-Atlantic Ridge. *Nature* **385**, 329–332.

Cann J. R., Smith D. K., Escartin J. and Schouten H. (2015) Tectonic evolution of 200 km of Mid-Atlantic Ridge over 10 million years: Interplay of volcanism and faulting. *Geochemistry, Geophys. Geosystems* **16**, 2303–2321.

Cannat M. (1996) How thick is the magmatic crust at slow spreading oceanic ridges? *J. Geophys. Res.* **101**, 2847–2857.

Cannat M., Karson J., Miller D. J. and Shipboard Scientific Party (1995) ODP Leg 153 MARK Initial Report. *Proc. ODP Initial Reports* **153**.

Chen M.-M., Tian W., Suzuki K., Tejada M.-L.-G., Liu F.-L., Senda R., Wei C.-J., Chen B. and Chu Z.-Y. (2014) Peridotite and pyroxenite xenoliths from Tarim, NW China: Evidences for melt depletion and mantle refertilization in the mantle source region of the Tarim flood basalt. *Lithos* **204**, 97–111.

Ciazela J., Koepke J., Dick H. J. B. and Muszynski A. (2015) Mantle rock exposures at oceanic core complexes along mid-ocean ridges. *Geologos* **4**, 207–231.

Ciazela J., Dick H. J. B., MacLeod C. J., Blum P. and the Expedition 360 Scientists (2016) IODP Expedition 360: first stage of drilling into Earth's Mantle. *Przegląd Geol.* **64**, 889–895.

Ciazela J., Koepke J., Strauss H., Pieterek B., Dick H. J. B., Muszynski A., Kuhn T. and Bender M. (2017a) Sulfur isotopes record chalcophile metal transport through the lower oceanic crust : IODP Hole U1473A, Atlantis Bank, Southwest Indian. *Mineral. - Spec. Pap.* **47**, 27.

Ciazela J., Dick H. J. B., Koepke J., Pieterek B., Muszynski A., Botcharnikov R. and Kuhn T. (2017b) Thin crust and exposed mantle control sulfide differentiation in slow-spreading ridge magmas. *Geology* **45**, 935–938.

Collins W. J., Huang H. Q. and Jiang X. (2016) Water-fluxed crustal melting produces Cordilleran batholiths. *Geology* **44**, 143–146.

Coogan L. A. (2014) The Lower Oceanic Crust. In *Treatise on Geochemistry: Second Edition* Elsevier Ltd. pp. 497–541.

Dare S. A. S., Barnes S. J. and Prichard H. M. (2010) The distribution of platinum group elements (PGE) and other chalcophile elements among sulfides from the Creighton Ni-Cu-PGE sulfide deposit, Sudbury, Canada, and the origin of palladium in pentlandite. *Miner. Depos.* **45**, 765–793.

Dare S. A., Barnes S. J., Prichard H. M. and Fisher P. C. (2011) Chalcophile and platinum-group element (PGE) concentrations in the sulfide minerals from the McCreedy East deposit, Sudbury, Canada, and the origin of PGE in pyrite. *Miner. Depos.* **46**, 381–407.

Delacour A., Früh-Green G. L., Bernasconi S. M. and Kelley D. S. (2008a) Sulfur in peridotites and gabbros at Lost City (30°N, MAR): Implications for hydrothermal alteration and microbial activity during serpentinization. *Geochim. Cosmochim. Acta* **72**, 5090–5110.

Delacour A., Früh-Green G. L. and Bernasconi S. M. (2008b) Sulfur mineralogy and geochemistry of serpentinites and gabbros of the Atlantis Massif (IODP Site U1309). *Geochim. Cosmochim. Acta* **72**, 5111–5127.

Detrick R. S., Honnorez J., Bryan W. B., Juteau T. and Expedition 106/109 Scientists (1988) *Proc. ODP, Init. Repts., 106/109.*, Ocean Drilling Program, College Station, TX. doi:10.2973/odp.proc.ir.106109.1988.

Dick H. J. B. (1977a) Evidence of partial melting in the Josephine Peridotite. In *Magma genesis. Proceedings of the American Geophysical Union. Chapman Conference on partial melting in the Earth's Upper Mantle* pp. 59–62.

Dick H. J. B. (1977b) Partial melting in the Josephine peridotite I, the effect on mineral composition and its consequence for geobarometry and geothermometry. *Am. J. Sci.* **277**, 801–832.

Dick H. J. B. (1981) Low-angle faulting and steady-state emplacement of plutonic rocks at ridge-transform intersections. In *EOS Transactions, American Geophysical Union 62* (ed. A. R. Ritsema). p. 406.

Dick H. J. B. (1989) Abyssal peridotites, very slow spreading ridges and ocean ridge magmatism. *Geol. Soc. London, Spec. Publ.* **42**, 71–105.

Dick H. J. B. and Natland J. H. (1996) Late-stage melt evolution and transport in the shallow mantle beneath the East Pacific Rise. *Proc. ODP Sci. Res.* **147**, 103–134.

Dick H. J. B., Tivey M. and Tucholke B. E. (2008) Plutonic foundation of a slow-spreading ridge segment: Oceanic core complex at Kane Megamullion, 23°30′N, 45°20′W. *Geochemistry Geophys. Geosystems* **9**, Q05014.

Dick H. J. B., Lissenberg C. J. and Warren J. M. (2010) Mantle Melting, Melt Transport, and Delivery Beneath a Slow-Spreading Ridge: The Paleo-MAR from 23 15'N to 23 45'N. *J. Petrol.* **51**, 425–467.

Dick H. J. B., Macleod C. J. and Blum P. (2015) Southwest Indian Ridge Lower Crust and Moho: the nature of the lower crust and Moho at slower spreading ridges (SloMo-Leg 1). *Int. Ocean Discov. Progr. Sci. Prospect.* **360**. Available at: http://dx.doi.org/10.14379/iodp.sp.360.2015.

Dick H. J. B., Macleod C. J., Blum P. and the Expedition 360 Scientists (2016) *Expedition 360 Preliminary report: Southwest Indian Ridge lower crust and Moho.*, International Ocean Discovery Program. http://dx.doi.org/?10.14379/?iodp.pr.360.2016.

Dilek Y. and Furnes H. (2014) Ophiolites and their origins. *Elements* **10**, 93–100.

Drouin M., Godard M., Ildefonse B., Bruguier O. and Garrido C. J. (2009) Geochemical and petrographic evidence for magmatic impregnation in the oceanic lithosphere at Atlantis Massif, Mid-Atlantic Ridge (IODP Hole U1309D, 30°N). *Chem. Geol.* **264**, 71–88.

Drouin M., Ildefonse B. and Godard M. (2010) A microstructural imprint of melt impregnation in slow spreading lithosphere: Olivine-rich troctolites from the Atlantis Massif, Mid-Atlantic Ridge, 30°N, IODP Hole U1309D. *Geochemistry, Geophys. Geosystems* **11**, Q06003.

Evans B. W. (2004) The Serpentinite Multisystem Revisited: Chrysotile Is Metastable. *Int. Geol. Rev.* **46**, 479–506.

Fellows S. A. and Canil D. (2012) Experimental study of the partitioning of Cu during partial melting of Earth's mantle. *Earth Planet. Sci. Lett.* **337-338**, 133–143.

Foose M. P., Economou M. and Panayiotou A. (1985) Compositional and mineralogic constrains on the genesis of ophiolite hosted nickel mineralization in the Pevkos Area, Limassol Forest, Cyprus. *Miner. Depos.* **20**, 234–240.

Francis R. D. (1990) Sulfide globules in mid-ocean ridge basalts (MORB), and the effect of oxygen abundance in FeSO liquids on the ability of those liquids to partition metals from MORB and komatiite magmas. *Chem. Geol.* **85**, 199–213.

Garuti G., Gorgoni C. and Sighinolfi G. P. (1984) Sulfide mineralogy and chalcophile and siderophile element abundances in the Ivrea-Verbano mantle peridotites ( Western Italian Alps ). *Earth Planet. Sci. Lett.* **70**, 69–87.

Godard M., Jousselin D. and Bodinier J. L. (2000) Relationships between geochemistry and structure beneath a palaeo-spreading centre: A study of the mantle section in the Oman ophiolite. *Earth Planet. Sci. Lett.* **180**, 133–148.

Goettler, G. W., Firith, N., and Huston, C. E. (1976) A preliminary discussion of ancient mining in the Sultanate of Oman. *J. Oman Studies* **2**, 43-56.

Gràcia E., Charlou J. L., Radford-Knoery J. and Parson L. M. (2000) Non-transform offsets along the Mid-Atlantic Ridge south of the Azores (38°N-34°N): Ultramafic exposures and hosting of hydrothermal vents. *Earth Planet. Sci. Lett.* **177**, 89–103.

Guillong M., Meier D. L., Allan M. M., Heinrich C. A. and Yardley B. W. D. (2008) SILLS: A Matlab-Based Program for the Reduction of Laser Ablation ICP–MS Data of Homogeneous Materials and Inclusions. *Mineral. Assoc. Canada Short Course* **40**, 328–333.

Hannington M., Jamieson J., Monecke T., Petersen S. and Beaulieu S. (2011) The abundance of seafloor massive sulfide deposits. *Geology* **39**, 1155–1158.

Hansen L. N., Cheadle M. J., John B. E., Swapp S. M., Dick H. J. B., Tucholke B. E. and Tivey M. (2013) Mylonitic deformation at the Kane oceanic core complex: Implications for the rheological behavior of oceanic detachment faults. *Geochemistry, Geophys. Geosystems* **14**, 3085–3108.

Hart S. R. and Gaetani G. A. (2006) Mantle Pb paradoxes: The sulfide solution. *Contrib. to Mineral. Petrol.* **152**, 295–308.

Harvey J., Gannoun A., Burton K. W., Rogers N. W., Alard O. and Parkinson I. J. (2006) Ancient melt extraction from the oceanic upper mantle revealed by Re-Os isotopes in abyssal peridotites from the Mid-Atlantic ridge. *Earth Planet. Sci. Lett.* **244**, 606–621.

Harvey J., Dale C. W., Gannoun A. and Burton K. W. (2011) Osmium mass balance in peridotite and the effects of mantle-derived sulphides on basalt petrogenesis. *Geochim. Cosmochim. Acta* **75**, 5574–5596.

Harvey J., Savov I. P., Agostini S., Cliff R. A. and Walshaw R. (2014) Si-metasomatism in serpentinized peridotite: The effects of talc-alteration on strontium and boron isotopes in abyssal serpentinites from Hole 1268a, ODP Leg 209. *Geochim. Cosmochim. Acta* **126**, 30–48.

Harvey J., Warren J. M. and Shirey S. B. (2016) Mantle Sulfides and their Role in Re–Os and Pb Isotope Geochronology. *Rev. Mineral. Geochemistry* **81**, 579–649.

Haughton D. R., Roeder P. L. and Skinner B. J. (1974) Solubility of sulfur in mafic magmas. *Econ. Geol.* **69**, 451–467.

Hein J. R., Mizell K., Koschinsky A. and Conrad T. (2013) Deep-ocean mineral deposits as a source of critical metals for high- and green-technology applications: Comparison with land-based resources. *Ore Geol. Rev.* **51**, 1–14.

Horn I. (2008) Comparison of femtosecond and nanosecond interactions with geologic matrices and their influence on accuracy and precision of LA-ICP-MS data. *Mineral. Assoc. Canada Short Course* **40**, 53–65.

Horn I. and Von Blanckenburg F. (2007) Investigation on elemental and isotopic fractionation during 196 nm femtosecond laser ablation multiple collector inductively coupled plasma mass spectrometry. *Spectrochim. Acta Part B* **62**, 410–422.

Horn I., Von Blanckenburg F., Schoenberg R., Steinhoefel G. and Markl G. (2006) In situ iron isotope ratio determination using UV-femtosecond laser ablation with application to hydrothermal ore formation processes. *Geochim. Cosmochim. Acta* **70**, 3677–3688.

Ikehata K. and Hirata T. (2012) Copper isotope characteristics of copper-rich minerals from the horoman peridotite complex, Hokkaido, Northern Japan. *Econ. Geol.* **107**, 1489–1497.

Jagoutz E., Palme H., Baddenhausen H., Blum K., Cendales M., Dreibus G., Spettel B., Lorenz V. and Wänke H. (1979) The abundances of major, minor and trace elements in the earth's mantle as derived from primitive ultramafic nodules. *Proc. Lunar Planet. Sci. Conf.* **10**, 2031–2050.

Jenner F. E. and O'Neill H. S. C. (2012) Analysis of 60 elements in 616 ocean floor basaltic glasses. *Geochemistry, Geophys. Geosystems* **13**, Q02005.

Jousselin D., Nicolas A. and Boudier F. (1998) Detailed mapping of a mantle diapir below a paleo-spreading center in the Oman ophiolite. *J. Geophys. Res. Earth* **103**, 18153–18170.

Kaim A., Tucholke B. E. and Warén A. (2012) A new Late Pliocene large provannid gastropod associated with hydrothermal venting at Kane Megamullion, Mid-Atlantic Ridge. *J. Syst. Palaeontol.* **10**, 423–433.

Kaneda H., Takenouchi S. and Shoji T. (1986) Stability of pentlandite in the Fe-Ni-Co-S system. *Miner. Depos.* **21**, 169–180.

Karson J. A., Collins J. A. and Casey J. F. (1984) Geologic and seismic velocity structure of the crust/mantle boundary in the Bay of Islands ophiolite complex. *J. Geophys. Res.* **89**, 6126–6138.

Kelemen P. B. (1990) Reaction between ultramafic rock and fractionating basaltic magma I. Phase relations, the origin of calc-alkaline magma series, and the formation of discordant dunite. *J. Petrol.* **31**, 51–98.

Kelemen P. B., Shimizu N. and Salters V. J. M. (1995) Extraction of MORB from the mantle by focussed flow of melt in dunite channels. *Nature* **375**, 747–753.

Kelemen P. B., Braun M. and Hirth G. (2000) Spatial distribution of melt conduits in the mantle beneath oceanic spreading ridges: Observations from the Ingalls and Oman ophiolites. *Geochemistry, Geophys. Geosystems* **1**, 1005.

Kelley D. S., Karson J., Blackman D. K., Früh-Green G. L., Butterfield D., Lilley M. D., Olson E. J., Schrenk M. O., Roe K. K., Lebon G. T. and Rivizzigno P. (2001) An off-axis hydrothermal vent field near the Mid-Atlantic Ridge at 30° N. *Nature* **412**, 145–149.

Kiseeva E. S., Fonseca R. O. C. and Smythe D. J. (2017) Chalcophile elements and sulfides in the upper mantle. *Elements* **13**, 111–116.

Klein E. M. (2003) Geochemistry of the igneous ocean crust. In *Treatise on Geochemistry, vol. 3 The Crust* (ed. R. L. Rudnick). Elsevier, Amsterdam. pp. 433–463.

Klein F. and Bach W. (2009) Fe-Ni-Co-O-S Phase Relations in Peridotite-Seawater Interactions. *J. Petrol.* **50**, 37–59.

Kodolányi J. and Pettke T. (2011) Loss of trace elements from serpentinites during fluid-assisted transformation of chrysotile to antigorite — An example from Guatemala. *Chem. Geol.* **284**, 351–362.

Kostitsyn Y., Silant'ev S., Belousova E., Bortnikov N. S., Krasnova E. and Kannat M. (2013) Time of the formation of the oceanic core complex of the Ashadze hydrothermal field in the Mid-Atlantic Ridge (12°58′ N): Evidence from zircon study. *Dokl. Earth Sci.* **447**, 1301–1305.

Larson P. B., Maher K., Ramos F. C., Chang Z., Gaspar M. and Meinert L. D. (2003) Copper isotope ratios in magmatic and hydrothermal ore-forming environments. *Chem. Geol.* **201**, 337–350.

Lazarov M. and Horn I. (2015) Matrix and energy effects during in-situ determination of Cu isotope ratios by ultraviolet-femtosecond laser ablation multicollector inductively coupled plasma mass spectrometry. *Spectrochim. Acta Part B At. Spectrosc.* **111**, 64–73.

Lee C.-T., Luffi P., Chin E. J., Bouchet R., Dasgupta R., Morton D. M., Le Roux V., Yin Q. and Jin D. (2012) Copper systematics in arc magmas and implications for crust-mantle differentiation. *Science* **336**, 64–8.

Lissner M., König S., Luguet A., le Roux P. J., Schuth S., Heuser A. and le Roex A. P. (2014) Selenium and tellurium systematics in MORBs from the southern Mid-Atlantic Ridge (47–50°S). *Geochim. Cosmochim. Acta* **144**, 379–402.

Liu S. A., Huang J., Liu J., Wörner G., Yang W., Tang Y. J., Chen Y., Tang L., Zheng J. and Li S. (2015) Copper isotopic composition of the silicate Earth. *Earth Planet. Sci. Lett.* **427**, 95–103.

Lorand J. P. (1989a) Abundance and distribution of Cu-Fe-Ni sulfides, sulfur, copper and platinum-group elements in orogenic-type spinel lherzolite massifs of Ariege (northeastern Pyrenees, France). *Earth Planet. Sci. Lett.* **93**, 50–64.

Lorand J. P. (1989b) Mineralogy and chemistry of Cu-Fe-Ni sulfides in orogenic-type spinel peridotite bodies from Ariege (Northeastern Pyrenees, France). *Contrib. to Mineral. Petrol.* **103**, 335–345.

Lorand J. P. (1990) Are spinel Iherzolite xenoliths representative of the abundance of sulfur in the upper mantle? *Geochim. Cosmochim. Acta* **54**, 1487–1492.

Lorand J. P. (1991) Sulphide petrology and sulphur geochemistry of orogenic lherzolites: A comparative study of the Pyrenean bodies (France) and the Lanzo massif (Italy). *J. Petrol.* **Special Lh**, 77–95.

Lorand J. P. and Luguet A. (2016) Chalcophile and Siderophile Elements in Mantle Rocks: Trace Elements Controlled By Trace Minerals. *Rev. Mineral. Geochemistry* **81**, 441–488.

Lorand J. P., Keays R. R. and Bodinier J. L. (1993) Copper and noble metal enrichments across the lithosphere-asthenosphere boundary of mantle diapirs: Evidence from the lanzo lherzolite massif. *J.*

*Petrol.* **34**, 1111–1140.

Lorand J. P., Reisberg L. and Bedini R. M. (2003) Platinum-group elements and melt percolation processes in Sidamo spinel peridotite xenoliths, Ethiopia, East African Rift. *Chem. Geol.* **196**, 57–75.

Lorand J. P., Alard O. and Luguet A. (2010) Platinum-group element micronuggets and refertilization process in Lherz orogenic peridotite (northeastern Pyrenees, France). *Earth Planet. Sci. Lett.* **289**, 298–310.

Lorand J. P., Luguet A. and Alard O. (2013) Platinum-group element systematics and petrogenetic processing of the continental upper mantle: A review. *Lithos* **164-167**, 2–21.

Luguet A. and Lorand J. (1999) Fe-Ni-Cu sulphides of abyssal peridotites from the MARK area (Mid-Atlantic ridge, 20-24°N). *Comptes Rendus de l'Académie des Sciences - Series IIA - Earth and Planetary Science* **329**, 637–644.

Luguet A., Lorand J. P. and Seyler M. (2003) Sulfide petrology and highly siderophile element geochemistry of abyssal peridotites: a coupled study of samples from the Kane Fracture Zone (45°W 23°20N, MARK area, Atlantic Ocean). *Geochim. Cosmochim. Acta* **67**, 1553–1570.

Mao J. W., Pirajno F., Zhang Z. H., Chai F. M., Wu H., Chen S. P., Cheng L. S., Yang J. M. and Zhang C. Q. (2008) A review of the Cu-Ni sulphide deposits in the Chinese Tianshan and Altay orogens (Xinjiang Autonomous Region, NW China): Principal characteristics and ore-forming processes. *J. Asian Earth Sci.* **32**, 184–203.

Marchesi C., Garrido C. J., Harvey J., González-Jiménez J. M., Hidas K., Lorand J. P. and Gervilla F. (2013) Platinum-group elements, S, Se and Cu in highly depleted abyssal peridotites from the Mid-Atlantic Ocean Ridge (ODP Hole 1274A): Influence of hydrothermal and magmatic processes. *Contrib. to Mineral. Petrol.* **166**, 1521–1538.

Maréchal C. N., Télouk P. and Albarède F. (1999) Precise analysis of copper and zinc isotopic compositions by plasma-source mass spectrometry. *Chem. Geol.* **156**, 251–273.

Mathur R. and Fantle M. S. (2015) Copper isotopic perspectives on supergene processes: Implications for the global Cu cycle. *Elements* **11**, 323–329.

Mathur R., Titley S., Barra F., Brantley S., Wilson M., Phillips A., Munizaga F., Maksaev V., Vervoort J. and Hart G. (2009) Exploration potential of Cu isotope fractionation in porphyry copper deposits. J.

*Geochemical Explor.* **102**, 1–6.

Mathur R., Dendas M., Titley S. and Phillips A. (2010) Patterns in the copper isotopic composition of minerals in porphyry copper deposits in southwestern United States. *Econ. Geol.* **105**, 1457–1467.

Mathur R., Jin L., Prush V., Paul J., Ebersole C., Fornadel A., Williams J. Z. and Brantley S. (2012) Cu isotopes and concentrations during weathering of black shale of the Marcellus Formation, Huntingdon County, Pennsylvania (USA). *Chem. Geol.* **304-305**, 175–184.

McDonough W. F. and Sun S. (1995) The composition of the Earth. *Chem. Geol.* **120**, 223–253.

Michalak P. and Nowak M. (2010) Accessory minerals from mantle xenoliths from Wołek Hill and Wilcza Góra. *Mineral. - Spec. Pap.* **37**, 94–95.

Miller A., Figueroa L. and Wildeman T. (2011) Zinc and nickel removal in simulated limestone treatment of mining influenced water. *Appl. Geochemistry* **26**, 125–132.

Miller J. (2007) Sulfide Mineralization at Site 1268, Mid-Atlantic Ridge, Ocean Drilling Program Leg 209. *Proc. Ocean Drill. Program, 209 Sci. Results* **209**, 1–18.

Miller J. and Cervantes P. (2002) Sulfide mineral chemistry and petrography and platinum group element composition in gabbroic rocks from the Southwest Indian Ridge. In *Proceedings of the Ocean Drilling Program, Scientific Results* pp. 1–29.

Mirnejad H., Mathur R., Einali M., Dendas M. and Alirezaei S. (2010) A comparative copper isotope study of porphyry copper deposits in Iran. *Geochemistry Explor. Environ. Anal.* **10**, 413–418.

Misra K. C. and Fleet M. E. (1974) Chemical Composition and Stability of Violarite. *Econ. Geol.* **69**, 391–403.

Morishita T., Hara K., Nakamura K., Sawaguchi T., Tamura A., Arai S., Okino K., Takai K. and Kumagai H. (2009) Igneous, Alteration and Exhumation Processes Recorded in Abyssal Peridotites and Related Fault Rocks from an Oceanic Core Complex along the Central Indian Ridge. *J. Petrol.* **50**, 1299–1325.

Muller M. R. (1997) Thin crust beneath ocean drilling program borehole 735B at the Southwest Indian Ridge? *Earth Planet. Sci. Lett.* **148**, 93–107.

Nedimović M. R., Carbotte S. M., Harding A. J., Detrick R. S., Canales J. P., Diebold J. B., Kent G. M., Tischer M. and Babcock J. M. (2005) Frozen magma lenses below the oceanic crust. *Nature* **436**, 1149–1152.

Negishi H., Arai S., Yurimoto H., Ito S., Ishimaru S., Tamura A. and Akizawa N. (2013) Sulfide-rich dunite within a thick Moho transition zone of the northern Oman ophiolite: Implications for the origin of Cyprus-type sulfide deposits. *Lithos* **164-167**, 22–35.

Nicolas A. (1995) *The Mid-Oceanic Ridges: Mountains Below Sea Level*., Springer, Berlin.

Nicolas A., Bouldier F., Ildefonse B. and Ball E. (2000) Accretion of Oman and United Arab Emirates ophiolite - Discussion of a new structural map. *Mar. Geophys. Res.* **21**, 147–179.

Niu Y. (2004) Bulk-rock major and trace element compositions of abyssal peridotites: Implications for mantle melting, melt extraction and post-melting processes beneath Mid-Ocean ridges. *J. Petrol.* **45**, 2423–2458.

O’Hanley D. S. and Wicks F. J. (1995) Conditions of formation of lizardite, chrysotile and antigorite, Cassiar, British Columbia. *Can. Mineral.* **33**, 753–773.

O’Neill H. S. C. and Mavrogenes J. A. (2002) The Sulfide Capacity and the Sulfur Content at Sulfide Saturation of Silicate Melts at 1400°C and 1 bar. *J. Petrol.* **43**, 1049–1087.

Panayiotou A. (1978) The mineralogy and chemistry of the podiform chromite deposits in the serpentinites of the Limassol Forest, Cyprus. *Miner. Depos.* **13**, 259–274.

Panayiotou A. (1980) Cu-Ni-Co-Fe sulfphide mineralization, Limassol Forest, Cyprus. In *Ophiolites, proceeding international ophilite symposium* (ed. A. Panayiotou). Cyprus. pp. 102–116.

Patten C., Barnes S.-J., Mathez E. A. and Jenner F. E. (2013) Partition coefficients of chalcophile elements between sulfide and silicate melts and the early crystallization history of sulfide liquid: LA-ICP-MS analysis of MORB sulfide droplets. *Chem. Geol.* **358**, 170–188.

Paulick H., Bach W., Godard M., De Hoog J. C. M., Suhr G. and Harvey J. (2006) Geochemistry of abyssal peridotites (Mid-Atlantic Ridge, 15°20′N, ODP Leg 209): Implications for fluid/rock interaction in slow spreading environments. *Chem. Geol.* **234**, 179–210.

Peltonen P., Kontinen A., Huhma H. and Kuronen U. (2008) Outokumpu revisited: New mineral deposit model for the mantle peridotite-associated Cu-Co-Zn-Ni-Ag-Au sulphide deposits. *Ore Geol. Rev.* **33**, 559–617.

Pertsev A. N., Bortnikov N. S., Vlasov E. A., Beltenev V. E., Dobretsova I. G. and Ageeva O. A. (2012)

Recent massive sulfide deposits of the Semenov ore district, Mid-Atlantic Ridge, 13°31′ N: Associated rocks of the oceanic core complex and their hydrothermal alteration. *Geol. Ore Depos.* **54**, 334–346.

Petersen S. and Hein J. R. (2013) The Geology of Sea-Floor Massive Sulphides. In *Deep Sea Minerals: Sea-Floor Massive Sulphides, a physical, biological, environmental, and technical review.* (eds. E. Baker and Y. Beaudoin). Secretariat of the Pacific Community. pp. 7–18.

Petersen S., Kuhn K., Kuhn T., Augustin N., Hékinian R., Franz L. and Borowski C. (2009) The geological setting of the ultramafic-hosted Logatchev hydrothermal field (14°45′N, Mid-Atlantic Ridge) and its influence on massive sulfide formation. *Lithos* **112**, 40–56.

Piccardo G. B., Zanetti A. and Müntener O. (2007) Melt/peridotite interaction in the Southern Lanzo peridotite: Field, textural and geochemical evidence. *Lithos* **94**, 181–209.

Pieterek B., Ciazela J., Koepke J., Strauss H., Dick H., Duczmal-Czernikiewicz A., Bender M. and Muszyński A. (2017) Layer boundaries attract sulfides throughout the igneous layering of the lower oceanic crust : IODP Hole U1473A, Atlantis Bank, Southwest Indian Ridge. *Mineral. - Spec. Pap.* **47**, 36.

Pouchou J.-L. and Pichoir F. (1991) Quantitative Analysis of Homogeneous or Stratified Microvolumes Applying the Model "PAP." In *Electron Probe Quantitation* (eds. K. F. J. Heinrich and D. E. Newbury). Springer US, Boston, MA. pp. 31–75.

Prendergast M. D. (2012) The Molopo Farms Complex, Southern Botswana - A reconsideration of structure, evolution, and the bushveld connection. *South African J. Geol.* **115**, 77–90.

Rampone E., Piccardo G. B., Vannucci R. and Bottazzi P. (1997) Chemistry and origin of trapped melts in ophioiitic peridotites. *Geochim. Cosmochim. Acta* **61**, 4557–4569.

Rehkämper M., Halliday A. N., Alt J., Fitton J. G., Zipfel J. and Takazawa E. (1999) Non-chondritic platinum-group element ratios in oceanic mantle lithosphere: petrogenetic signature of melt percolation? *Earth Planet. Sci. Lett.* **172**, 65–81.

Rouxel O., Fouquet Y. and Ludden J. N. (2004) Copper isotope systematics of the Lucky Strike, Rainbow, and Logatchev sea-floor hydrothermal fields on the Mid-Atlantic Ridge. *Econ. Geol.* **99**, 585–600.

Saalmann K. and Laine E. L. (2014) Structure of the Outokumpu ore district and ophiolite-hosted Cu-Co-

Zn-Ni-Ag-Au sulfide deposits revealed from 3D modeling and 2D high-resolution seismic reflection data. *Ore Geol. Rev.* **62**, 156–180.

Saalmann K. and Laine E. (2015) Structure of the ophiolite-hosted Outokumpu Cu – Co – Zn – Ni – Ag – Au sulfide ore district revealed by combined 3D modelling and 2D high-resolution seismic reflection data. *Geophys. Res. Abstr.* **17**, EGU2015–1437.

Sanfilippo A., Dick H. J. B. and Ohara Y. (2013) Melt-Rock Reaction in the Mantle: Mantle Troctolites from the Parece Vela Ancient Back-Arc Spreading Center. *J. Petrol.* **54**, 861–885.

Sanfilippo A., Morishita T., Kumagai H., Nakamura K., Okino K., Hara K., Tamura A. and Arai S. (2015) Hybrid troctolites from mid-ocean ridges: inherited mantle in the lower crust. *Lithos* **232**, 124–130.

Sanfilippo A., Morishita T. and Senda R. (2016) Rhenium-osmium isotope fractionation at the oceanic crust-mantle boundary. *Geology* **44**, 167–170.

Savage P., Harvey J. and Moynier F. (2014) Copper isotope heterogeneity in the lithospheric mantle. In *Goldschmidt Conference Abstracts* p. 2192.

Schwartz S., Guillot S., Reynard B., Lafay R., Debret B., Nicollet C., Lanari P. and Auzende A. L. (2013) Pressure-temperature estimates of the lizardite/antigorite transition in high pressure serpentinites. *Lithos* **178**, 197–210.

Seewald J. S. and Seyfried W. E. (1990) The effect of temperature on metal mobility in subseafloor hydrothermal systems: constraints from basalt alteration experiments. *Earth Planet. Sci. Lett.* **101**, 388–403.

Seyler M., Lorand J.-P., Dick H. J. B. and Drouin M. (2007) Pervasive melt percolation reactions in ultra-depleted refractory harzburgites at the Mid-Atlantic Ridge, 15° 20′N: ODP Hole 1274A. *Contrib. to Mineral. Petrol.* **153**, 303–319.

Song X. Y., Keays R. R., Zhou M. F., Qi L., Ihlenfeld C. and Xiao J. F. (2009) Siderophile and chalcophile elemental constraints on the origin of the Jinchuan Ni-Cu-(PGE) sulfide deposit, NW China. *Geochim. Cosmochim. Acta* **73**, 404–424.

Suhr G., Hellebrand E., Johnson K. and Brunelli D. (2008) Stacked gabbro units and intervening mantle: A detailed look at a section of IODP Leg 305, Hole U1309D. *Geochemistry, Geophys. Geosystems* **9**, Q10007.

Sun S. (1982) Chemical composition and origin of the earth's primitive mantle. *Geochim. Cosmochim. Acta* **46**, 179–192.

Tamura A., Arai S., Ishimaru S. and Andal E. S. (2008) Petrology and geochemistry of peridotites from IODP Site U1309 at Atlantis Massif, MAR 30°N: micro- and macro-scale melt penetrations into peridotites. *Contrib. to Mineral. Petrol.* **155**, 491–509.

Thalhammer O., Stumpfl E. F. and Panayiotou A. (1986) Postmagmatic, hydrothermal origin of sulfide and arsenide mineralizations at Limassol Forest, Cyprus. *Miner. Depos.* **21**, 95–105.

Tivey M., Tucholke B. E. and Dick H. J. B. (2004) *Kane Megamullion 2004, Cruise Rep. KN180-2.*, Woods Hole Oceanographic Institution, Woods Hole, Mass., US.

Tsujimura T. and Kitakaze A. (2005) Experimental study of sulfur solubility in silicate melts coexisting with graphite as a function of silicate melt composition. *Resour. Geol.* **55**, 55–60.

Tucholke B. E. and Lin J. (1994) A Geological Model for the Structure of Ridge Segments in Slow-Spreading Ocean Crust. *J. Geophys. Res.* **99**, 11937–11958.

Tucholke B. E., Lin J. and Kleinrock M. C. (1998) Megamullions and mullion structure defining oceanic metamorphic core complexes on the Mid-Atlantic Ridge. *J. Geophys. Res.* **103**, 9857–9866.

Tucholke B. E., Humphris S. E. and Dick H. J. B. (2013) Cemented mounds and hydrothermal sediments on the detachment surface at Kane Megamullion: A new manifestation of hydrothermal venting. *Geochemistry, Geophys. Geosystems* **14**, 3352–3378.

U.S. Geological Survey (2016) Mineral Commodities Summaries. *Miner. Commod. Summ.*, 202.

Ulmer P. and Trommsdorff V. (1995) Serpentine Stability to Mantle Depths and Subduction-Related Magmatism. *Science* **268**, 858–861.

Vance D., Archer C., Bermin J., Perkins J., Statham P. J., Lohan M. C., Ellwood M. J. and Mills R. A. (2008) The copper isotope geochemistry of rivers and the oceans. *Earth Planet. Sci. Lett.* **274**, 204–213.

Vaughan D. J. and Corkhill C. L. (2017) Mineralogy of sulfides. *Elements* **13**, 81–87.

Wang K. L., O'Reilly S. Y., Griffin W. L., Pearson N. J. and Zhang M. (2009) Sulfides in mantle peridotites from Penghu Islands, Taiwan: Melt percolation, PGE fractionation, and the lithospheric evolution of the South China block. *Geochim. Cosmochim. Acta* **73**, 4531–4557.

Watmuff I. G. (1974) Supergene alteration of the Mt Windarra nickel sulphide ore deposit, Western Australia. *Miner. Depos.* **9**, 199–221.

White W. M. and Klein E. M. (2013) Composition of the Oceanic Crust. In *Treatise on Geochemistry: Second Edition* Elsevier Ltd. pp. 457–496.

Wittke J. H., Haxel G. B., Epstein G. S. and Jacobson C. E. (2016) and Intermetallic Minerals in an Unusual Inland Tectonic Setting, Southwest Arizona. *Geol. Soc. Am. Abstr. with Programs* **48**, 25: 2.

Xu M., Canales J. P., Tucholke B. E. and DuBois D. L. (2009) Heterogeneous seismic velocity structure of the upper lithosphere at Kane oceanic core complex, Mid-Atlantic Ridge. *Geochemistry, Geophys. Geosystems* **10**, Q10001.

Zhang Z. and Hirschmann M. M. (2016) Experimental constraints on mantle sulfide melting up to 8 GPa. *Am. Mineral.* **101**, 181–192.

Zhu X. K., O'Nions R. K., Guo Y., Belshaw N. S. and Rickard D. (2000) Determination of natural Cu-isotope variation by plasma-source mass spectrometry: Implications for use as geochemical tracers. *Chem. Geol.* **163**, 139–149.

## FIGURE CAPTIONS

**Fig. 1.** Geology of the Kane Fracture Zone (KFZ) and the Kane Megamullion ocean core complex (OCC). Our samples have been collected along the walls of the Eastern and Western Faults. ODP – Ocean Drilling Program, MAR – Mid-Atlantic Ridge.

**Fig. 2.** Representative samples of basement rocks from below detachment shear zones used in our study: spinel harzburgite (112-71), plagioclase harzburgite (28-9A), peridotite-gabbro contact (19-11) and dunite (113-41B).

**Fig. 3.** Sample 21-9 showing the mantle-gabbro contact 21-9T. A) Microphotography of the entire thin section in plane-polarized transmitted light. The red hexagons show the location of large sulfides (40-120 µm). Orange boxes (I-IV) outline selected areas where we investigated for the presence of medium sulfides (10-40 µm; yellow dots). B & C) X-ray map of orange box II for S and Al. The colors correspond to the X-ray intensity on the S Kα and Al Kα lines. The brightest points on the S image forming the ~1-mm-wide subvertical band are tiny sulfides dispersed in the antigorite-chrysotile matrix (see Section 5.5). Note that most of these sulfides crystallize where the Al-concentration gradient is the steepest. The Al

concentration measured by EPM in the dark orange/brown area corresponding to ~30 counts (see the side bar) is 2.5 wt%. This area corresponds to the yellow part of the contact zone visible in Picture A.

**Fig. 4.** MgO, $Al_2O_3$, Ni and Zn versus Cu and S contents of the Kane Megamullion spinel and plagioclase harzburgites, dunite, and peridotite-gabbro contacts.

**Fig. 5.** Mean Cu concentration of the Kane Megamullion (KM) plagioclase (Pl) harzburgites compared to the mean concentration of the KM spinel (Sp) harzburgites and various orogenic spinel harzburgites. Primitive mantle estimate is also plotted as a reference line (30 ppm; Sun 1982). Error bars represent 1 standard error of the mean (SE). Where the bars are not visible, 1 SE is <4 ppm. Source of data for orogenic peridotites: Lanzo (Lorand et al., 1993), Western Pyrenean Massif (Lorand, 1991), Eastern Pyrenean Massif (Lorand, 1989a), Baldissero, Balmuccia, and Finero (Garuti et al., 1984).

**Fig. 6.** Whole-rock Cu versus S concentrations of the Kane Megamullion spinel (Sp) and plagioclase (Pl) harzburgites, mantle-gabbro contacts, and dunites. PM is the theoretical primitive mantle (Sun, 1982). DMM is theoretical depleted mantle (see Section 5.1). The pink dots labeled with 6% and 17% represent the maximum and minimum degree of melting in the Kane Megamullion spinel harzburgites. RM is the theoretical refertilized mantle defined as formed through addition of melt-derived sulfides containing between 3.5 (~10% of chalcopyrite in sulfide grains) and 35 wt% Cu (~100% chalcopyrite) into DMM. Note that even the addition of Cu-rich sulfides would not reproduce the observed Cu-S concentrations in the refertilized mantle. These can only be explained with subsequent desulfurization during serpentinization (see Section 5.5).

**Fig. 7.** Nickel and Cu contents of pentlandites (Pn) and heazlewoodites (Hz) from the mantle-gabbro contact in sample 21-9 (see Fig. 3). Lizardite, antigorite, chrysotile, tremolite, chlorite and prehnite have been identified by optical microscope and X-ray diffraction. The Ni content of the sulfides attains the maximum value on the gabbro side and gradually lowers towards the peridotite side. Although the sulfides are secondary their Cu contents seem to match the whole-rock Cu concentrations. Hence, the Cu concentrations are the highest in the sulfides from the contact zone (the antigorite/chrysotile and chlorite domains), whereas those from the gabbro and peridotite are very low.

**Fig. 8.** Photomicrographs of our two most common chalcopyrite parageneses in our sample suite in cross-polarized (A) and plane polarized reflected light (B): A) Inclusion of chalcopyrite (inset) in plagioclase from a peridotite-gabbro contact in sample 21-7. The broad picture is taken in transmitted cross-polarized light. The inset image is taken in reflected plane-polarized light. B) Polysulfide composed of chalcopyrite (Ccp), pyrrhotite (Po) and pentlandite (Pn) from a peridotite-gabbro contact in sample 21-7. Note that

chalcopyrite in the middle of the grain is preserved, whereas chalcopyrite in the rim has been altered to a Fe-Cu hydroxide (31.8 wt% Fe, 13.0 wt% Cu, but only 0.3 wt% S).

**Fig. 9.** Primitive mantle-normalized multi-element diagram of Kane Megamullion sulfides. The normalization values are from McDonough and Sun (1995). A) Pentlandite compared to primary sulfides (chalcopyrite and pyrrhotite). Note that Cu, Zn, Bi, Ga, Cd show affinity to chalcopyrite, whereas Pb, Co, Ni, Ag, Sb, Ge, and As show affinity to pentlandite, and As and Tl to pyrrhotite. The concentrations of As, Sb, Ge, As and Tl in chalcopyrite are under detection limit. B) Pentlandite compared to secondary Ni sulfides (heazlewoodite, millerite, and godlevskite). C) Secondary pentlandite from peridotite-gabbro contacts compared to the secondary pentlandites away from the contact zones and the primary pentlandites. Note that the three types represent the similar pattern but the secondary pentlandite from peridotite-gabbro contact is most enriched in chalcophile elements.

**Fig. 10.** Concentrations of selected chalcophile elements along the laser ablation profile composed of 18 parallel lines across the mantle-gabbro contact in sample 21-9. Note that all chalcophile elements show higher concentrations within the contact. Most of them are highly concentrated in the peridotite portion of the contact (yellow lithology). Zinc is unique as it is enriched in the gabbro part of the contact (white lithology). Arsenic is anomalous as it shows two major peaks.

**Fig. 11.** Copper and zinc concentrations in serpentine minerals of spinel (Sp) harzburgites, plagioclase (Pl) harzburgites, and peridotite-gabbro contacts from the Kane Megamullion measured with LA-ICPMS.

**Fig. 12.** The $\delta^{65}$Cu range of the Kane Megamullion chalcopyrite measured in this study compared to Mid-Ocean Ridge Basalts (MORB; Ben Othman et al., 2006, Rouxel et al., 2004), fresh and altered mantle, as well as other settings. Sea-floor hydrothermal vents data from Rouxel et al. (2004). Marine sediments data from Marechal et al. (1999). Pore waters data from Mathur et al. (2012). Seawater data from Vance et al. (2008). Supergene systems from Mathur and Fantle (2015).The grey field indicates the terrestrial range for igneous copper (after Ikehata and Hirata, 2012).

**Table 1.** Major element contents (wt%) and Mg#s of Kane Megamullion peridotites.

| Label | Material | $SiO_2$ | $TiO_2$ | $Al_2O_3$ | $Fe_2O_3$* | MnO | MgO | CaO | $Na_2O$ | $K_2O$ | $P_2O_5$ | LOI | Total | Mg# |
|---|---|---|---|---|---|---|---|---|---|---|---|---|---|---|
| *Depleted mantle samples* | | | | | | | | | | | | | | |
| 5-1 | Sp harzburgite | 38.6 | 0.02 | 1.21 | 9.07 | 0.13 | 36.0 | 1.25 | 0.07 | 0.01 | 0.04 | 12.9 | 99.3 | 0.89 |
| 5-31A | Sp harzburgite | 38.9 | 0.12 | 1.41 | 10.15 | 0.13 | 36.4 | 0.56 | 0.02 | 0.02 | 0.02 | 11.6 | 99.3 | 0.88 |
| 14-44 | Sp harzburgite | 39.1 | 0.01 | 1.33 | 8.29 | 0.09 | 36.2 | 0.62 | 0.11 | 0.02 | 0.01 | 13.3 | 99.3 | 0.90 |
| 14-70 | Sp harzburgite | 40.0 | 0.05 | 2.06 | 9.83 | 0.12 | 34.7 | 1.12 | 0.15 | 0.05 | 0.01 | 11.1 | 99.3 | 0.87 |
| 17-17 | Sp harzburgite | 38.7 | 0.02 | 1.33 | 8.00 | 0.10 | 36.8 | 0.29 | 0.06 | 0.02 | 0.02 | 13.8 | 99.3 | 0.90 |
| 19-10A | Sp harzburgite | 34.8 | 0.02 | 1.06 | 8.54 | 0.17 | 32.5 | 5.87 | 0.08 | 0.02 | 0.03 | 16.1 | 99.3 | 0.88 |
| 19-11A | Sp harzburgite | 39.3 | 0.02 | 1.68 | 8.31 | 0.13 | 35.9 | 0.34 | 0.10 | 0.03 | 0.03 | 13.3 | 99.2 | 0.90 |

| | | | | | | | | | | | | | | |
|---|---|---|---|---|---|---|---|---|---|---|---|---|---|---|
| 19-18A | Sp harzburgite | 37.6 | 0.04 | 1.58 | 11.31 | 0.16 | 33.5 | 1.81 | 0.14 | 0.03 | 0.07 | 12.9 | 99.2 | 0.85 |
| 19-31 | Sp harzburgite | 36.5 | 0.02 | 1.71 | 9.38 | 0.15 | 31.6 | 5.28 | 0.15 | 0.01 | 0.07 | 14.1 | 99.1 | 0.87 |
| 112-44A | Sp harzburgite | 39.4 | 0.01 | 1.04 | 8.20 | 0.12 | 37.7 | 0.30 | - | - | 0.01 | 12.5 | 99.3 | 0.90 |
| 112-49 | Sp harzburgite | 39.7 | 0.02 | 1.37 | 8.47 | 0.11 | 37.1 | 0.54 | 0.02 | 0.01 | 0.02 | 11.9 | 99.3 | 0.90 |
| 112-71 | Sp harzburgite | 40.4 | 0.02 | 1.35 | 8.25 | 0.15 | 36.0 | 0.33 | 0.11 | 0.03 | 0.03 | 12.6 | 99.3 | 0.90 |
| 112-84 | Sp harzburgite | 42.2 | 0.02 | 1.45 | 8.51 | 0.13 | 40.3 | 1.16 | - | 0.01 | 0.00 | 5.4 | 99.2 | 0.90 |
| 113-40 | Sp harzburgite | 36.1 | 0.01 | 1.09 | 7.80 | 0.07 | 34.3 | 4.66 | 0.07 | 0.03 | 0.02 | 15.1 | 99.3 | 0.90 |
| 113-55A | Sp harzburgite | 40.4 | 0.12 | 1.78 | 15.09 | 0.20 | 33.8 | 1.79 | 0.16 | 0.02 | 0.09 | 5.8 | 99.3 | 0.82 |
| 113-57A | Sp harzburgite | 39.3 | 0.02 | 1.37 | 8.16 | 0.12 | 37.6 | 0.06 | 0.08 | 0.01 | 0.01 | 12.6 | 99.3 | 0.90 |
| 113-59A | Sp harzburgite | 38.5 | 0.01 | 1.07 | 10.52 | 0.14 | 36.9 | 0.03 | 0.05 | 0.01 | 0.01 | 12.2 | 99.4 | 0.87 |
| 114-9 | Sp harzburgite | 57.8 | 0.01 | 0.95 | 7.06 | 0.02 | 28.6 | 0.01 | 0.08 | 0.01 | 0.01 | 4.9 | 99.4 | 0.89 |
| 114-19A | Sp harzburgite | 39.3 | 0.02 | 1.33 | 8.23 | 0.11 | 37.5 | 0.40 | 0.02 | 0.01 | 0.01 | 12.4 | 99.3 | 0.90 |
| *Melt-modified mantle samples* | | | | | | | | | | | | | | |
| 19-11B | m-g contact | 25.7 | 0.35 | 3.00 | 39.33 | 0.56 | 14.0 | 3.50 | 0.40 | 0.06 | 0.85 | 11.2 | 98.9 | 0.41 |
| 21-7 | m-g contact | 31.6 | 0.16 | 4.04 | 25.70 | 0.36 | 23.1 | 3.62 | 0.36 | 0.04 | 0.36 | 9.8 | 99.1 | 0.64 |
| 21-9A | Pl harzburgite | 38.7 | 0.03 | 1.10 | 8.78 | 0.10 | 37.3 | 0.30 | 0.05 | 0.01 | 0.02 | 12.8 | 99.3 | 0.89 |
| 28-9A | Pl harzburgite | 37.6 | 0.03 | 1.54 | 11.75 | 0.14 | 34.3 | 0.88 | 0.13 | 0.05 | 0.07 | 12.7 | 99.2 | 0.85 |
| 112-10 | Pl harzburgite | 39.3 | 0.03 | 1.09 | 8.25 | 0.08 | 37.1 | 0.08 | 0.05 | 0.02 | 0.02 | 13.4 | 99.4 | 0.90 |
| 112-116 | Pl harzburgite | 39.2 | 0.02 | 1.48 | 8.15 | 0.11 | 37.3 | 0.04 | 0.04 | 0.01 | 0.01 | 12.9 | 99.3 | 0.90 |
| 113-41B | dunite | 29.4 | 0.00 | 0.66 | 8.06 | 0.15 | 29.5 | 11.48 | 0.04 | 0.01 | 0.04 | 19.7 | 99.2 | 0.88 |
| *Early mantle veins* | | | | | | | | | | | | | | |
| 5-31-B | Ol websterite | 48.4 | 0.00 | 3.36 | 8.69 | 0.13 | 30.1 | 6.05 | 0.12 | 0.02 | 0.01 | 3.5 | 98.7 | 0.90 |

$Fe_2O_3$* = Total Fe as $Fe_2O_3$. LOI – loss-on-ignition. Mg# = [molar Mg/(molar Mg + molar Fe)] x 100. Sp – spinel, Pl – plagioclase, m-g – mantle-gabbro, Ol – olivine. (-) below detection limit.

**Table 2.** Chalcophile element contents of Kane Megamullion peridotites.

| | | Concentration (ppm) | | | | | | | | | | Concentration (ppb) | | | |
|---|---|---|---|---|---|---|---|---|---|---|---|---|---|---|---|
| Label | Material | S | Cu | As | Zn | Ga | Pb | Se | Sb | Tl | Ni | Au | Ag | Bi | Cd |
| *Depleted mantle samples* | | | | | | | | | | | | | | | |
| 5-1 | Sp harzburgite | 159 | 40 | 35 | 68 | 1.6 | 0.5 | 2.6 | 1.5 | 0.24 | 1860 | - | - | - | 100 |
| 5-31-A | Sp harzburgite | 142 | 17 | 3 | 56 | 11.7 | 0.6 | 0.5 | - | 0.06 | 1120 | - | - | - | - |
| 14-44 | Sp harzburgite | 142 | 7 | 11 | 47 | 1.9 | - | 0.4 | 0.4 | 0.36 | 2050 | - | - | - | - |
| 14-70 | Sp harzburgite | 81 | 9 | 5 | 43 | 3.9 | - | 0.3 | - | 0.13 | 1800 | - | - | - | - |
| 17-17 | Sp harzburgite | 210 | 47 | 29 | 101 | 2 | - | 0.6 | 0.5 | 0.24 | 1590 | - | - | - | - |
| 19-10A | Sp harzburgite | 188 | 39 | 22 | 91 | 1.8 | - | 0.2 | 0.7 | 1.96 | 1810 | - | - | 20 | 100 |
| 19-11A | Sp harzburgite | 283 | 69 | 20 | 110 | 2.2 | 0.8 | 0.8 | 0.9 | 0.39 | 1720 | - | - | - | - |
| 19-18A | Sp harzburgite | 81 | 52 | 45 | 126 | 2.3 | 1.1 | 1.2 | 1.4 | 1.58 | 1870 | - | - | 70 | - |
| 19-31 | Sp harzburgite | 215 | 59 | 45 | 111 | 2.4 | 0.7 | - | 2.1 | 1.71 | 1900 | - | - | 30 | - |
| 112-44A | Sp harzburgite | 241 | 11 | 5 | 72 | 1.2 | 0.7 | 1.6 | 0.3 | 0.14 | 1930 | - | - | - | - |
| 112-49 | Sp harzburgite | 332 | 52 | 17 | 69 | 1.4 | 0.8 | 0.7 | 0.8 | 0.26 | 1670 | - | - | 20 | - |
| 112-71 | Sp harzburgite | 84 | 21 | 23 | 82 | 2.1 | 0.9 | - | 1.4 | 0.28 | 1300 | - | - | - | - |
| 112-84 | Sp harzburgite | 184 | 38 | 3 | 67 | 1.5 | 1.5 | - | - | - | 2030 | - | - | - | - |
| 113-40 | Sp harzburgite | 129 | 14 | 25 | 50 | 1.2 | 0.6 | 0.1 | 0.3 | 0.63 | 1230 | - | - | - | - |
| 113-55A | Sp harzburgite | 561 | 21 | 22 | 127 | 3 | 1.0 | - | 1.8 | 3.30 | 1600 | - | - | - | - |
| 113-57A | Sp harzburgite | 32 | 25 | 10 | 115 | 1.8 | 0.8 | - | 0.4 | 0.41 | 1110 | - | - | - | - |
| 113-59A | Sp harzburgite | 45 | 23 | 9 | 171 | 1.6 | 0.9 | - | 0.4 | 0.70 | 1400 | - | - | - | - |
| 114-9 | Sp harzburgite | - | 8 | 5 | 36 | 2 | 0.6 | 0.2 | 0.3 | - | 1380 | - | - | 20 | - |
| 114-19A | Sp harzburgite | 212 | 24 | 13 | 55 | 1.8 | 1.2 | - | 0.5 | 0.58 | 1610 | - | 90 | 100 | - |
| *Melt-modified mantle samples* | | | | | | | | | | | | | | | |
| 19-11B | m-g contact | 488 | 284 | 371 | 462 | 8.2 | 1.2 | 1.4 | 22.0 | 9.87 | 1180 | - | - | - | 500 |
| 21-7A | m-g contact | 283 | 304 | 134 | 246 | 5.4 | 1.0 | 0.5 | 7.9 | 2.36 | 1050 | - | - | - | 200 |

| | | | | | | | | | | | | | | | |
|---|---|---|---|---|---|---|---|---|---|---|---|---|---|---|---|
| 21-9A | Pl harzburgite | 182 | 139 | 18 | 66 | 1.9 | 1.0 | 0.6 | 0.8 | 0.88 | 1620 | - | - | - | - |
| 28-9A | Pl harzburgite | 206 | 147 | 44 | 125 | 2.4 | 1.6 | 1.2 | 1.8 | 3.21 | 1400 | - | 80 | 70 | 100 |
| 112-10 | Pl harzburgite | 159 | 155 | 9 | 75 | 1.3 | 0.8 | 0.9 | 0.6 | 0.27 | 1680 | 7 | - | - | 100 |
| 112-116 | Pl harzburgite | 90 | 82 | 5 | 96 | 2.1 | 0.7 | - | - | 0.23 | 1230 | 11 | - | - | - |
| 113-41B | dunite | 226 | 118 | 26 | 124 | 1.6 | 1.0 | - | 1.8 | 0.62 | 669 | - | 60 | - | - |
| *Early mantle veins* | | | | | | | | | | | | | | | |
| 5-31-B | Ol websterite | n/a | 157 | 3.1 | 54 | 3.6 | 0.7 | 1.1 | - | - | 1950 | - | - | 20 | - |
| Detection limit: | | 9 | 0.2 | 0.5 | 0.5 | 0.1 | 0.5 | 0.1 | 0.1 | 0.05 | 0.5 | 2 | 50 | 20 | 100 |

Sp – spinel, Pl – plagioclase, m-g – mantle-gabbro, Ol – olivine; (-) below detection limit.

**Table 3.** Copper isotope values of chalcopyrite from sample 21-7 from the Kane Megamullion OCC

| Sulfide ID | $\delta^{65}$Cu (‰) | ± 2σ (‰)[a] | Beam size (µm) | Laser frequency (Hz) | n |
|---|---|---|---|---|---|
| *Sample* | | | | | |
| cb3 | 0.26 | 0.16 | 10 | 83 | 1 |
| cb23 | 0.18 | 0.09 | 10 | 100 | 1 |
| ha3 | -0.04 | 0.15 | 10 | 100 | 1 |
| ha4 | 0.29 | 0.18 | 10 | 100 | 1 |
| *Standard* | | | | | |
| cpy2 | 0.11 | 0.05 | 40 | 10 | 4 |
| cpy2 | 0.10 | 0.08 | 10 | 10 | 4 |

[a] calculated by the propagation of the within-run relative standard error of the sample and the within-run relative standard errors of the two bracketing standards (Cu NIST SRM 976).

**Table 4.** Summary of sulfide phases based on ore microscopy.

| Lithology | Sample | Ccp | Po | Pn | Py | Viol | Hz | Gs | Mi |
|---|---|---|---|---|---|---|---|---|---|
| spinel harzburgite | 5-1 | − | − | + | − | − | − | − | − |
| | 14-44 | − | − | − | − | − | − | − | − |
| | 19-11A | − | − | − | − | − | − | − | − |
| plagioclase harzburgite | 21-9A | − | − | + + | − | − | − | − | − |
| | 28-9A | − | − | + | − | − | − | − | − |
| | 112-10 | − | + + | + | + | − | − | − | − |
| mantle-gabbro contacts | 19-11T | − | + + + | − | − | − | − | − | − |
| | 21-7 | + + | + + + | + + + | − | + | − | − | − |
| | 21-9T | − | − | + + + | − | − | + + | + | + |
| dunite | 113-41B | − | − | − | − | − | − | − | − |
| olivine websterite | 5-31B | + + | + + + | + + + | − | + | − | − | − |
| gabbro | 19-11B | − | − | − | − | − | − | − | − |
| | 21-9B | − | − | − | − | − | + | − | − |

Sulfide abbreviations: Pn, pentlandite; Po, pyrrhotite; Ccp, chalcopyrite; Hz, heazlewoodite; Viol, violarite; Py, pyrite; Gs, godlevskite; Mi, millerite. A number of sulfide grains in a thin section: (−) absent, (+) 1-4 sulfide grains, (+ +) 5-20 sulfide grains; (+ + +) >20 sulfide grains. The samples with a letter suffix occupy only a fraction of the standard thin section size, i.e. 19-11A (~25%), 19-11B (~40%), 19-11T (~35%), 21-9A (~65%), 21-9B (~30%), 21-9T (~5%), 28-9A (~25%). Note that sulfides are least abundant in spinel peridotites, medium abundant in plagioclase peridotites and most abundant in mantle-gabbro contacts.

# APPENDIX

## *A. Trace element compositions of the Kane Megamullion sulfides*

**Table A.1.** Chalcophile element concentrations (ppm) of selected Kane Megamullion sulfides determined by a femtosecond-laser ablation-inductively coupled plasma-mass spectrometer.

|  | 5-31A |  |  |  |  |  |  |  |  |  | 19-11B |  |  |  |
|---|---|---|---|---|---|---|---|---|---|---|---|---|---|---|
|  | ca29/30 | cb12 | cc20-23 | oa19-21 | oa17 | oa18 | oa27-29 | sa3/4 | sa5/6 | sa20 | od1 | od2 | odn1 | odn2 |
| Mineral | Pn | Ccp | Pn | Pn | Po | Po | Po | Pn | Pn | Pn | Po | Po | Po | Po |
| Co | 6445 | 176 | 6667 | 4318 | 13 | 11 | 62 | 4794 | 4843 | 5242 | 87 | 180 | 104 | 91 |
| 1σ[a] | 881 | 26 | 203 | 34 | 4 | 2 | 4 | 127 | 73 | 36 | 5 | 11 | 9 | 10 |
| Ni[b] | 31.0% | 16472 | 32.4% | 35.2% | 1718 | 1616 | 6666 | 32.4% | 32.6% | 33.5% | 324 | 1309 | 132 | <141 |
| 1σ |  | 2558 |  |  | 306 | 49 | 320 |  |  |  | 38 | 109 | 13 |  |
| Cu[b] | 11 | 37% | 22 | 15 | <6.7 | 3.5 | 1167 | 12337 | 2291 | 348 | 25 | 55 | 67 | 128 |
| 1σ | 3 |  | 2 | 1 |  | 1.3 | 168 | 900 | 252 | 26 | 3 | 7 | 8 | 18 |
| Zn | <8.9 | 859 | <2.8 | 2.3 | <14 | <6.7 | <3.5 | 151 | 54 | 5.3 | 4.2 | 11 | 33 | 29 |
| 1σ |  | 122 |  | 0.3 |  |  |  | 8 | 4 | 0.5 | 1.1 | 3 | 4 | 5 |
| Ga | <1.3 | 3.8 | <0.42 | <0.093 | <2.4 | <1.1 | <0.60 | 0.14 | <0.22 | <0.095 | <0.40 | <1.1 | 2.8 | 2.1 |
| 1σ |  | 1.3 |  |  |  |  |  | 0.05 |  |  |  |  | 0.4 | 0.6 |
| Ge | <6.7 | <13 | 3.2 | 2.7 | <15.1 | <6.7 | <3.4 | 3.0 | 2.1 | 2.7 | <2.7 | <7.5 | 1.6 | <7.4 |
| 1σ |  |  | 0.9 | 0.2 |  |  |  | 0.3 | 0.5 | 0.2 |  |  | 0.4 |  |
| As | 6.8 | <7.7 | 6.7 | 2.4 | <7.7 | <3.4 | <1.7 | 7.7 | 8.3 | 5.8 | 26 | <5.9 | 128 | <5.6 |
| 1σ | 1.9 |  | 0.5 | 0.1 |  |  |  | 0.3 | 0.3 | 0.1 | 2 |  | 27 |  |
| Se | 108 | 138 | 109 | 101 | 81 | 94 | 86 | 121 | 113 | 92 | 40 | <59 | 40 | <61 |
| 1σ | 24 | 25 | 6 | 2 | 33 | 12 | 7 | 4 | 4 | 1 | 8 |  | 4 |  |
| Ag | 3.0 | <3.0 | 3.1 | 3.3 | <2.0 | <0.95 | 1.0 | 4.3 | 5.3 | 3.4 | <0.44 | <1.4 | 0.50 | <1.3 |
| 1σ | 0.7 |  | 0.2 | 0.1 |  |  | 0.2 | 0.1 | 0.2 | 0.1 |  |  | 0.12 |  |
| Cd | <1.6 | 13 | <0.62 | <0.14 | <3.6 | <1.5 | <0.61 | 5.1 | 1.8 | <0.10 | <1.1 | <3.3 | 0.51 | <4.2 |
| 1σ |  | 4 |  |  |  |  |  | 0.2 | 0.2 |  |  |  | 0.18 |  |
| Sb | <0.8 | <3.6 | <0.26 | 0.088 | <2.5 | <1.0 | <0.43 | <0.090 | <0.14 | <0.047 | <0.69 | <1.7 | 0.41 | <1.5 |
| 1σ |  | 1 |  | 0.024 |  |  |  |  |  |  |  |  | 0.09 |  |
| Te | 11 | <10.1 | 4.1 | 17 | <8.1 | <5.6 | <2.4 | 14 | 20 | 7.6 | <2.5 | <7.3 | <0.90 | <7.4 |
| 1σ | 3 |  | 0.7 | 1 |  |  |  | 1 | 1 | 0.3 |  |  |  |  |
| Tl | <0.20 | <0.28 | <0.048 | 0.030 | <0.49 | <0.32 | <0.11 | 0.075 | 0.050 | 0.016 | 2.2 | 0.3 | 1.5 | 0.7 |
| 1σ |  |  |  | 0.008 |  |  |  | 0.012 | 0.013 | 0.004 | 0.2 | 0.1 | 0.2 | 0.1 |
| Pb | 1.7 | 3.0 | 3.5 | 0.63 | <1.2 | 1.7 | 6.3 | 6.2 | 7.4 | 1.4 | 0.14 | <0.33 | 0.96 | <0.29 |
| 1σ | 0.5 | 1.0 | 0.2 | 0.0 |  | 0.2 | 0.4 | 0.1 | 0.3 | 0.1 | 0.05 |  | 0.20 |  |
| Bi | 0.40 | 1.5 | 0.64 | 0.12 | 0.55 | 0.83 | 3.7 | 0.70 | 0.68 | 0.15 | <0.10 | <0.25 | <0.028 | <0.20 |
| 1σ | 0.10 | 0.4 | 0.22 | 0.01 | 0.20 | 0.12 | 0.1 | 0.02 | 0.04 | 0.01 |  |  |  |  |
| Frequency (Hz) | 36 | 20 | 33 | 42 | 33 | 42 | 36 | 42 | 36 | 36 | 20 | 20 | 20 | 20 |
| Beam size[c] (μm) | 30 | 10 (l) | 20 (l) | 340 (l) | 5 | 5 | 105 (l) | 190 (l) | 180(l) | 240 (l) | 40 | 20 | 50 | 20 |

|  | 19-11-T |  |  |  |  |  |  |  |  |  |  |  | 21-9-A |  |
|---|---|---|---|---|---|---|---|---|---|---|---|---|---|---|
|  | sa1c | sa2 | sa3 | m2sa1 | m2sa2 | m2sb1 | m2sb3 | m2sc | m2sd1 | m2sd2 | m2sg1 | m2sg2 | cb1 | cb2 |
| Mineral | Po | Po | Po | Po | Po | Po | Po | Po | Po | Po | Po | Po | Pn | Pn |
| Co | 117 | 80 | 128 | 107 | 93 | 66 | 34 | 111 | 66 | 65 | 53 | 45 | nd | nd |
| 1σ[a] | 13 | 7 | 36 | 3 | 3 | 5 | 3 | 3 | 7 | 9 | 4 | 3 |  |  |
| Ni[b] | <152 | 546 | <5038 | 81 | 95 | 129 | 70 | 97 | 135 | 274 | <45 | 119 | 30.2% | 29.7% |
| 1σ |  | 102 |  | 9 | 11 | 16 | 14 | 17 | 22 | 37 |  | 18 |  |  |
| Cu[b] | 405 | 473 | 1286 | 8.7 | 212 | 460 | 134 | 51 | 47 | 46 | 29 | 36 | 52 | 32 |
| 1σ | 31 | 56 | 313 | 2.6 | 20 | 61 | 12 | 8 | 5 | 5 | 8 | 10 | 11 | 6 |
| Zn | 41 | 87 | <382 | <6.2 | 34 | 95 | 19 | <11 | 15.3 | <7.4 | <11 | <11 | 29 | 29 |
| 1σ | 7 | 13 |  |  | 5 | 10 | 5 |  | 4.0 |  |  |  | 11 | 10 |
| Ga | <1.2 | 1.8 | <43 | <1.1 | 1.9 | <1.6 | 2.7 | <2.0 | <1.6 | <1.3 | <2.1 | <2.0 | <5.7 | <5.9 |
| 1σ |  | 0.7 |  |  | 0.5 |  | 0.8 |  |  |  |  |  |  |  |
| Ge | <7.9 | <12 | <270 | <7.1 | <7.4 | <10 | <13 | <12 | <9.6 | <7.7 | <13 | <12 | <35 | <35 |
| 1σ |  |  |  |  |  |  |  |  |  |  |  |  |  |  |
| As | 10 | 46 | <196 | <4.4 | 16 | 41 | 9.6 | <6.9 | <5.5 | <4.4 | <7.2 | <6.5 | <21 | 30 |
| 1σ | 3 | 6 |  |  | 3 | 4 | 3.4 |  |  |  |  |  |  | 8 |
| Se | <64 | 100 | <2184 | 40 | 52 | <53 | <69 | <66 | 57 | <43 | <70 | <63 | <267 | <261 |
| 1σ |  | 30 |  | 14 | 16 |  |  |  | 22 |  |  |  |  |  |
| Ag | <1.4 | <2.1 | <52 | <0.85 | <0.88 | <1.2 | <1.5 | <1.5 | <1.1 | <0.95 | <1.5 | <1.3 | <4.0 | <4.2 |
| 1σ |  |  |  |  |  |  |  |  |  |  |  |  |  |  |
| Cd | <3.8 | <5.2 | <138 | <1.7 | <1.9 | <2.2 | <3.8 | <2.2 | <2.6 | <2.9 | <3.0 | <3.5 | <11 | <10 |
| 1σ |  |  |  |  |  |  |  |  |  |  |  |  |  |  |
| Sb | <1.5 | 2.7 | <56 | <1.5 | <1.5 | 2.0 | <2.1 | <2.0 | <1.5 | <1.2 | <1.9 | <1.8 | <7.5 | <7.6 |
| 1σ |  | 0.8 |  |  |  | 0.6 |  |  |  |  |  |  |  |  |
| Te | <6.9 | <10 | <303 | <4.1 | <4.3 | <4.9 | <7.0 | <6.5 | <4.3 | <4.2 | <6.2 | <5.9 | <30 | <30 |
| 1σ |  |  |  |  |  |  |  |  |  |  |  |  |  |  |
| Tl | 1.2 | 2.6 | 8.0 | <0.16 | 1.8 | 6.9 | 1.7 | <0.26 | 1.5 | 0.24 | <0.26 | <0.28 | <1.3 | <1.3 |
| 1σ | 0.2 | 0.5 | 3.9 |  | 0.2 | 0.5 | 0.3 |  | 0.2 | 0.09 |  |  |  |  |
| Pb | <0.32 | <0.50 | 13 | <0.63 | <0.63 | <0.84 | <1.0 | <0.92 | <0.79 | <0.68 | <1.1 | <0.93 | 29 | 50 |
| 1σ |  |  | 7 |  |  |  |  |  |  |  |  |  | 5 | 7 |
| Bi | <0.21 | <0.27 | <7.8 | <0.21 | <0.20 | <0.26 | <0.29 | <0.27 | <0.21 | <0.15 | <0.26 | <0.26 | <1.3 | <1.2 |
| 1σ |  |  |  |  |  |  |  |  |  |  |  |  |  |  |
| Frequency (Hz) | 20 | 20 | 20 | 15 | 12 | 12 | 20 | 20 | 18 | 12 | 15 | 16 | 14 | 8 |
| Beam size[c] (μm) | 20 | 20 | 10 | 13 (r) | 10 | 10 | 5 | 10 | 10 | 10 | 5 | 5 | 5 | 5 |

|  | 21-9A |  |  |  |  | 21-9B |  |  |  |  | 21-9T |  |  |  |
|---|---|---|---|---|---|---|---|---|---|---|---|---|---|---|
|  | u1 | ckn | ckm | ckl | cji | cg1 | cg2 | st | sk1 | sk2 | sr | ss | ckp | cko |
| Mineral | Pn | Pn | Pn | Pn | Pn | Mi | Gs | Hz | Hz | Hz | Pn | Pn | Pn | Pn |
| Co | nd | nd | nd | nd | nd | nd | nd | nd | nd | nd | nd | nd | nd | nd |
| 1σ[a] |  |  |  |  |  |  |  |  |  |  |  |  |  |  |
| Ni[b] | 33.2% | 33.4% | 32.8% | 32.1% | 33.5% | 62.4% | 66.0% | 72.3% | 71.7% | 72.1% | 39.4% | 36.2% | 32.7% | 32.2% |
| 1σ |  |  |  |  |  |  |  |  |  |  |  |  |  |  |
| Cu[b] | 10 | <2.7 | 2.9 | 4.2 | 15 | 59 | 27 | <5.2 | 1.7 | 7.0 | 228 | 80 | 148 | 181 |
| 1σ | 2 |  | 0.5 | 0.7 | 3 | 6 | 2 |  | 0.4 | 1.9 | 17 | 19 | 61 | 62 |
| Zn | <10 | <5.2 | <2.6 | <5.3 | <15 | <12 | <6.5 | <11 | <2.2 | <12 | 8.6 | <8.1 | <170 | <22 |
| 1σ |  |  |  |  |  |  |  |  |  |  | 1.2 |  |  |  |
| Ga | <2.4 | <1.2 | <0.8 | <1.7 | <3.1 | <2.6 | <1.4 | <2.8 | <0.48 | <2.7 | <1.3 | <1.9 | <56 | <8.2 |
| 1σ |  |  |  |  |  |  |  |  |  |  |  |  |  |  |
| Ge | <20 | <11 | <6 | <13 | <18 | <16 | <7.8 | <25 | <2.7 | <15 | <10 | <16 | <47 | <64 |
| 1σ |  |  |  |  |  |  |  |  |  |  |  |  |  |  |
| As | 22 | 29 | 27 | 23 | 31 | 8294 | 1641 | 458 | 816 | 1219 | 45 | 48 | <227 | <30 |
| 1σ | 4 | 6 | 3 | 7 | 5 | 677 | 97 | 98 | 83 | 43 | 3 | 10 |  |  |
| Se | <165 | 130 | 158 | 157 | <157 | 215 | 354 | <191 | 125 | <137 | 130 | <121 | <3645 | <490 |
| 1σ |  | 30 | 20 | 46 |  | 48 | 29 |  | 19 |  | 17 |  |  |  |
| Ag | <3.0 | <1.4 | <0.8 | <1.8 | <2.2 | <1.5 | <0.82 | <3.0 | <0.35 | <1.8 | <1.3 | <2.0 | <59 | <7.5 |
| 1σ |  |  |  |  |  |  |  |  |  |  |  |  |  |  |
| Cd | <7.6 | <3.9 | <2.4 | <6.1 | <5.0 | <4.5 | <1.9 | <7.1 | <0.83 | <4.6 | <2.9 | <5.1 | <135 | <22 |
| 1σ |  |  |  |  |  |  |  |  |  |  |  |  |  |  |
| Sb | <4.6 | <2.1 | <1.2 | <2.7 | <3.1 | 48 | 6.0 | <5.1 | 2.2 | <2.5 | 4.2 | 12 | <86 | <12 |
| 1σ |  |  |  |  |  | 5 | 0.8 |  | 0.3 |  | 0.6 | 3 |  |  |
| Te | <21 | 21 | 17 | 12 | 26 | 102 | 100 | 34 | 133 | 107 | 31 | 13 | <319 | <45 |
| 1σ |  | 4 | 2 | 5 | 6 | 13 | 7 | 10 | 14 | 8 | 3 | 4 |  |  |
| Tl | <0.43 | <0.20 | <0.097 | <0.20 | <0.57 | <0.49 | <0.28 | <0.44 | <0.089 | <0.53 | 0.45 | <0.37 | <5.0 | <0.78 |
| 1σ |  |  |  |  |  |  |  |  |  |  | 0.05 |  |  |  |
| Pb | 7.9 | 3.1 | 0.8 | 5.1 | 16 | 26 | 13 | 1.8 | 0.68 | <0.61 | 9.1 | 5.3 | 22 | 23 |
| 1σ | 2.0 | 0.4 | 0.2 | 1.0 | 3 | 2 | 1 | 0.5 | 0.09 |  | 0.5 | 1.2 | 8 | 8 |
| Bi | <0.70 | <0.30 | <0.19 | <0.42 | <0.48 | 8.4 | 3.0 | 0.81 | <0.078 | <0.50 | <0.29 | <0.50 | <13 | <1.9 |
| 1σ |  |  |  |  |  | 0.7 | 0.2 | 0.27 |  |  |  |  |  |  |
| Frequency (Hz) | 50 | 50 | 50 | 50 | 10 | 10 | 17 | 50 | 42 | 10 | 10 | 50 | 50 | 50 |
| Beam size[c] (μm) | 5 | 5 | 5 | 5 | 5 | 5 | 5 | 5 | 5 | 5 | 30 | 5 | 5 | 5 |

| | 21-9T | | | 28-9A | |
|---|---|---|---|---|---|
| | cjg | cjh | cjj | ca1 | ca2 |
| Mineral | Pn | Pn | Pn | Pn | Pn |
| Co | nd | nd | nd | 8784 | 9555 |
| 1σ[a] | | | | 717 | 173 |
| Ni[b] | 40.1% | 34.8% | 33.6% | 239576 | 333664 |
| 1σ | | | | 18128 | 5886 |
| Cu[b] | 463 | 130 | 133 | 910 | 598 |
| 1σ | 87 | 8 | 26 | 109 | 57 |
| Zn | 31 | 512 | <74 | <201 | <100 |
| 1σ | 6 | 87 | | | |
| Ga | <0.99 | <5.5 | <16.4 | <18 | <8.7 |
| 1σ | | | | | |
| Ge | <5.5 | <31 | <92 | <76 | <38 |
| 1σ | | | | | |
| As | 1028 | 33 | <55 | 96 | 31 |
| 1σ | 103 | 7 | | 24 | 7 |
| Se | 250 | <274 | <835 | <699 | 407 |
| 1σ | 38 | | | | 138 |
| Ag | <0.70 | <3.9 | <12 | <20 | <10 |
| 1σ | | | | | |
| Cd | <1.7 | <9.6 | <31 | <25 | <11 |
| 1σ | | | | | |
| Sb | 3.2 | <5.4 | <16 | <15 | <7.3 |
| 1σ | 0.6 | | | | |
| Te | 139 | 49 | <82 | <80 | <38 |
| 1σ | 16 | 13 | | | |
| Tl | <0.18 | <0.94 | <2.9 | <4.0 | <2.2 |
| 1σ | | | | | |
| Pb | 29 | 26 | 50 | 21 | <4.9 |
| 1σ | 5 | 2 | 8 | 4 | |
| Bi | 0.80 | <0.96 | <2.8 | <2.7 | <1.5 |
| 1σ | 0.15 | | | | |
| Frequency (Hz) | 25 | 10 | 10 | 8 | 8 |
| Beam size[c] (μm) | 5 | 5 | 5 | 5 | 5 |

[a] 1σ: within-run error;

[b] Ni in pentlandite, and Cu in chalcopyrite were measured by the electron microprobe;

[c] when line (l) or raster (r.) were made, the length of the line/diameter of the raster is given instead the size of the beam size.

Sulfide abbreviations: Pn, pentlandite; Po, pyrrhotite; Ccp, chalcopyrite; Hz, heazlewoodite; Gs, godlevskite; Mi, millerite.

## B. *Chemical compositions of the Kane Megamullion serpentines*

**Table B.1.** Selected EPMA analyses of serpentines from the Kane Megamullion OCC

| Lithology (sample ID) | spinel harzburgite (14-44) | | | | | | | plagioclase harzburgite (19-11A) | | | | mantle-gabbro-contact (21-9T) | | | |
|---|---|---|---|---|---|---|---|---|---|---|---|---|---|---|---|
| Analysis code | ca5 | ca6 | ca10 | ca11 | ca12 | ca13 | ca14 | oaa1 | oaa2 | oaa3 | oab1 | ck1 | ck2 | ck3 | ck4 |
| *major elements [wt%]* | | | | | | | | | | | | | | | |
| $SiO_2$ | 42.0 | 42.3 | 38.5 | 42.2 | 40.4 | 41.7 | 39.9 | 39.4 | 39.9 | 40.3 | 36.7 | 42.1 | 42.3 | 42.9 | 41.7 |
| $Al_2O_3$ | 1.4 | 1.4 | 3.1 | 0.2 | 0.3 | 0.1 | 0.2 | 3.6 | 3.8 | 3.7 | 4.1 | 0.6 | 0.9 | 0.5 | 0.5 |
| CaO | 0.1 | 0.1 | 0.2 | 0.1 | 0.0 | 0.1 | 0.2 | 0.1 | 0.1 | 0.2 | 0.1 | 0.1 | 0.2 | 0.0 | 0.1 |
| $K_2O$ | 0.0 | 0.0 | 0.1 | 0.0 | 0.0 | 0.0 | 0.0 | 0.1 | 0.1 | 0.2 | 0.0 | 0.0 | 0.0 | 0.0 | 0.0 |
| $TiO_2$ | 0.0 | 0.0 | 0.1 | 0.0 | 0.0 | 0.0 | 0.0 | 0.0 | 0.0 | 0.0 | 0.0 | 0.0 | 0.0 | 0.0 | 0.0 |
| FeO[a] | 3.9 | 4.0 | 6.6 | 6.0 | 4.4 | 8.4 | 8.3 | 7.1 | 7.1 | 7.5 | 7.1 | 7.6 | 7.7 | 3.7 | 2.4 |
| MnO | 0.0 | 0.0 | 0.0 | 0.0 | 0.0 | 0.2 | 0.3 | 0.3 | 0.2 | 0.2 | 0.0 | 0.0 | 0.0 | 0.5 | 2.4 |
| $Cr_2O_3$ | 0.0 | 0.0 | 0.7 | 0.0 | 0.0 | 0.0 | 0.0 | 1.2 | 1.0 | 1.2 | 1.1 | 0.0 | 0.0 | 0.0 | 0.0 |
| $Na_2O$ | 0.1 | 0.1 | 0.1 | 0.1 | 0.0 | 0.0 | 0.1 | 0.1 | 0.1 | 0.1 | 0.1 | 0.1 | 0.0 | 0.0 | 0.0 |
| MgO | 36.7 | 36.5 | 31.7 | 35.0 | 36.9 | 35.1 | 33.1 | 25.5 | 32.1 | 29.0 | 28.8 | 35.8 | 33.1 | 38.8 | 38.9 |
| NiO | 0.0 | 0.0 | 0.0 | 0.3 | 0.3 | 0.4 | 0.4 | 0.3 | 0.2 | 0.2 | 0.4 | 0.4 | 0.4 | 0.0 | 0.4 |
| TOTAL | 84.2 | 84.4 | 81.1 | 83.9 | 82.3 | 86.0 | 82.4 | 77.6 | 84.6 | 82.5 | 78.5 | 86.7 | 84.6 | 86.4 | 86.4 |
| *trace elements [ppm]* | | | | | | | | | | | | | | | |
| Cu (63)[b] | 11 | 7.0 | 5.9 | 10 | 8.9 | 8.5 | 8.6 | 117 | 69 | 39 | 91 | 306 | 281 | 931 | 813 |
| Zn (66) | 28 | 33 | 74 | 28 | 28 | 27 | 26 | 55 | 47 | 29 | 69 | 168 | 139 | 287 | 175 |
| Ga (69) | 2.2 | 2.1 | 2.7 | 1.8 | 1.6 | 1.8 | 1.7 | 4.8 | 4.5 | 4.2 | 4.6 | 56 | 65 | 276 | 333 |
| Ge (74) | 0.48 | 0.53 | 0.84 | 0.93 | 1.0 | <0.99 | <0.99 | 1.9 | <1.6 | <1.7 | <1.7 | <61 | <13.2 | <247 | <315 |
| As (75) | 2.0 | 2.9 | 1.5 | 12 | 11 | 17 | 20 | 580 | 601 | 568 | 551 | <28 | 14 | <111 | <145 |
| Se (77) | 2.8 | 2.7 | 2.9 | 2.7 | 3.0 | <9.2 | <8.8 | <21 | <20 | <21 | <21 | <463 | <101 | <1866 | <2313 |
| Ag (107) | 0.057 | 0.027 | 0.053 | 0.097 | 0.090 | <0.068 | <0.052 | <0.35 | <0.31 | <0.34 | <0.33 | <8.7 | <1.5 | <33 | <44 |
| Cd (111) | 0.044 | 0.031 | 0.042 | 0.038 | 0.038 | <0.20 | <0.21 | <1.0 | <0.97 | <0.95 | <1.0 | <27 | <3.2 | <91 | <138 |
| Sb (121) | 0.092 | 0.087 | 0.11 | 0.35 | 0.33 | 0.43 | 0.88 | 0.49 | <0.35 | <0.34 | 0.38 | <12 | <2.1 | <47 | <65 |
| Te (125) | 0.082 | 0.080 | 0.093 | 0.07 | 0.15 | <0.55 | <0.63 | <1.9 | <1.6 | <1.8 | <1.9 | <53 | <8.2 | <212 | <310 |
| Tl (205) | 0.063 | 0.056 | 0.12 | 0.083 | 0.086 | 0.085 | 0.079 | 0.11 | 0.12 | 0.10 | 0.29 | 1.2 | 0.61 | 17 | 14 |
| Pb (208) | 0.66 | 0.56 | 0.53 | 0.62 | 0.58 | 0.54 | 0.56 | 2.6 | 2.6 | 2.4 | 2.2 | 20 | 15 | 137 | 166 |
| Bi (209) | 0.39 | 0.23 | 0.26 | 0.34 | 0.34 | 0.31 | 0.26 | <0.051 | <0.045 | <0.042 | <0.042 | <2.1 | <0.32 | <8.3 | <11 |

[a] All iron calculated as FeO
[b] isotope mass

## *C. Chalcophile element contents of the Kane Megamullion hydrothermal products*

**Table C.1.** Chalcophile element contents of the Kane Megamullion hydrothermal products determined by INAA and ICPMS.

| Label | Cu | As | Zn | Ga | Pb | Se | Sb | Tl | Ni | Ag | Bi | Cd |
|---|---|---|---|---|---|---|---|---|---|---|---|---|
| 112-54 | 228 | 237 | 116 | 1.5 | 1.7 | 2.0 | 9.6 | 10.1 | 774 | <0.05 | 0.02 | 0.9 |
| 112-75 | 5.3 | 14.3 | 6.6 | <1.0 | 0.5 | 0.7 | 2.1 | 0.23 | 72.9 | <0.05 | <0.02 | 0.2 |
| 112-95 | 717 | 332 | 536 | <1.0 | 795 | 6.7 | 49.9 | 103 | 1730 | 3.22 | 9.06 | 3.2 |
| 112-96 | 242 | 98.9 | 76.4 | 2.3 | 16.9 | 1.1 | 8.0 | 2.3 | 221 | 0.38 | 0.25 | 0.3 |
| 112-97 | 3500 | 89.7 | 1150 | 16.4 | 32.1 | 3.0 | 22.9 | 211 | 3630 | 0.32 | 0.61 | 4.9 |
| 112-98 | 84.5 | 14.0 | 31.5 | 1.1 | 8.1 | 1.0 | 2.6 | 2.6 | 296 | 0.09 | 0.19 | 0.4 |
| 112-104 | 1790 | 21.8 | 617 | 5.2 | 27.8 | 0.8 | 98.6 | 152 | 1650 | 0.09 | 0.22 | 21.1 |
| 116-30-(1) | 1840 | 14.4 | 44.1 | 0.9 | 4.2 | 0.1 | 6.4 | 8.1 | 2030 | <0.05 | 0.05 | 0.7 |
| 116-30-(3) | 2280 | 159 | 139 | 2.7 | 9.7 | <0.1 | 22.1 | 45.7 | 6040 | <0.05 | 0.08 | 1.7 |
| 116-46 | 489 | 570 | 772 | 2.5 | 1.4 | 0.6 | 50.8 | 29.7 | 884 | 0.05 | 0.20 | 5.7 |

## D. *Major element compositions of the Kane Megamullion sulfides*

**Table D.1.** Major element compositions (wt%) of the Kane Megamullion sulfides determined by an electron probe microanalyzer.

| Sample No. | | Mineral[a] | Fe | Co | Ni | Cu | S | Total | Me/S[e] | Ni/(Ni+Fe)[e] | Cu/(Cu+Fe)[e] |
|---|---|---|---|---|---|---|---|---|---|---|---|
| 5-1 | sa1 | Pn | 32.5 | n/a[d] | 33.8 | 0.0 | 32.9 | 99.2 | 1.13 | 0.50 | |
| spinel harzburgite[b] | sa2 | Pn | 32.0 | n/a | 33.9 | 0.0 | 32.6 | 98.5 | 1.13 | 0.50 | |
| 5-31B | cb9 | Pn | 36.8 | 0.4 | 30.6 | 0.0 | 31.5 | 99.3 | 1.21 | 0.44 | |
| olivine websterite | cb10 | Pn | 33.4 | 0.4 | 32.2 | 0.0 | 31.4 | 97.5 | 1.18 | 0.48 | |
| | cb11 | Ccp | 31.8 | 0.0 | 0.2 | 36.6 | 32.9 | 101.5 | 1.12 | | 0.50 |
| | cb12 | Ccp | 31.4 | 0.0 | 0.2 | 37.0 | 32.7 | 101.4 | 1.13 | | 0.51 |
| | cb13 | Pn | 33.8 | 0.4 | 31.6 | 0.0 | 30.0 | 95.8 | 1.23 | 0.47 | |
| | cb14 | Pn | 33.2 | 0.8 | 32.1 | 0.0 | 31.2 | 97.3 | 1.19 | 0.48 | |
| | cb15 | Pn | 33.3 | 0.8 | 32.4 | 0.0 | 30.6 | 97.1 | 1.22 | 0.48 | |
| | cb16 | Ccp | 31.3 | 0.0 | 0.3 | 36.1 | 32.2 | 99.9 | 1.13 | | 0.50 |
| | cb17 | Pn | 31.5 | 0.4 | 34.6 | 0.0 | 30.3 | 96.9 | 1.23 | 0.51 | |
| | cb18 | Pn | 31.4 | 0.4 | 34.7 | 0.0 | 30.6 | 97.1 | 1.22 | 0.51 | |
| | cb19 | Pn | 32.5 | 0.4 | 34.0 | 0.0 | 30.1 | 97.0 | 1.24 | 0.50 | |
| | cb20 | Pn | 32.6 | 0.4 | 33.3 | 0.0 | 29.9 | 96.1 | 1.24 | 0.49 | |
| | cb21 | Pn | 36.2 | 0.6 | 30.5 | 0.0 | 29.8 | 97.1 | 1.27 | 0.44 | |
| | cb22 | Pn | 35.2 | 0.5 | 31.1 | 0.0 | 30.1 | 97.0 | 1.24 | 0.46 | |
| | cb23 | Pn | 35.5 | 0.5 | 31.2 | 0.0 | 30.1 | 97.3 | 1.25 | 0.46 | |
| | cb24 | Pn | 36.1 | 0.6 | 30.2 | 0.0 | 30.1 | 97.0 | 1.25 | 0.44 | |
| | cb25 | Pn | 36.4 | 0.6 | 29.2 | 0.0 | 30.1 | 96.2 | 1.23 | 0.43 | |
| | cb26 | Pn | 32.1 | 0.7 | 33.7 | 0.0 | 30.8 | 97.3 | 1.21 | 0.50 | |
| | ca17 | Pn | 33.4 | 0.4 | 32.7 | 0.0 | 30.5 | 97.1 | 1.22 | 0.48 | |
| | ca18 | Pn | 33.3 | 0.5 | 32.2 | 0.0 | 30.9 | 96.8 | 1.20 | 0.48 | |
| | ca19 | Pn | 32.6 | 0.5 | 31.1 | 0.0 | 30.3 | 94.5 | 1.19 | 0.48 | |
| | ca20 | Pn | 35.6 | 0.5 | 30.3 | 0.0 | 30.2 | 96.5 | 1.24 | 0.45 | |
| | ca21 | Pn | 35.4 | 0.5 | 30.6 | 0.0 | 30.0 | 96.5 | 1.24 | 0.45 | |
| | ca22 | Pn | 32.4 | 0.4 | 34.1 | 0.0 | 29.5 | 96.4 | 1.27 | 0.50 | |
| | ca23 | Pn | 31.9 | 0.4 | 34.8 | 0.0 | 29.7 | 96.8 | 1.26 | 0.51 | |
| | ca24 | Pn | 32.0 | 0.4 | 33.1 | 0.0 | 29.9 | 95.3 | 1.23 | 0.50 | |
| | ca25 | Ccp | 30.9 | 0.0 | 0.3 | 34.9 | 32.0 | 98.1 | 1.11 | | 0.50 |

| Sample No. | Mineral[a] | Fe | Co | Ni | Cu | S | Total | Me/S[e] | Ni/(Ni+Fe)[e] | Cu/(Cu+Fe)[e] |
|---|---|---|---|---|---|---|---|---|---|---|
| ca26 | Pn | 33.2 | 0.4 | 32.2 | 0.0 | 29.8 | 95.6 | 1.24 | 0.48 | |
| ca27 | Pn | 32.8 | 0.4 | 31.6 | 0.0 | 29.8 | 94.5 | 1.22 | 0.48 | |
| ca28 | Pn | 32.5 | 0.6 | 32.0 | 0.0 | 29.1 | 94.2 | 1.26 | 0.48 | |
| ca30 | Pn | 34.1 | 0.7 | 31.0 | 0.0 | 30.1 | 95.9 | 1.23 | 0.46 | |
| ca31 | Ccp | 29.9 | 0.0 | 3.9 | 30.6 | 34.5 | 99.0 | 1.01 | | 0.47 |
| ca32 | Pn | 33.1 | 0.5 | 32.3 | 0.0 | 29.7 | 95.7 | 1.24 | 0.48 | |
| ca33 | Pn | 34.4 | 0.3 | 32.0 | 0.0 | 29.6 | 96.3 | 1.26 | 0.47 | |
| ca34 | Pn | 34.5 | 0.3 | 31.8 | 0.0 | 30.1 | 96.6 | 1.24 | 0.47 | |
| ca35 | Pn | 32.2 | 0.4 | 33.6 | 0.0 | 30.1 | 96.3 | 1.23 | 0.50 | |
| ca36 | Pn | 31.9 | 0.3 | 33.2 | 0.0 | 29.9 | 95.4 | 1.23 | 0.50 | |
| ca37 | Pn | 33.5 | 0.4 | 32.0 | 0.0 | 32.4 | 98.2 | 1.14 | 0.48 | |
| cc11 | Pn | 35.3 | 1.0 | 30.4 | 0.0 | 29.8 | 96.6 | 1.26 | 0.45 | |
| cc12 | Ccp | 29.8 | 0.0 | 0.6 | 35.5 | 34.0 | 100.0 | 1.04 | | 0.51 |
| cc13 | Pn | 33.9 | 1.0 | 30.7 | 0.0 | 32.2 | 97.8 | 1.14 | 0.46 | |
| cc14 | Pn | 33.8 | 0.9 | 30.6 | 0.0 | 32.3 | 97.7 | 1.13 | 0.46 | |
| cc15 | Pn | 34.7 | 0.8 | 30.1 | 0.0 | 29.9 | 95.6 | 1.23 | 0.45 | |
| cc16 | Ccp | 29.6 | 0.0 | 1.2 | 33.4 | 35.0 | 99.2 | 0.99 | | 0.50 |
| cc17 | Pn | 33.8 | 1.0 | 30.6 | 0.0 | 31.7 | 97.2 | 1.16 | 0.46 | |
| cc18 | Pn | 31.8 | 1.0 | 33.9 | 0.0 | 32.4 | 99.0 | 1.15 | 0.50 | |
| cc19 | Pn | 32.1 | 0.5 | 33.7 | 0.0 | 32.8 | 99.2 | 1.13 | 0.50 | |
| cc20 | Pn | 32.6 | 0.6 | 33.1 | 0.0 | 32.8 | 99.2 | 1.13 | 0.49 | |
| cc21 | Pn | 33.3 | 0.6 | 31.6 | 0.0 | 29.5 | 95.0 | 1.25 | 0.47 | |
| cc22 | Pn | 33.5 | 0.7 | 31.8 | 0.0 | 30.2 | 96.1 | 1.22 | 0.47 | |
| cc23 | Pn | 31.7 | 0.6 | 32.2 | 0.0 | 31.0 | 95.4 | 1.17 | 0.49 | |
| cc24 | Pn | 31.3 | 0.8 | 34.2 | 0.0 | 32.7 | 98.9 | 1.14 | 0.51 | |
| oa8 | Ccp | 30.0 | 0.0 | 0.2 | 36.2 | 34.8 | 101.2 | 1.02 | | 0.51 |
| oa9 | Po | 60.0 | 0.0 | 0.0 | 0.0 | 39.3 | 99.3 | 0.88 | | |
| oa10 | Po | 61.0 | 0.0 | 0.3 | 0.0 | 38.9 | 100.2 | 0.90 | | |
| oa11 | Po | 60.3 | 0.0 | 0.0 | 0.0 | 38.2 | 98.6 | 0.91 | | |
| oa12 | Pn | 36.0 | 0.3 | 30.3 | 0.0 | 30.1 | 96.8 | 1.24 | 0.44 | |
| oa13 | Pn | 34.7 | 0.4 | 31.9 | 0.0 | 32.6 | 99.6 | 1.15 | 0.47 | |
| oa14 | Pn | 33.8 | 0.4 | 30.3 | 0.0 | 32.3 | 96.8 | 1.12 | 0.46 | |
| oa15 | Pn | 33.4 | 0.3 | 32.2 | 0.0 | 32.5 | 98.4 | 1.14 | 0.48 | |
| oa16 | Pn | 33.0 | 0.4 | 32.6 | 0.0 | 32.8 | 98.8 | 1.13 | 0.48 | |
| oa17 | Po | 63.2 | 0.0 | 0.2 | 0.0 | 36.3 | 99.7 | 1.00 | | |

| Sample No. | Mineral[a] | Fe | Co | Ni | Cu | S | Total | Me/S[e] | Ni/(Ni+Fe)[e] | Cu/(Cu+Fe)[e] |
|---|---|---|---|---|---|---|---|---|---|---|
| oa18 | Po | 62.7 | 0.0 | 0.2 | 0.0 | 36.2 | 99.1 | 1.00 | | |
| oa19 | Pn | 34.6 | 0.3 | 32.2 | 0.0 | 30.6 | 97.8 | 1.23 | 0.47 | |
| oa20 | Pn | 34.4 | 0.5 | 31.7 | 0.0 | 30.4 | 97.0 | 1.23 | 0.47 | |
| oa21 | Pn | 35.2 | 0.4 | 31.2 | 0.0 | 30.0 | 96.8 | 1.25 | 0.46 | |
| oa22 | Ccp | 31.7 | 0.0 | 0.2 | 35.8 | 31.9 | 99.6 | 1.14 | | 0.50 |
| oa23 | Po | 62.5 | 0.0 | 0.3 | 0.8 | 35.9 | 99.4 | 1.02 | | |
| oa24 | Pn | 37.3 | 0.4 | 28.3 | 0.0 | 30.4 | 96.4 | 1.22 | 0.42 | |
| oa25 | Po | 62.1 | 0.0 | 0.6 | 0.0 | 35.2 | 97.8 | 1.02 | | |
| oa26 | Pn | 36.8 | 0.3 | 30.9 | 0.0 | 30.5 | 98.6 | 1.25 | 0.44 | |
| oa27 | Po | 62.6 | 0.0 | 0.3 | 0.0 | 35.9 | 98.8 | 1.01 | | |
| oa28 | Po | 63.3 | 0.0 | 0.3 | 0.0 | 35.8 | 99.3 | 1.02 | | |
| oa29 | Po | 62.5 | 0.0 | 0.4 | 0.0 | 36.0 | 99.0 | 1.00 | | |
| oa30 | Pn | 36.5 | 0.3 | 30.2 | 0.0 | 30.3 | 97.4 | 1.24 | 0.44 | |
| oa31 | Pn | 36.5 | 0.4 | 30.6 | 0.6 | 29.9 | 97.9 | 1.28 | 0.44 | |
| oa33 | Pn | 29.3 | 0.4 | 35.3 | 0.0 | 32.8 | 97.8 | 1.11 | 0.53 | |
| oa34 | Ccp | 29.2 | 0.0 | 2.9 | 33.0 | 35.2 | 100.2 | 0.99 | | 0.50 |
| oa35 | Pn | 34.7 | 0.3 | 31.3 | 0.0 | 30.0 | 96.4 | 1.24 | 0.46 | |
| oa36 | Pn | 35.0 | 0.5 | 32.0 | 0.0 | 30.1 | 97.6 | 1.26 | 0.47 | |
| oa37 | Pn | 33.5 | 0.4 | 33.0 | 0.0 | 32.3 | 99.2 | 1.16 | 0.48 | |
| ob12 | Pn | 34.5 | 0.5 | 31.0 | 0.0 | 32.3 | 98.2 | 1.15 | 0.46 | |
| ob13 | Pn | 34.4 | 0.5 | 30.9 | 0.0 | 32.8 | 98.6 | 1.12 | 0.46 | |
| ob14 | Pn | 32.5 | 0.6 | 33.5 | 0.0 | 32.8 | 99.4 | 1.14 | 0.49 | |
| ob15 | Pn | 32.6 | 0.5 | 32.9 | 0.0 | 32.4 | 98.5 | 1.14 | 0.49 | |
| ob16 | Pn | 32.8 | 0.5 | 32.1 | 0.0 | 32.2 | 97.6 | 1.14 | 0.48 | |
| ob17 | Pn | 33.4 | 0.3 | 31.6 | 0.0 | 32.8 | 98.1 | 1.12 | 0.47 | |
| ob18 | Pn | 32.5 | 0.4 | 32.2 | 0.0 | 32.9 | 98.0 | 1.11 | 0.49 | |
| ob19 | Ccp | 29.6 | 0.0 | 0.2 | 36.0 | 34.6 | 100.6 | 1.02 | | 0.52 |
| ob20 | Pn | 34.1 | 0.4 | 31.6 | 0.0 | 32.7 | 98.9 | 1.13 | 0.47 | |
| ob23 | Pn | 31.8 | 0.3 | 33.5 | 0.0 | 32.4 | 98.0 | 1.13 | 0.50 | |
| oc15 | Pn | 30.0 | 0.7 | 35.2 | 0.0 | 32.3 | 98.2 | 1.14 | 0.53 | |
| sa1 | Ccp | 30.4 | 0.0 | 0.3 | 33.2 | 33.6 | 97.5 | 1.02 | | 0.49 |
| sa3 | Pn | 33.0 | 0.5 | 33.1 | 0.0 | 33.5 | 100.1 | 1.12 | 0.49 | |
| sa4 | Pn | 33.1 | 0.5 | 32.3 | 0.0 | 33.5 | 99.4 | 1.10 | 0.48 | |
| sa5 | Pn | 33.6 | 0.6 | 32.5 | 0.0 | 33.9 | 100.6 | 1.10 | 0.48 | |
| sa6 | Pn | 33.9 | 0.5 | 32.7 | 0.0 | 33.4 | 100.5 | 1.13 | 0.48 | |

| Sample No. | Mineral[a] | Fe | Co | Ni | Cu | S | Total | Me/S[e] | Ni/(Ni+Fe)[e] | Cu/(Cu+Fe)[e] |
|---|---|---|---|---|---|---|---|---|---|---|
| sa7 | Pn | 36.2 | 0.6 | 30.5 | 0.0 | 33.4 | 100.7 | 1.13 | 0.44 | |
| sa8 | Pn | 36.1 | 0.6 | 30.1 | 0.0 | 33.8 | 100.5 | 1.11 | 0.44 | |
| sa9 | Pn(+Ccp) | 31.5 | 0.3 | 21.1 | 13.7 | 34.3 | 100.9 | 1.07 | | |
| sa10 | Pn(+Ccp) | 35.3 | 0.5 | 29.2 | 1.6 | 34.0 | 100.5 | 1.10 | | |
| sa11 | Ccp | 30.5 | 0.0 | 0.4 | 35.1 | 35.5 | 101.5 | 1.00 | | 0.50 |
| sa12 | Pn | 36.1 | 0.5 | 30.4 | 0.0 | 33.5 | 100.5 | 1.12 | 0.44 | |
| sa14 | Pn | 33.0 | 0.5 | 33.1 | 0.0 | 33.3 | 99.9 | 1.12 | 0.49 | |
| sa16 | Pn | 33.1 | 0.6 | 31.9 | 0.0 | 33.1 | 98.7 | 1.11 | 0.48 | |
| sa17 | Ccp(+Pn) | 29.9 | 0.0 | 1.7 | 34.3 | 35.2 | 101.2 | 1.01 | | |
| sa18 | Ccp(+Pn) | 30.7 | 0.0 | 1.2 | 35.4 | 34.5 | 101.9 | 1.05 | | |
| sa20 | Pn | 32.8 | 0.6 | 33.5 | 0.0 | 33.6 | 100.5 | 1.11 | 0.49 | |
| sa21 | Pn | 33.0 | 0.6 | 32.6 | 0.0 | 32.7 | 98.8 | 1.13 | 0.48 | |
| sa22 | Pn | 32.9 | 0.5 | 33.6 | 0.0 | 33.0 | 99.9 | 1.14 | 0.49 | |
| sb1 | Pn | 34.2 | 0.4 | 31.6 | 0.0 | 32.0 | 98.2 | 1.16 | 0.47 | |
| sb2 | Pn | 33.8 | 0.5 | 32.1 | 0.0 | 32.2 | 98.6 | 1.15 | 0.47 | |
| sb3 | Pn | 34.8 | 0.6 | 31.9 | 0.0 | 33.0 | 100.2 | 1.14 | 0.47 | |
| sb4 | Ccp | 30.6 | 0.0 | 0.6 | 34.8 | 34.3 | 100.3 | 1.03 | | 0.50 |
| sb5 | Pn | 34.4 | 0.6 | 30.7 | 0.0 | 33.0 | 98.7 | 1.12 | 0.46 | |
| sb6 | Pn | 33.7 | 0.5 | 30.9 | 0.0 | 31.9 | 97.1 | 1.14 | 0.47 | |
| sb7 | Pn | 35.4 | 0.5 | 30.0 | 0.0 | 33.3 | 99.2 | 1.11 | 0.45 | |
| sb8 | Pn | 35.5 | 0.5 | 31.2 | 0.0 | 32.7 | 100.0 | 1.15 | 0.46 | |
| sb9 | Pn | 35.1 | 0.5 | 31.0 | 0.0 | 32.6 | 99.2 | 1.14 | 0.46 | |
| sc1 | Ccp | 30.4 | 0.0 | 0.7 | 37.0 | 34.6 | 102.7 | 1.05 | | 0.52 |
| sc2 | Pn | 32.2 | 0.5 | 31.0 | 0.0 | 32.2 | 95.8 | 1.11 | 0.48 | |
| sc3 | Pn | 33.8 | 0.5 | 33.3 | 0.0 | 33.3 | 100.9 | 1.14 | 0.48 | |
| sc4 | Pn | 33.2 | 0.5 | 32.0 | 0.0 | 33.3 | 99.0 | 1.11 | 0.48 | |
| sc5 | Viol | 16.0 | 0.5 | 37.6 | 0.0 | 40.2 | 90.0 | 0.75 | 0.69 | |
| sc6 | Viol | 18.0 | 0.5 | 38.5 | 0.0 | 43.2 | 95.5 | 0.73 | 0.67 | |
| sc7 | Pn | 32.2 | 0.6 | 33.1 | 0.0 | 33.1 | 99.0 | 1.11 | 0.49 | |
| sc15 | Viol | 17.7 | 0.6 | 36.9 | 0.0 | 42.3 | 93.0 | 0.73 | 0.66 | |
| sd5 | Ccp(+Pn) | 30.1 | 0.0 | 3.9 | 28.7 | 33.7 | 96.5 | 1.01 | | |
| sd6 | Pn(+Ccp) | 33.8 | 0.4 | 30.3 | 0.9 | 31.7 | 97.1 | 1.16 | | |
| sd7 | Ccp(+Pn) | 30.0 | 0.0 | 0.4 | 36.2 | 34.3 | 100.8 | 1.04 | | |
| se1 | Pn(+Ccp) | 31.4 | 0.3 | 33.3 | 1.6 | 33.1 | 99.7 | 1.12 | | |
| se2 | Pn | 31.1 | 0.4 | 35.3 | 0.0 | 33.0 | 99.8 | 1.13 | 0.52 | |

| Sample No. | Mineral[a] | Fe | Co | Ni | Cu | S | Total | Me/S[e] | Ni/(Ni+Fe)[e] | Cu/(Cu+Fe)[e] |
|---|---|---|---|---|---|---|---|---|---|---|
| se3 | Pn | 31.0 | 0.2 | 34.2 | 0.0 | 32.4 | 97.8 | 1.13 | 0.51 | |
| se4 | Pn | 32.1 | 0.2 | 34.0 | 0.0 | 32.6 | 99.0 | 1.14 | 0.50 | |
| sf1 | Pn | 34.0 | 0.9 | 31.3 | 0.0 | 30.6 | 96.6 | 1.21 | 0.47 | |
| sf2 | Ccp | 29.9 | 0.0 | 0.5 | 35.1 | 32.0 | 97.5 | 1.10 | | 0.51 |
| sf3 | Ccp | 30.4 | 0.0 | 0.3 | 35.4 | 32.5 | 98.6 | 1.09 | | 0.51 |
| sf4 | Pn | 36.9 | 0.8 | 28.7 | 0.0 | 31.1 | 97.4 | 1.20 | 0.43 | |
| sf5 | Pn | 32.7 | 0.7 | 33.0 | 0.0 | 29.9 | 96.3 | 1.24 | 0.49 | |
| sg1 | Pn | 34.7 | 0.5 | 32.0 | 0.0 | 30.8 | 97.9 | 1.22 | 0.47 | |
| sg2 | Pn | 32.7 | 0.6 | 33.1 | 0.0 | 30.3 | 96.6 | 1.23 | 0.49 | |
| sg3 | Pn | 30.4 | 0.0 | 0.4 | 34.1 | 32.9 | 97.8 | 1.06 | 0.01 | |
| sg4 | Pn | 32.8 | 0.4 | 32.9 | 0.0 | 30.3 | 96.4 | 1.22 | 0.49 | |
| sh1 | Pn | 34.4 | 0.4 | 31.2 | 0.0 | 29.8 | 95.8 | 1.24 | 0.46 | |
| sh2 | Ccp | 30.5 | 0.0 | 0.5 | 36.2 | 32.0 | 99.2 | 1.13 | | 0.51 |
| sh3 | Pn | 34.9 | 0.4 | 31.5 | 0.0 | 29.9 | 96.6 | 1.25 | 0.46 | |
| sh4 | Ccp | 30.5 | 0.0 | 0.5 | 34.9 | 32.1 | 98.0 | 1.10 | | 0.50 |
| sh5 | Po | 60.2 | 0.0 | 0.3 | 0.0 | 35.6 | 96.1 | 0.98 | | |
| sh6 | Po | 59.1 | 0.0 | 0.4 | 0.0 | 35.6 | 95.1 | 0.96 | | |
| sh7 | Po | 60.3 | 0.0 | 0.3 | 0.0 | 36.0 | 96.6 | 0.97 | | |
| sh8 | Pn | 34.2 | 0.2 | 30.8 | 0.0 | 30.1 | 95.3 | 1.22 | 0.46 | |
| si1 | Pn | 35.1 | 0.6 | 30.6 | 0.0 | 30.4 | 96.6 | 1.22 | 0.45 | |
| si2 | Pn | 34.0 | 0.6 | 31.0 | 0.0 | 30.2 | 95.8 | 1.22 | 0.46 | |
| si3 | Pn | 34.7 | 0.5 | 31.0 | 0.0 | 30.8 | 97.0 | 1.20 | 0.46 | |
| si4 | Ccp | 29.4 | 0.0 | 0.2 | 34.5 | 31.7 | 95.8 | 1.09 | | 0.51 |
| sj1 | Ccp | 30.3 | 0.0 | 0.2 | 35.4 | 31.5 | 97.4 | 1.12 | | 0.51 |
| sj2 | Pn | 58.8 | 0.0 | 0.3 | 0.0 | 36.7 | 95.9 | 0.93 | 0.01 | |
| sj3 | Pn | 32.3 | 0.5 | 31.9 | 0.0 | 30.2 | 94.9 | 1.20 | 0.48 | |
| sj4 | Pn | 35.6 | 0.5 | 29.3 | 0.0 | 30.0 | 95.3 | 1.23 | 0.44 | |
| sj5 | Ccp | 29.9 | 0.0 | 0.0 | 35.4 | 31.6 | 96.9 | 1.11 | | 0.51 |
| ga6 | Pn | 31.0 | 0.4 | 32.9 | 0.0 | 30.1 | 94.3 | 1.20 | 0.50 | |
| ga7 | Ccp | 30.0 | 0.0 | 1.9 | 35.9 | 31.0 | 98.7 | 1.17 | | 0.51 |
| ga8 | Pn | 33.1 | 0.6 | 32.5 | 0.0 | 29.0 | 95.2 | 1.28 | 0.48 | |
| ga9 | Ccp | 29.5 | 0.0 | 0.0 | 34.6 | 31.6 | 95.7 | 1.09 | | 0.51 |
| gc1 | Pn | 32.0 | 0.3 | 32.6 | 0.0 | 29.3 | 94.2 | 1.24 | 0.49 | |
| gc2 | Pn | 32.2 | 0.4 | 33.1 | 0.0 | 29.3 | 95.0 | 1.26 | 0.49 | |
| wa9 | Pn | 33.6 | 0.4 | 31.6 | 0.0 | 29.2 | 94.9 | 1.26 | 0.47 | |

| Sample No. |  | Mineral[a] | Fe | Co | Ni | Cu | S | Total | Me/S[e] | Ni/(Ni+Fe)[e] | Cu/(Cu+Fe)[e] |
|---|---|---|---|---|---|---|---|---|---|---|---|
|  | wa10 | Pn | 33.0 | 0.5 | 31.8 | 0.0 | 29.6 | 94.9 | 1.24 | 0.48 |  |
|  | yb10 | Ccp | 29.1 | 0.0 | 0.8 | 35.4 | 30.6 | 96.0 | 1.14 |  | 0.52 |
|  | yb11 | Ccp | 29.7 | 0.0 | 0.7 | 34.9 | 30.4 | 95.6 | 1.15 |  | 0.51 |
|  | yb14 | Pn | 32.7 | 0.5 | 31.9 | 0.0 | 29.3 | 94.5 | 1.25 | 0.48 |  |
|  | xa8 | Pn | 32.8 | 0.0 | 33.3 | 0.0 | 33.4 | 99.5 | 1.11 | 0.49 |  |
|  | xa15 | Pn | 32.3 | 0.4 | 31.8 | 0.0 | 29.3 | 93.8 | 1.23 | 0.48 |  |
|  | xb10 | Pn | 32.5 | 1.0 | 31.3 | 0.0 | 30.4 | 95.2 | 1.19 | 0.48 |  |
|  | xb11 | Ccp | 30.0 | 0.0 | 0.0 | 35.2 | 32.4 | 97.7 | 1.08 |  | 0.51 |
|  | xb12 | Ccp | 29.2 | 0.0 | 0.0 | 32.8 | 31.2 | 93.2 | 1.07 |  | 0.50 |
|  | ca17 | Pn | 31.8 | 0.0 | 31.0 | 0.0 | 31.8 | 94.7 | 1.11 | 0.48 |  |
|  | ca18 | Pn | 31.5 | 0.0 | 31.4 | 0.0 | 31.3 | 94.1 | 1.12 | 0.49 |  |
|  | ca19 | Pn | 31.5 | 0.0 | 31.4 | 0.0 | 32.3 | 95.2 | 1.09 | 0.49 |  |
|  | sa13 | Pn | 35.5 | 0.5 | 28.0 | 0.0 | 33.7 | 97.8 | 1.07 | 0.43 |  |
|  | sa15 | Pn | 32.7 | 0.5 | 32.2 | 0.0 | 32.8 | 98.2 | 1.12 | 0.48 |  |
| 19-11T | od1 | Po | 62.3 | n/a | 0.0 | 0.0 | 36.9 | 99.2 | 0.97 |  |  |
| mantle-gabbro contact | od2 | Po | 62.4 | n/a | 0.0 | 0.0 | 36.7 | 99.2 | 0.98 |  |  |
|  | od5 | Po | 62.8 | n/a | 0.0 | 0.0 | 37.3 | 100.2 | 0.97 |  |  |
|  | odn1 | Po | 60.9 | n/a | 0.0 | 0.0 | 38.1 | 99.0 | 0.92 |  |  |
|  | odn2 | Po | 62.4 | n/a | 0.0 | 0.0 | 37.1 | 99.5 | 0.97 |  |  |
|  | sa1c | Po | 61.3 | 0.0 | 0.0 | 0.0 | 38.1 | 99.4 | 0.92 |  |  |
|  | sa2 | Po | 63.3 | 0.0 | 0.0 | 0.0 | 36.3 | 99.5 | 1.00 |  |  |
|  | sa3 | Po | 60.9 | 0.0 | 0.0 | 0.0 | 36.7 | 97.6 | 0.95 |  |  |
|  | m2sa1 | Po | 57.3 | 0.0 | 0.0 | 0.0 | 40.7 | 98.0 | 0.81 |  |  |
|  | m2sa2 | Po | 57.8 | 0.0 | 0.0 | 0.0 | 37.9 | 95.7 | 0.88 |  |  |
|  | m2sb1 | Po | 56.5 | 0.0 | 0.0 | 0.0 | 35.9 | 92.3 | 0.90 |  |  |
|  | m2sb3 | Po | 58.6 | 0.0 | 0.0 | 0.0 | 40.1 | 98.7 | 0.84 |  |  |
|  | m2sc | Po | 59.1 | 0.0 | 0.0 | 0.0 | 39.8 | 98.9 | 0.85 |  |  |
|  | m2sd1 | Po | 58.9 | 0.0 | 0.0 | 0.0 | 38.0 | 96.9 | 0.89 |  |  |
|  | m2sd2 | Po | 57.2 | 0.0 | 0.0 | 0.0 | 38.1 | 95.3 | 0.86 |  |  |
|  | m2sg1 | Po | 58.1 | 0.0 | 0.0 | 0.0 | 36.5 | 94.7 | 0.91 |  |  |
|  | m2sg2 | Po | 60.7 | 0.0 | 0.0 | 0.0 | 39.6 | 100.3 | 0.88 |  |  |
| 21-7 | ca1 | Po | 58.4 | 0.0 | 0.0 | 0.0 | 36.3 | 94.7 | 0.93 |  |  |
| mantle-gabbro contact | ca2 | Pn | 37.4 | 0.8 | 25.9 | 0.0 | 30.9 | 95.1 | 1.17 | 0.40 |  |
|  | ca7 | Po | 59.3 | 0.0 | 0.0 | 0.0 | 38.7 | 98.0 | 0.88 |  |  |
|  | ca8 | Po | 58.4 | 0.0 | 0.0 | 0.0 | 39.9 | 98.3 | 0.84 |  |  |

| Sample No. | | Mineral[a] | Fe | Co | Ni | Cu | S | Total | Me/S[e] | Ni/(Ni+Fe)[e] | Cu/(Cu+Fe)[e] |
|---|---|---|---|---|---|---|---|---|---|---|---|
| | cb3 | Ccp | 29.6 | 0.0 | 0.5 | 34.9 | 33.6 | 98.6 | 1.04 | | 0.51 |
| | cb4 | Po | 60.3 | 0.0 | 0.0 | 0.0 | 37.5 | 97.8 | 0.92 | | |
| | cb5 | Po | 61.3 | 0.0 | 0.0 | 0.0 | 36.7 | 98.0 | 0.96 | | |
| | cb8 | Pn | 32.9 | 2.5 | 29.6 | 0.0 | 31.7 | 96.7 | 1.15 | 0.46 | |
| | cb9 | Po | 59.4 | 0.0 | 0.0 | 0.0 | 39.9 | 99.3 | 0.86 | | |
| | cb14 | Po | 59.4 | 0.0 | 0.0 | 0.0 | 37.4 | 96.7 | 0.91 | | |
| | cb15 | Po | 59.3 | 0.0 | 0.0 | 0.0 | 37.6 | 97.0 | 0.91 | | |
| | cb16 | Po | 59.8 | 0.0 | 0.0 | 0.0 | 38.0 | 97.9 | 0.90 | | |
| | cb23 | Ccp | 30.8 | 0.0 | 0.0 | 37.6 | 32.1 | 100.5 | 1.14 | | 0.52 |
| | cb24 | Po | 60.6 | 0.0 | 0.0 | 0.0 | 36.6 | 97.2 | 0.95 | | |
| | cb25 | Po | 62.0 | 0.0 | 0.0 | 0.0 | 37.0 | 99.0 | 0.96 | | |
| | cb26 | Po | 54.8 | 0.0 | 0.0 | 0.0 | 41.6 | 96.4 | 0.76 | | |
| | cb27 | Pn | 41.3 | 0.7 | 22.6 | 0.0 | 32.8 | 97.4 | 1.11 | 0.34 | |
| | cb29 | Po | 58.7 | 0.0 | 0.3 | 0.0 | 42.8 | 101.8 | 0.79 | | |
| | cb30 | Pn | 35.7 | 1.4 | 29.2 | 0.0 | 32.5 | 98.8 | 1.14 | 0.44 | |
| | cb31 | Po | 61.1 | 0.0 | 0.0 | 0.0 | 40.2 | 101.3 | 0.87 | | |
| | cc19 | Po | 60.2 | 0.0 | 0.0 | 0.0 | 37.1 | 97.2 | 0.93 | | |
| | cc20 | Po | 56.4 | 0.0 | 0.0 | 0.0 | 38.5 | 95.0 | 0.84 | | |
| | cc22 | Po | 60.8 | 0.0 | 0.0 | 0.0 | 36.3 | 97.1 | 0.96 | | |
| | cc23 | Pn | 37.4 | 1.5 | 24.3 | 0.0 | 32.0 | 95.3 | 1.11 | 0.38 | |
| | na1 | Viol | 24.3 | 1.2 | 27.7 | 0.0 | 40.4 | 93.6 | 0.74 | 0.52 | |
| | of1 | Pn | 39.4 | 1.2 | 24.0 | 0.0 | 31.6 | 96.2 | 1.15 | 0.37 | |
| | of2 | Po | 61.9 | 0.0 | 0.0 | 0.0 | 36.0 | 97.9 | 0.99 | | |
| | og1 | Pn | 25.0 | 0.8 | 38.0 | 0.0 | 31.3 | 95.1 | 1.14 | 0.59 | |
| | og2 | Pn | 26.3 | 0.9 | 37.8 | 0.0 | 31.7 | 96.7 | 1.14 | 0.58 | |
| | oh1 | Po | 61.2 | 0.0 | 0.0 | 0.0 | 36.2 | 97.4 | 0.97 | | |
| | oi1 | Po | 61.5 | 0.0 | 0.0 | 0.0 | 35.5 | 97.0 | 0.99 | | |
| | oi2 | Pn | 40.7 | 1.2 | 24.7 | 0.0 | 32.9 | 99.5 | 1.14 | 0.37 | |
| | cj1 | Po | 62.8 | 0.0 | 0.0 | 0.0 | 35.5 | 98.3 | 1.02 | | |
| | cj2 | Po | 61.6 | 0.0 | 0.0 | 0.0 | 36.2 | 97.8 | 0.98 | | |
| | cj3 | Po | 61.0 | 0.0 | 0.0 | 0.0 | 35.0 | 96.0 | 1.00 | | |
| | cj4 | Pn | 33.9 | 8.1 | 21.3 | 0.0 | 32.3 | 95.6 | 1.10 | 0.37 | |
| 21-9A | cb1 | Pn | 33.7 | n/a | 31.7 | 0.0 | 32.7 | 98.1 | 1.12 | 0.47 | |
| Pl harzburgite | cb2 | Pn | 32.4 | n/a | 31.2 | 0.0 | 33.4 | 97.0 | 1.07 | 0.48 | |
| | ccn1 | Pn | 31.3 | 1.5 | 32.3 | n/a | 33.3 | 98.5 | 1.10 | 0.50 | |

| Sample No. | | Mineral[a] | Fe | Co | Ni | Cu | S | Total | Me/S[e] | Ni/(Ni+Fe)[e] | Cu/(Cu+Fe)[e] |
|---|---|---|---|---|---|---|---|---|---|---|---|
| | ccn2 | Pn | 32.5 | 1.3 | 31.5 | n/a | 33.6 | 99.0 | 1.09 | 0.48 | |
| | s1 | Pn | 31.1 | 2.2 | 31.7 | n/a | 31.6 | 96.7 | 1.15 | 0.49 | |
| | cd1 | Pn | 30.3 | 1.1 | 32.2 | n/a | 33.5 | 97.1 | 1.06 | 0.50 | |
| | cji | Pn | 29.8 | n/a | 33.5 | 0.0 | 33.3 | 96.6 | 1.06 | 0.52 | |
| | ckm | Pn | 31.3 | n/a | 32.8 | 0.0 | 33.0 | 97.1 | 1.09 | 0.50 | |
| | ckn | Pn | 32.0 | n/a | 33.4 | 0.0 | 33.1 | 98.5 | 1.11 | 0.50 | |
| | ckl | Pn | 31.4 | n/a | 32.1 | 0.0 | 32.3 | 95.8 | 1.10 | 0.49 | |
| | u1 | Pn | 30.2 | n/a | 33.2 | 0.0 | 32.5 | 95.9 | 1.09 | 0.51 | |
| 21-GB | cg1 | Mi | 0.3 | n/a | 62.4 | 0.0 | 33.9 | 96.7 | 1.01 | 1.00 | |
| olivine gabbro vein | cg2 | Gs | 0.5 | n/a | 66.0 | 0.0 | 31.6 | 98.1 | 1.15 | 0.99 | |
| | sk1 | Hz | 0.6 | n/a | 71.7 | 0.0 | 25.9 | 98.2 | 1.53 | 0.99 | |
| | sk2 | Hz | 0.6 | n/a | 72.1 | 0.0 | 26.7 | 99.3 | 1.49 | 0.99 | |
| | sk3 | Hz | 0.7 | n/a | 71.9 | 0.0 | 26.3 | 98.8 | 1.51 | 0.99 | |
| | st | Hz | 0.3 | n/a | 72.3 | 0.0 | 26.5 | 99.1 | 1.50 | 0.99 | |
| 21-9T | sw1 | Hz | 0.5 | 0.0 | 71.9 | n/a | 26.1 | 98.5 | 1.52 | 0.99 | |
| mantle-gabbro contact | sw2 | Hz | 0.6 | 0.0 | 71.6 | n/a | 26.3 | 98.5 | 1.50 | 0.99 | |
| | sw3 | Hz | 0.4 | 0.0 | 71.8 | n/a | 26.8 | 99.0 | 1.47 | 0.99 | |
| | cje | Pn | 30.9 | n/a | 31.8 | 0.0 | 32.9 | 95.5 | 1.07 | 0.49 | |
| | cjg | Pn | 27.5 | n/a | 40.1 | 0.0 | 32.6 | 100.2 | 1.15 | 0.58 | |
| | cjg2 | Pn | 27.4 | n/a | 39.6 | 0.0 | 33.4 | 100.4 | 1.12 | 0.58 | |
| | cjh | Pn | 28.8 | n/a | 34.8 | 0.0 | 31.8 | 95.3 | 1.12 | 0.53 | |
| | cjj | Pn | 29.9 | n/a | 33.6 | 0.0 | 33.1 | 96.6 | 1.07 | 0.52 | |
| | cko | Pn | 33.2 | n/a | 32.2 | 0.0 | 32.4 | 97.9 | 1.13 | 0.48 | |
| | sr | Pn | 26.8 | n/a | 39.4 | 0.0 | 32.7 | 99.0 | 1.13 | 0.58 | |
| | ss | Pn | 30.5 | n/a | 36.2 | 0.0 | 33.1 | 99.8 | 1.13 | 0.53 | |
| 28-9A (Pl harzburgite) | ca2 | Pn | 33.5 | n/a | 33.4[f] | 0.0 | 32.1 | 99.0 | 1.17 | 0.49 | |
| 112-10 | vb12 | Pn | 32.4 | 2.4 | 28.8 | 0.0 | 30.4 | 94.0 | 1.17 | 0.46 | |
| Pl harzburgite | xa5 | Pn | 31.0 | 2.3 | 30.5 | 0.0 | 29.8 | 93.6 | 1.20 | 0.48 | |
| | sa1 | Po | 53.7 | n/a | 0.5 | 0.0 | 39.5 | 93.7 | 0.79 | | |
| | sa3 | Po | 55.6 | n/a | 0.0 | 0.0 | 39.7 | 95.3 | 0.81 | | |
| | sa2 | Po | 55.2 | n/a | 0.0 | 0.0 | 39.8 | 94.9 | 0.80 | | |
| | sa4 | Py | 46.5 | n/a | 0.1 | 0.0 | 47.6 | 94.1 | 0.56 | | |
| | sa5 | Py | 46.9 | n/a | 0.2 | 0.0 | 47.9 | 95.0 | 0.56 | | |

[a] Pn, pentlandite; Po, pyrrhotite; Ccp, chalcopyrite; Hz, heazlewoodite; Viol, violarite; Py, pyrite; Gs, godlevskite; Mi, millerite; Pn(+Ccp), Pn with intergrowths of Ccp; Ccp(+Pn), Ccp with intergrowths of pentlandite

[b] lithology of host rock indicated under sample name

[c] does not include impurities, which occur in 96 of 274 records. Total impurities, mostly Si and Mg, make up >1 wt% in 8 records, but never >2 wt%. They are typically caused by small sizes of analyzed sulfides. The beam interacts with neighbor phases in such a case

[d] n/a – data is not available

[e] molar ratio

[f] we measured this value using LA-ICPMS

## *E. X-ray diffraction diffractograms of the Kane Megamullion silicates*

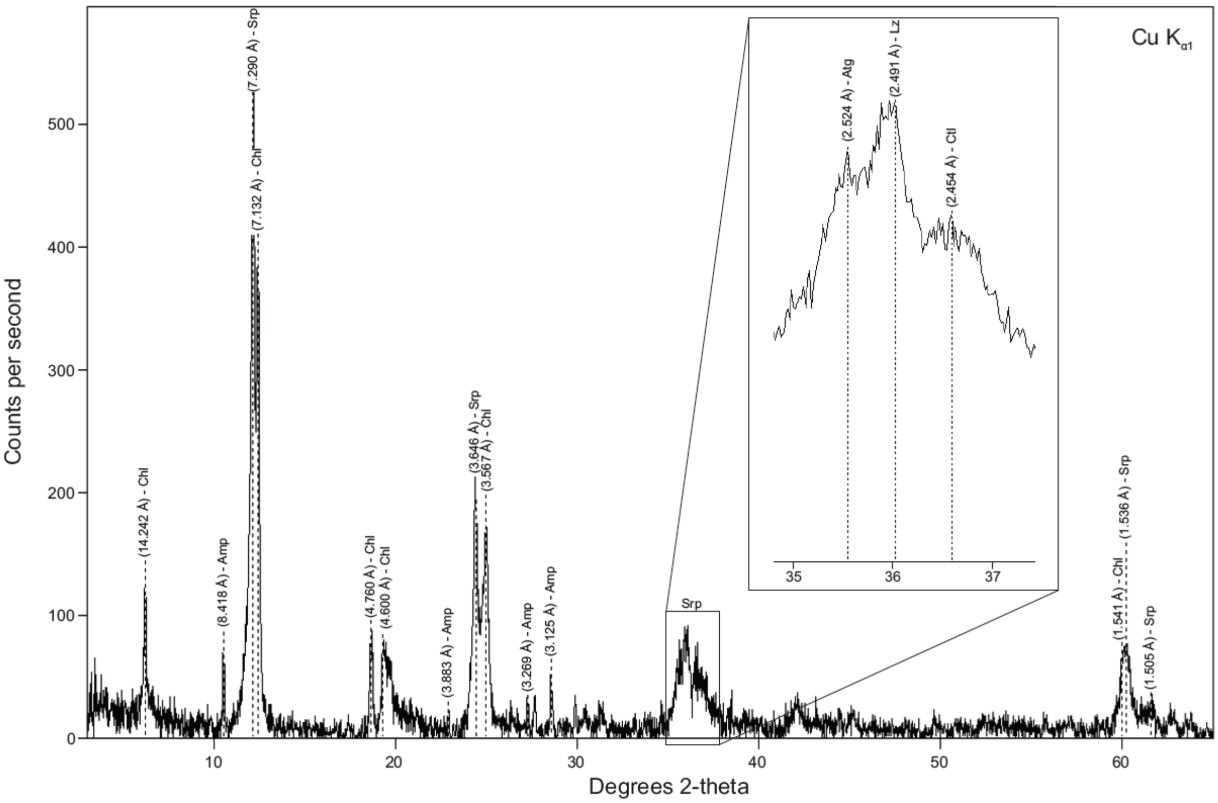

**Fig. E.1.** X-ray diffraction (XRD) diffractogram of subsample 21-9T. Srp – serpentine, Atg – Antigorite, Ctl- chrysotile, Lz- lizardite, Chl – chlorite, Amp- amphibole. Interplanar spacing (d) is given in brackets in Å.

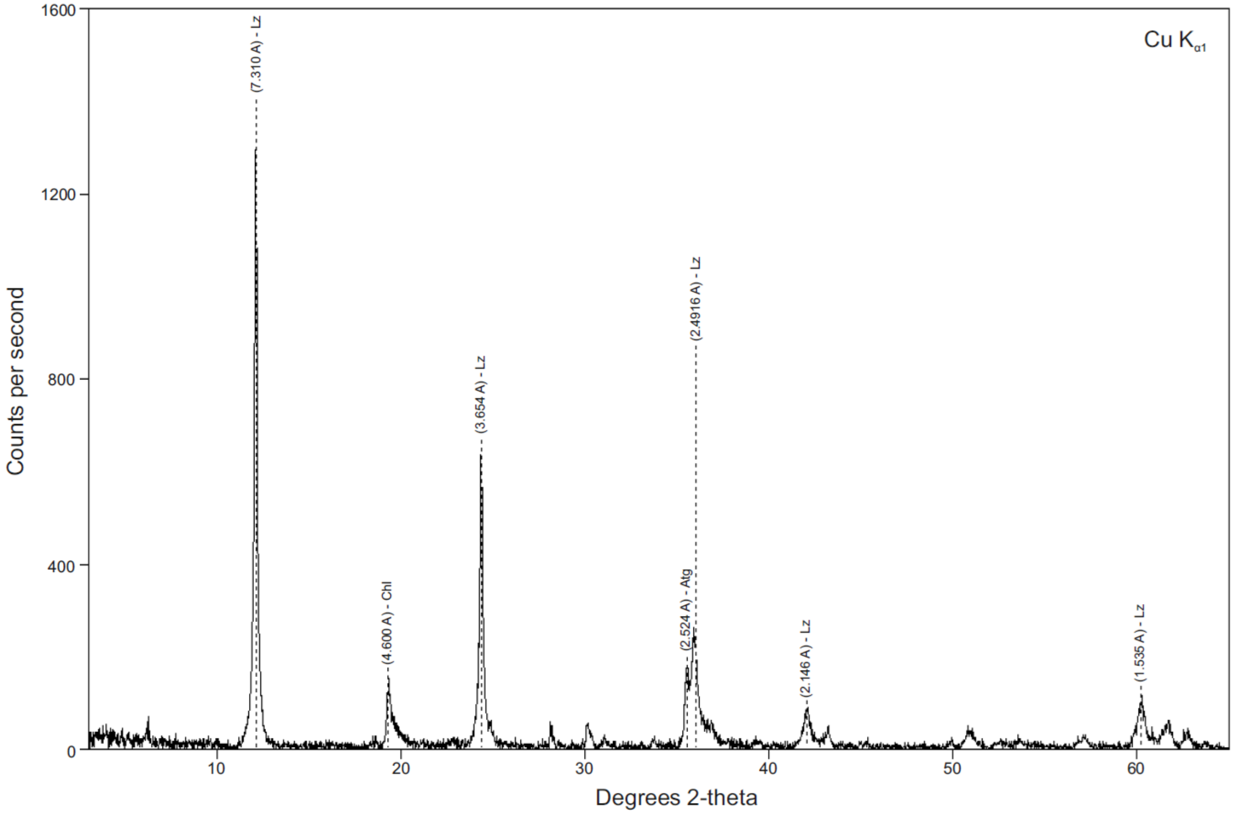

**Fig. E.2.** X-ray diffraction (XRD) diffractogram of subsample 21-9A. Srp – serpentine, Atg – Antigorite, Lz- lizardite, Chl – chlorite. Interplanar spacing (d) is given in brackets in Å.

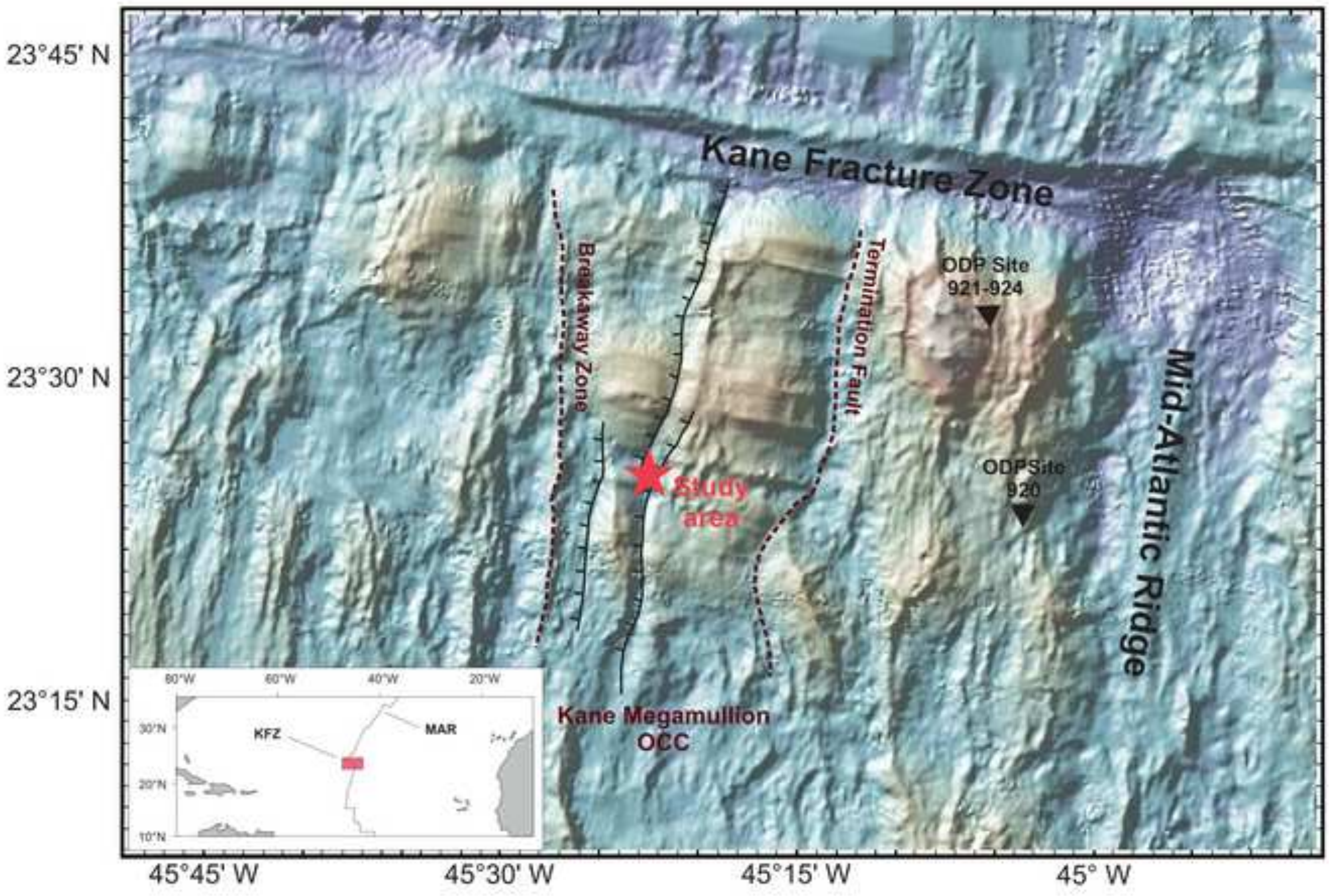
23°45' N
23°30' N
23°15' N
45°45' W
45°30' W
45°15' W
45° W
Kane Fracture Zone
Breakaway Zone
Termination Fault
ODP Site
921-924
ODPSite
920
Study
area
Mid-Atlantic Ridge
Kane Megamullion
OCC
80°W
60°W
40°W
20°W
30°N
20°N
10°N
KFZ
MAR

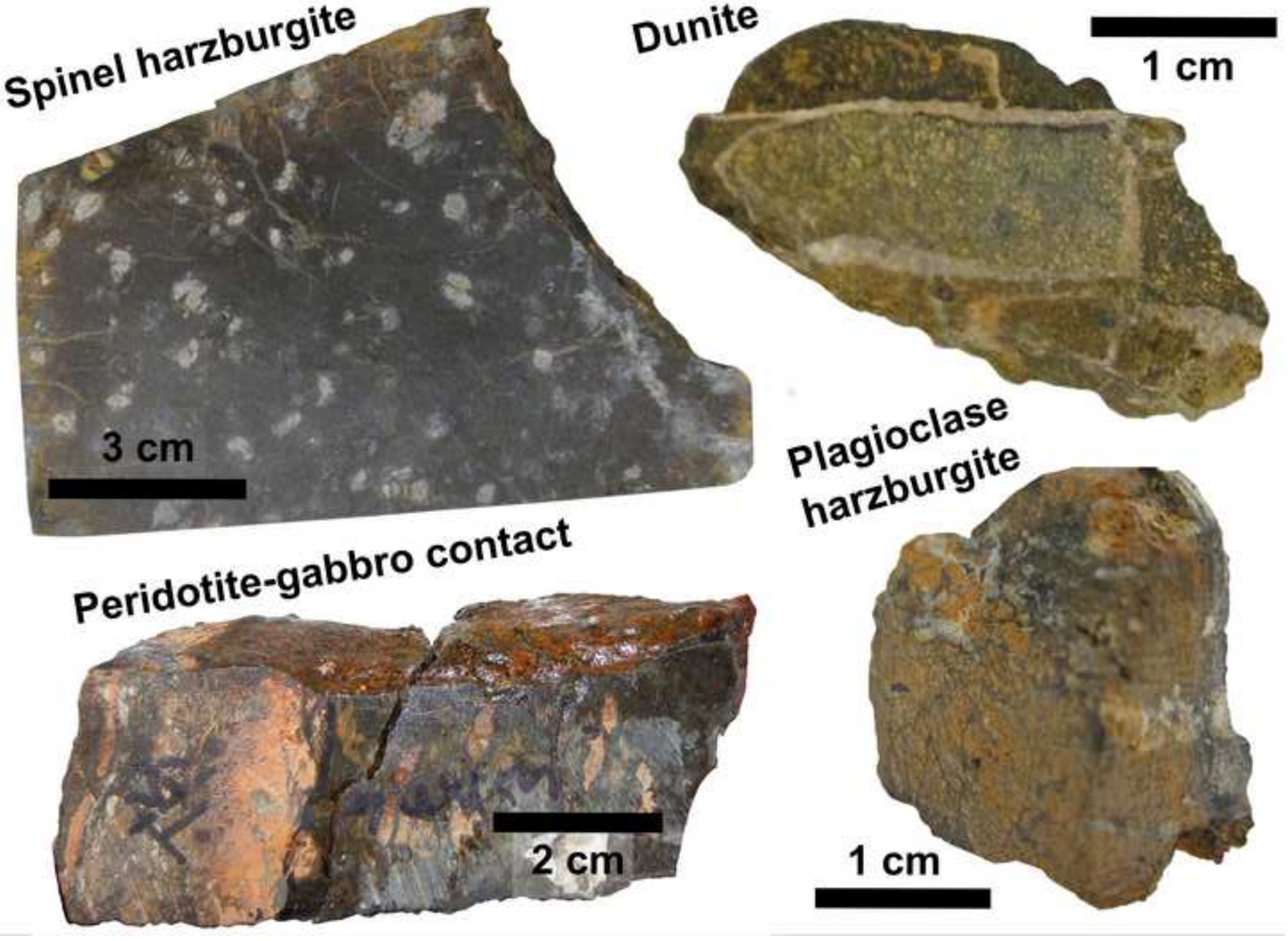
Spinel harzburgite
3 cm
Dunite
1 cm
Plagioclase harzburgite
1 cm
Peridotite-gabbro contact
2 cm

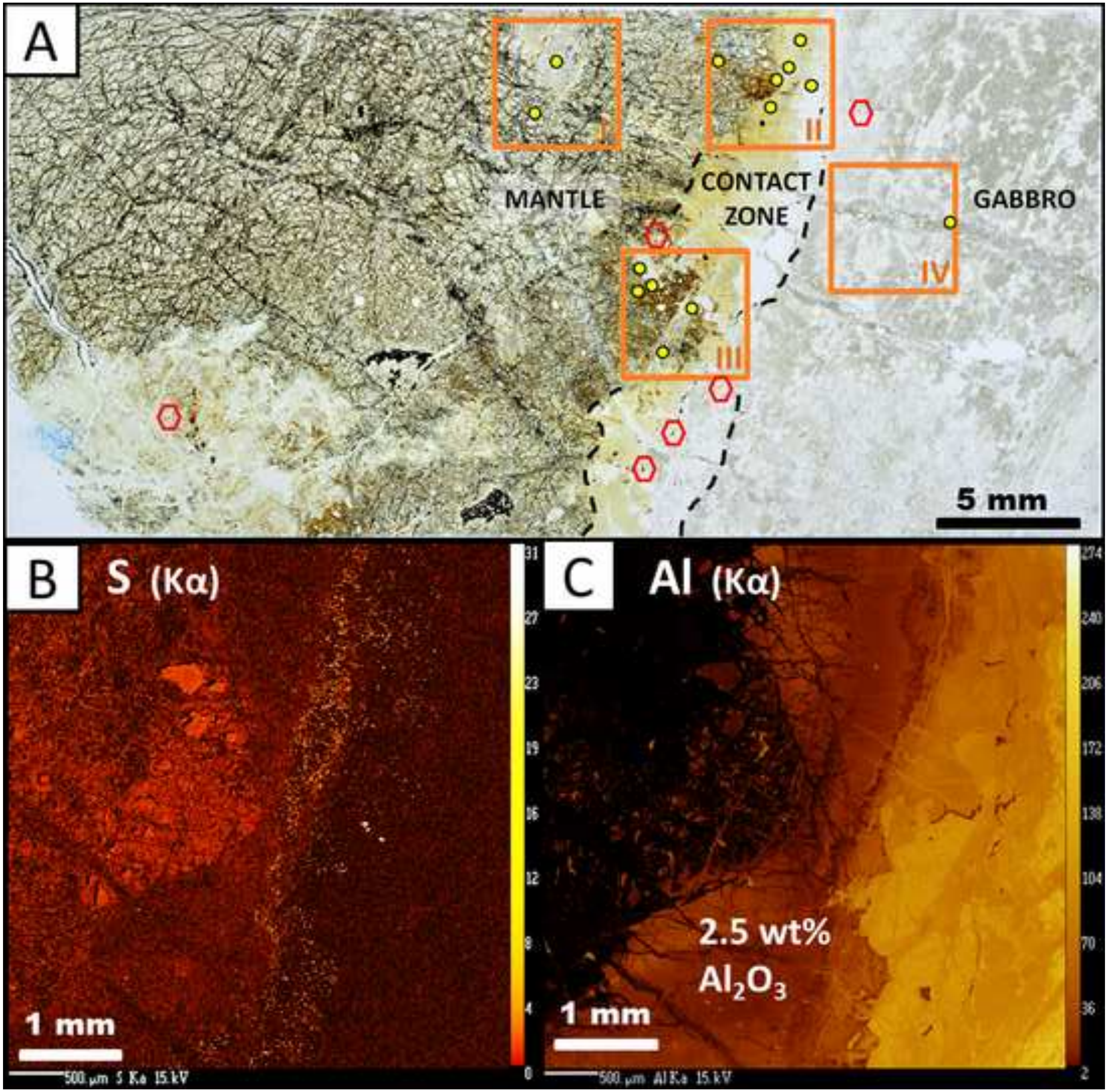
A
I
II
III
IV
MANTLE
CONTACT ZONE
GABBRO
5 mm
B
S (Kα)
1 mm
500 µm S Ka 15 kV
31
27
23
19
16
12
8
4
0
C
Al (Kα)
2.5 wt% $Al_2O_3$
1 mm
500 µm Al Ka 15 kV
274
240
206
172
138
104
70
36
2

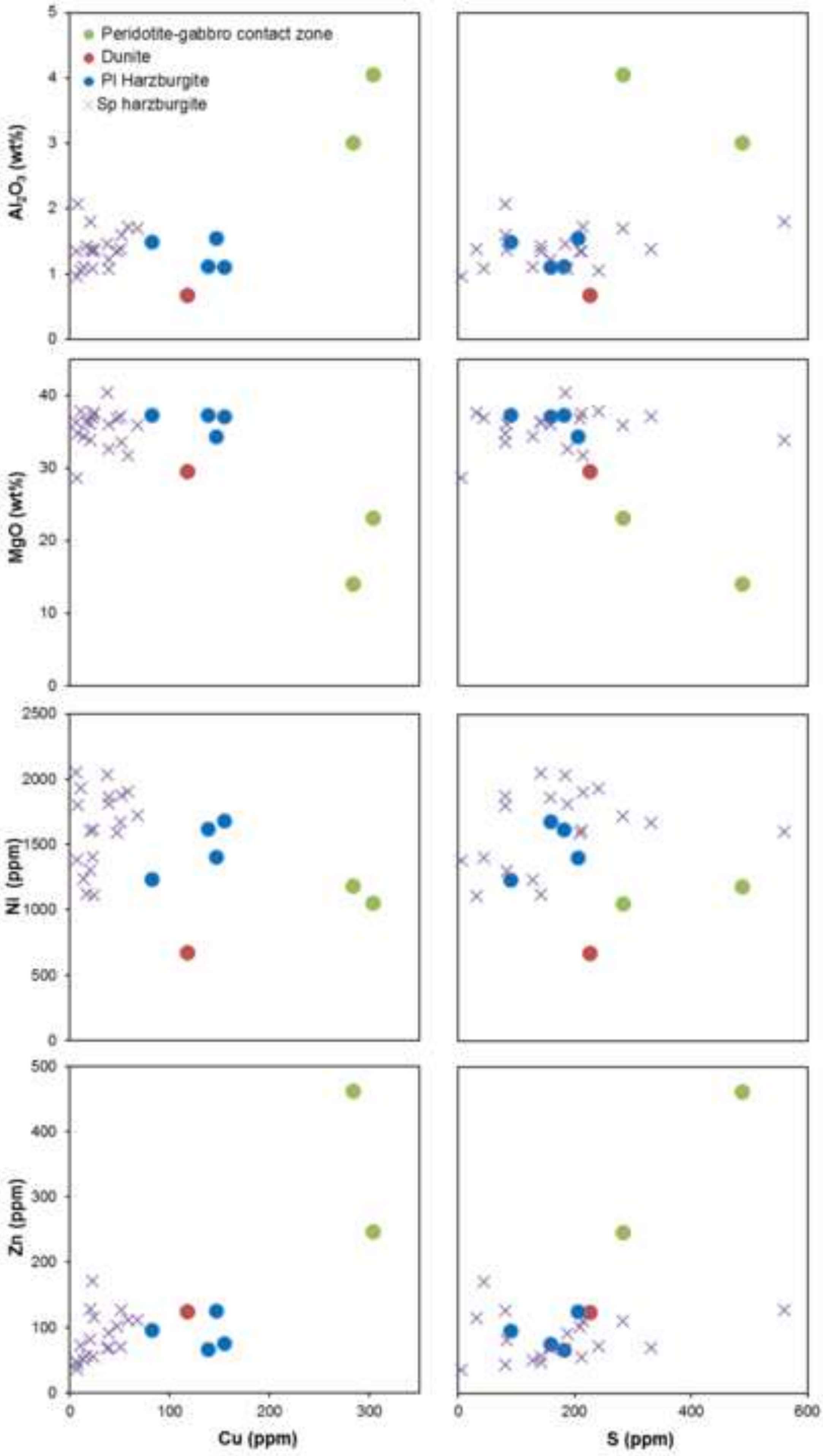
Peridotite-gabbro contact zone
Dunite
Pl Harzburgite
Sp harzburgite
Al2O3 (wt%)
0
1
2
3
4
5
MgO (wt%)
0
10
20
30
40
Ni (ppm)
0
500
1000
1500
2000
2500
Zn (ppm)
0
100
200
300
400
500
0
100
200
300
Cu (ppm)
0
200
400
600
S (ppm)

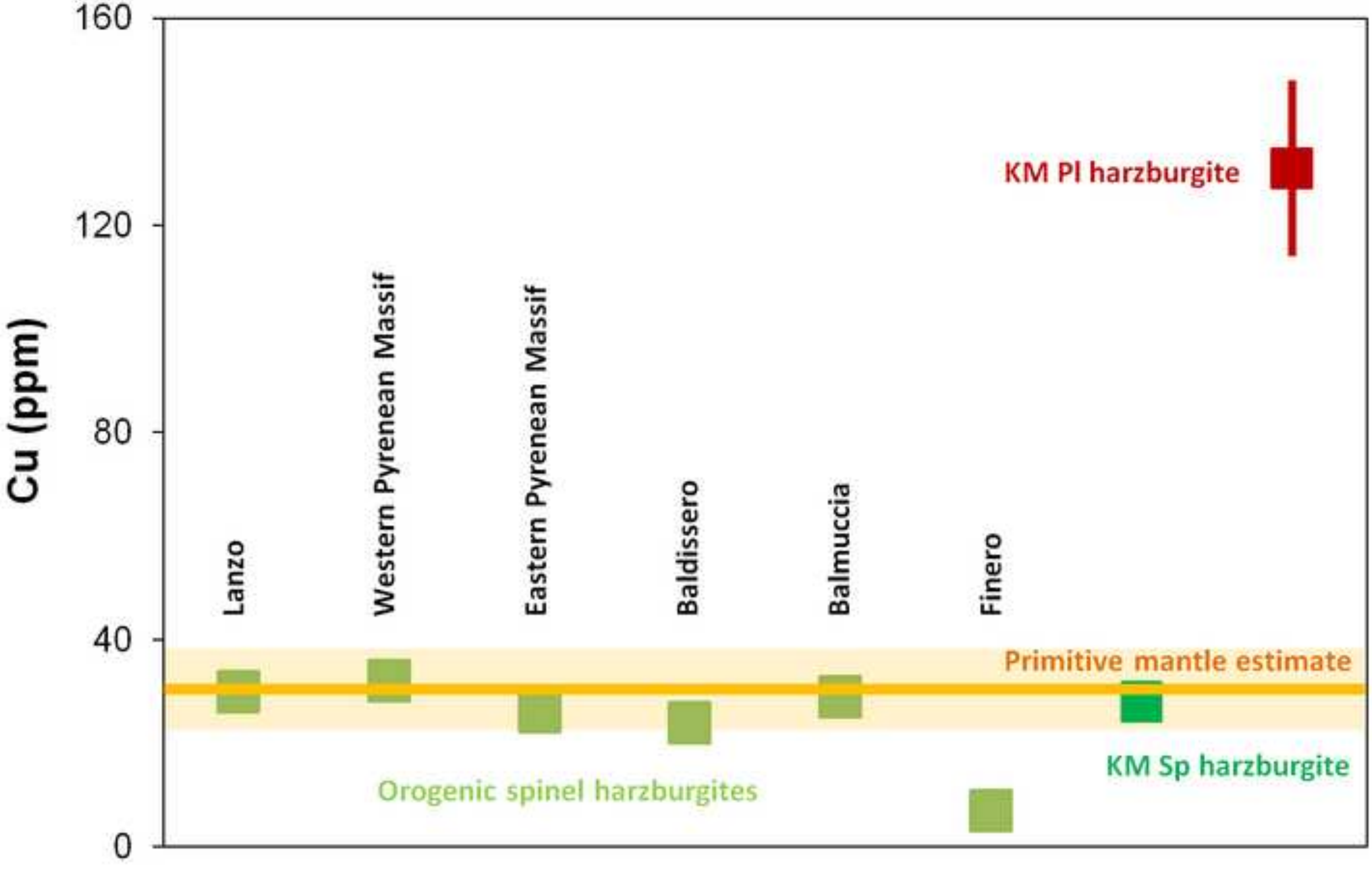
Cu (ppm)
160
120
80
40
0
Lanzo
Western Pyrenean Massif
Eastern Pyrenean Massif
Baldissero
Balmuccia
Finero
KM Pl harzburgite
Primitive mantle estimate
KM Sp harzburgite
Orogenic spinel harzburgites

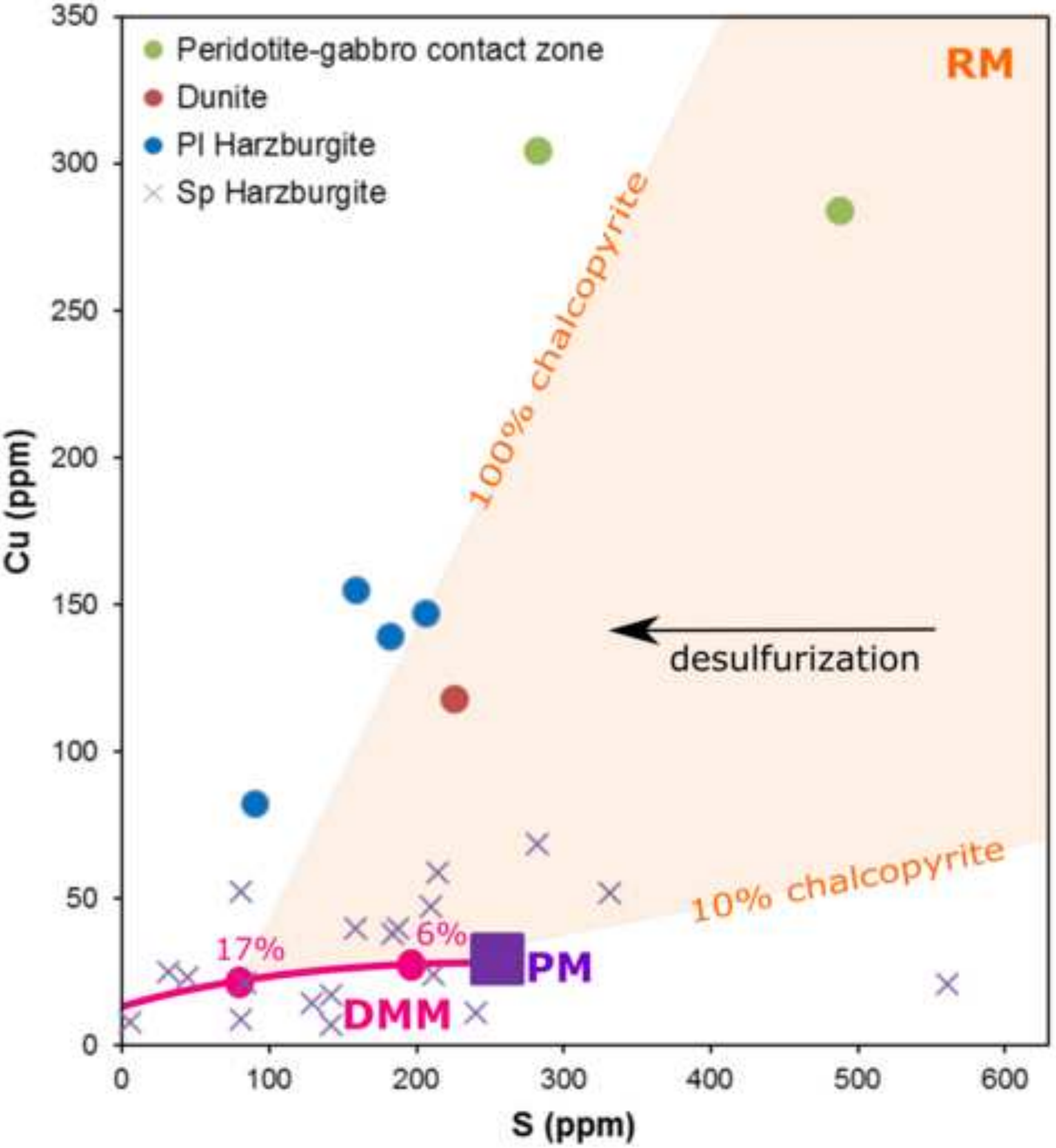
Peridotite-gabbro contact zone
Dunite
Pl Harzburgite
Sp Harzburgite
RM
100% chalcopyrite
10% chalcopyrite
desulfurization
17%
6%
DMM
PM
Cu (ppm)
S (ppm)
0
50
100
150
200
250
300
350
0
100
200
300
400
500
600

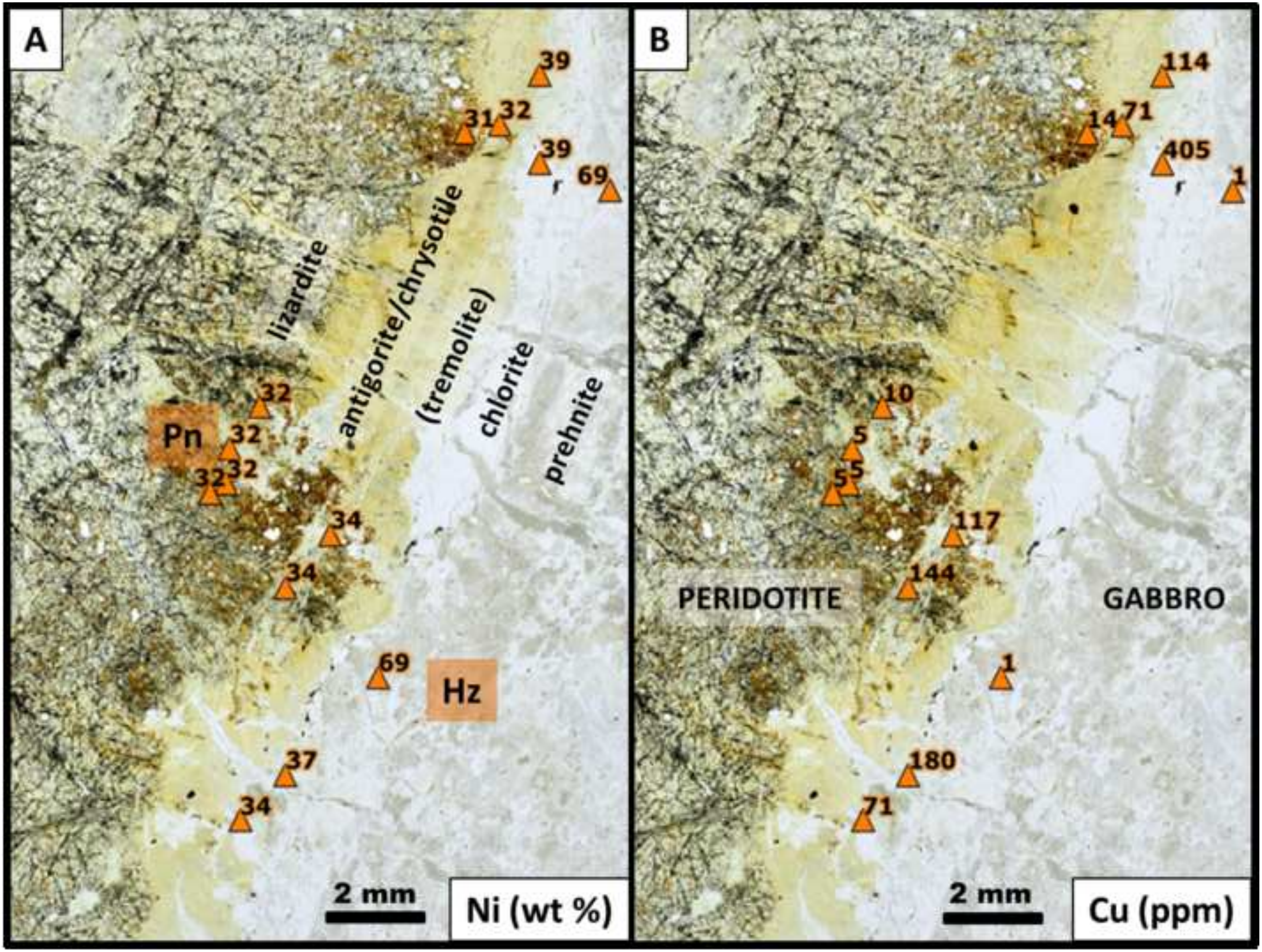
A
39
31
32
39
69
lizardite
antigorite/chrysotile
(tremolite)
chlorite
prehnite
32
Pn
32
32
32
34
34
69
Hz
37
34
2 mm
Ni (wt %)
B
114
14
71
405
1
10
5
5
5
117
144
PERIDOTITE
GABBRO
1
180
71
2 mm
Cu (ppm)

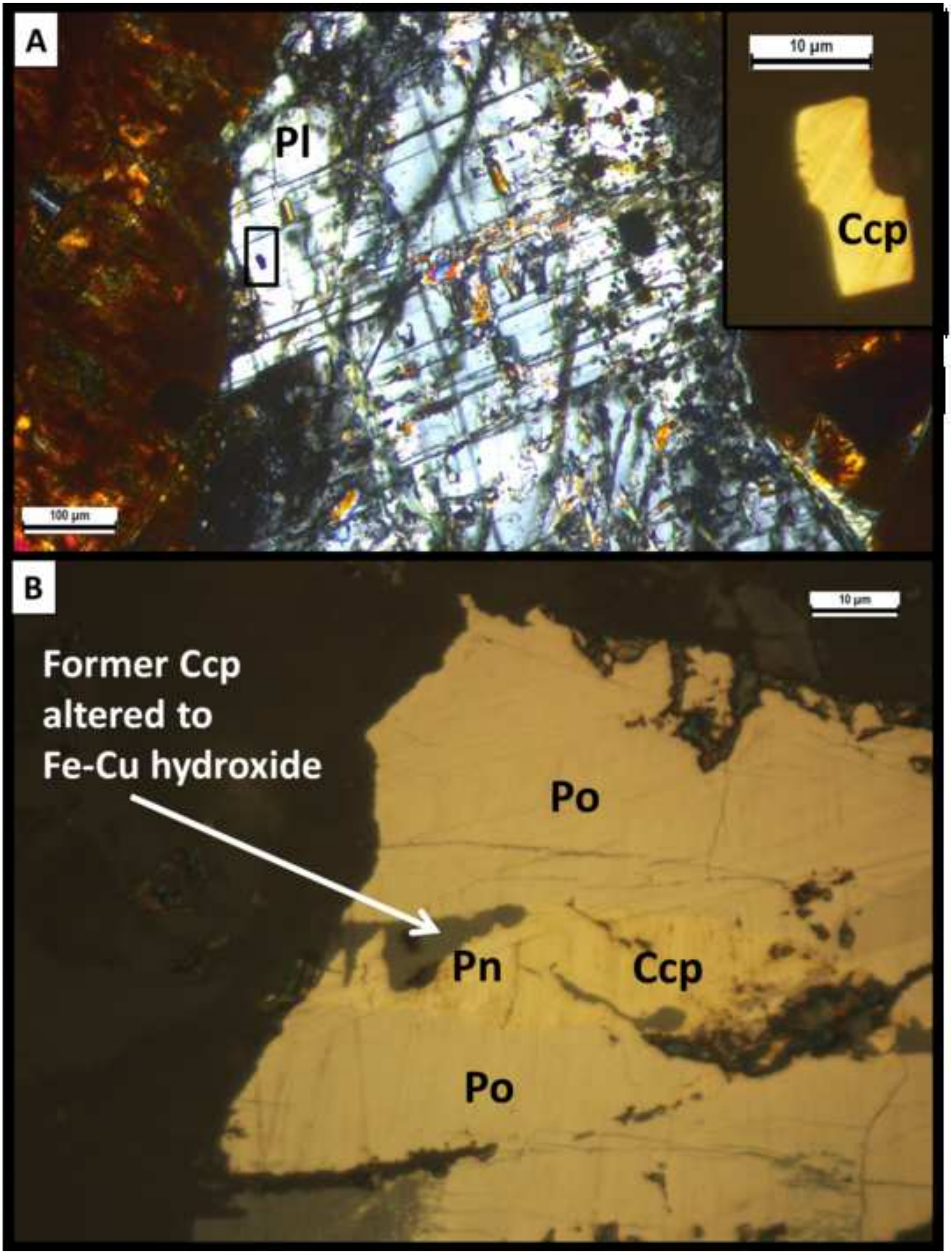
A
Pl
10 µm
Ccp
100 µm
B
10 µm
Former Ccp altered to Fe-Cu hydroxide
Po
Pn
Ccp
Po

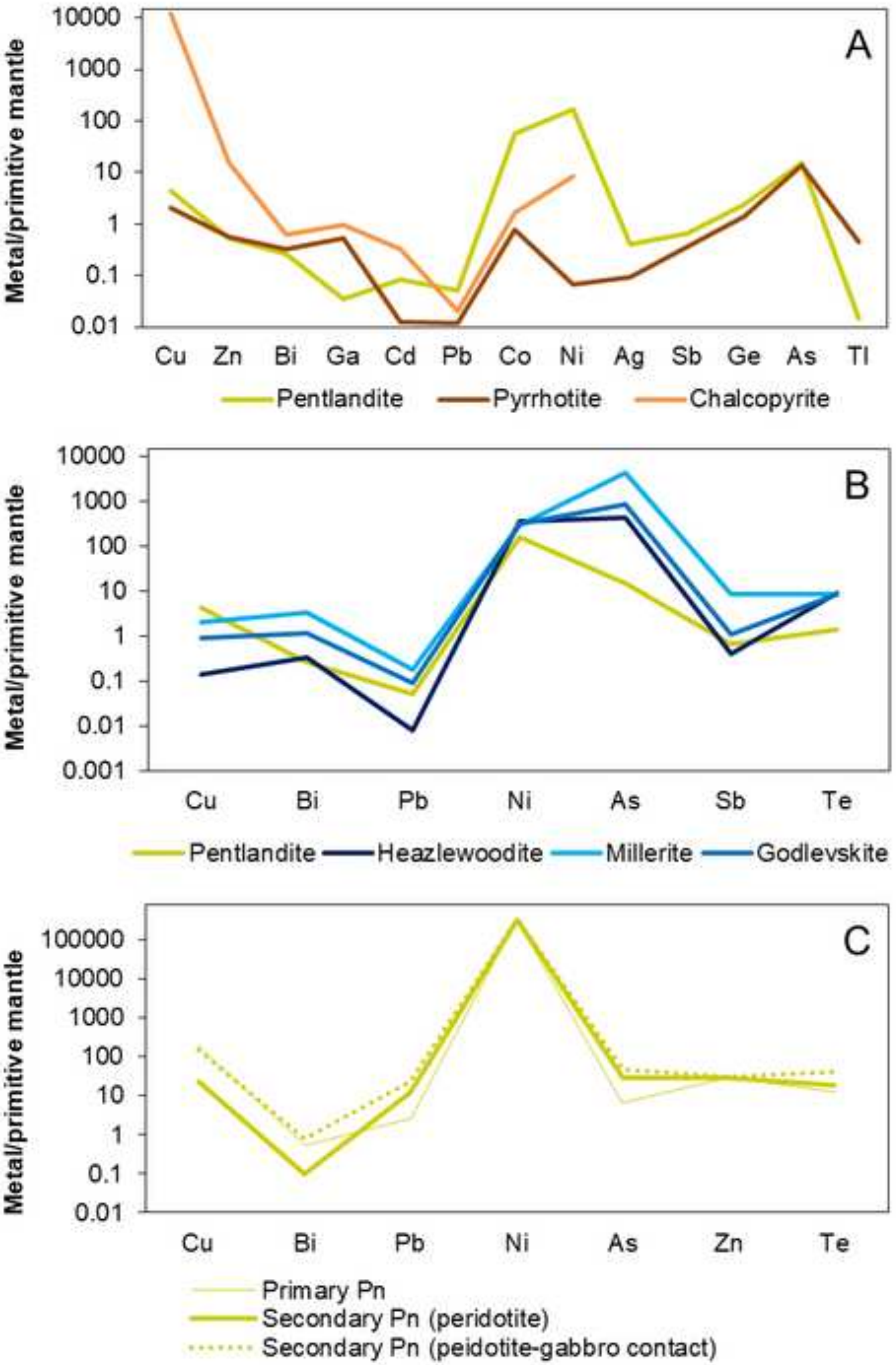
A
Metal/primitive mantle
10000
1000
100
10
1
0.1
0.01
Cu
Zn
Bi
Ga
Cd
Pb
Co
Ni
Ag
Sb
Ge
As
Tl
Pentlandite
Pyrrhotite
Chalcopyrite
B
Metal/primitive mantle
10000
1000
100
10
1
0.1
0.01
0.001
Cu
Bi
Pb
Ni
As
Sb
Te
Pentlandite
Heazlewoodite
Millerite
Godlevskite
C
Metal/primitive mantle
100000
10000
1000
100
10
1
0.1
0.01
Cu
Bi
Pb
Ni
As
Zn
Te
Primary Pn
Secondary Pn (peridotite)
Secondary Pn (peidotite-gabbro contact)

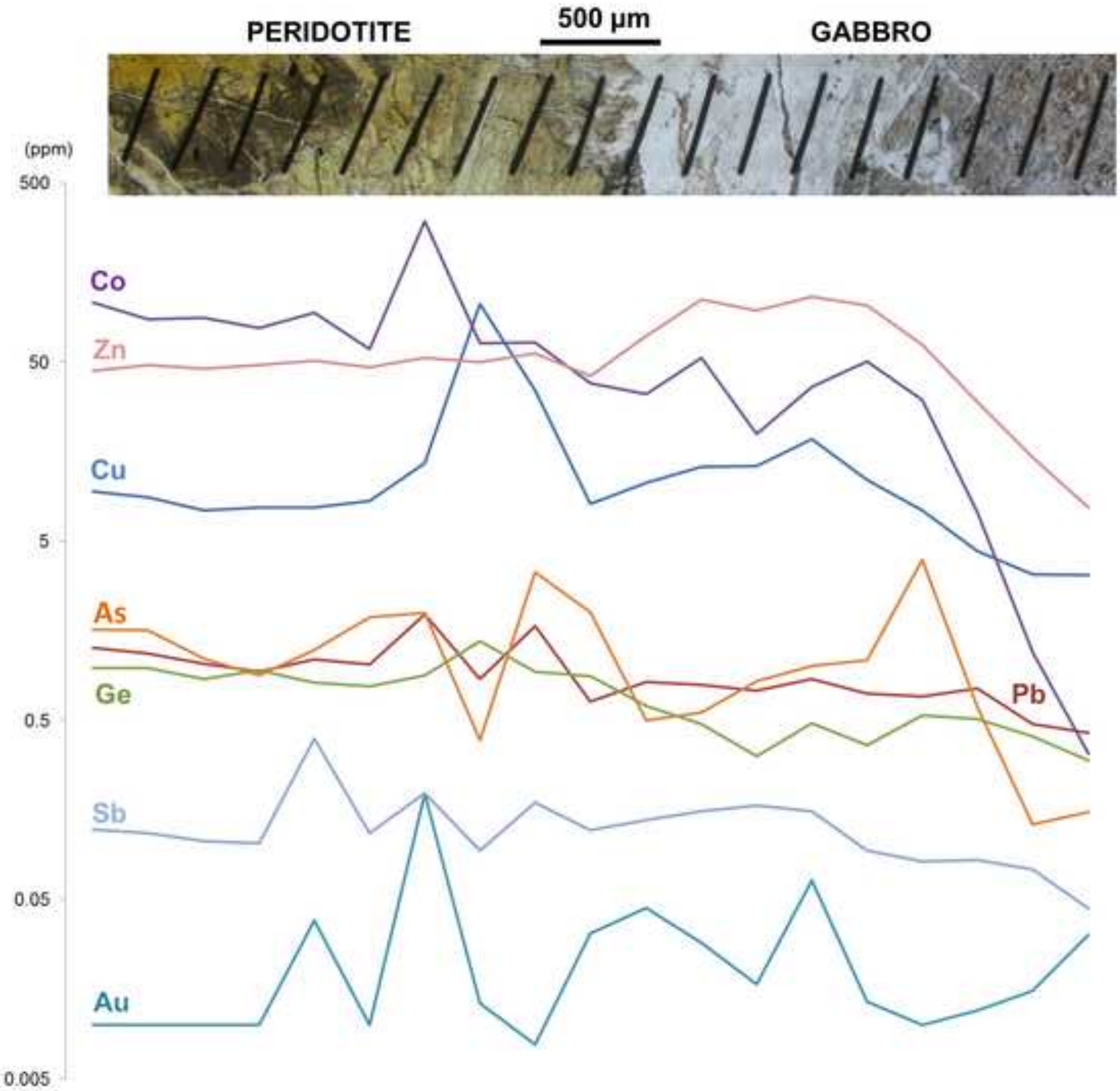

PERIDOTITE
500 µm
GABBRO
(ppm)
500
50
5
0.5
0.05
0.005
Co
Zn
Cu
As
Ge
Pb
Sb
Au

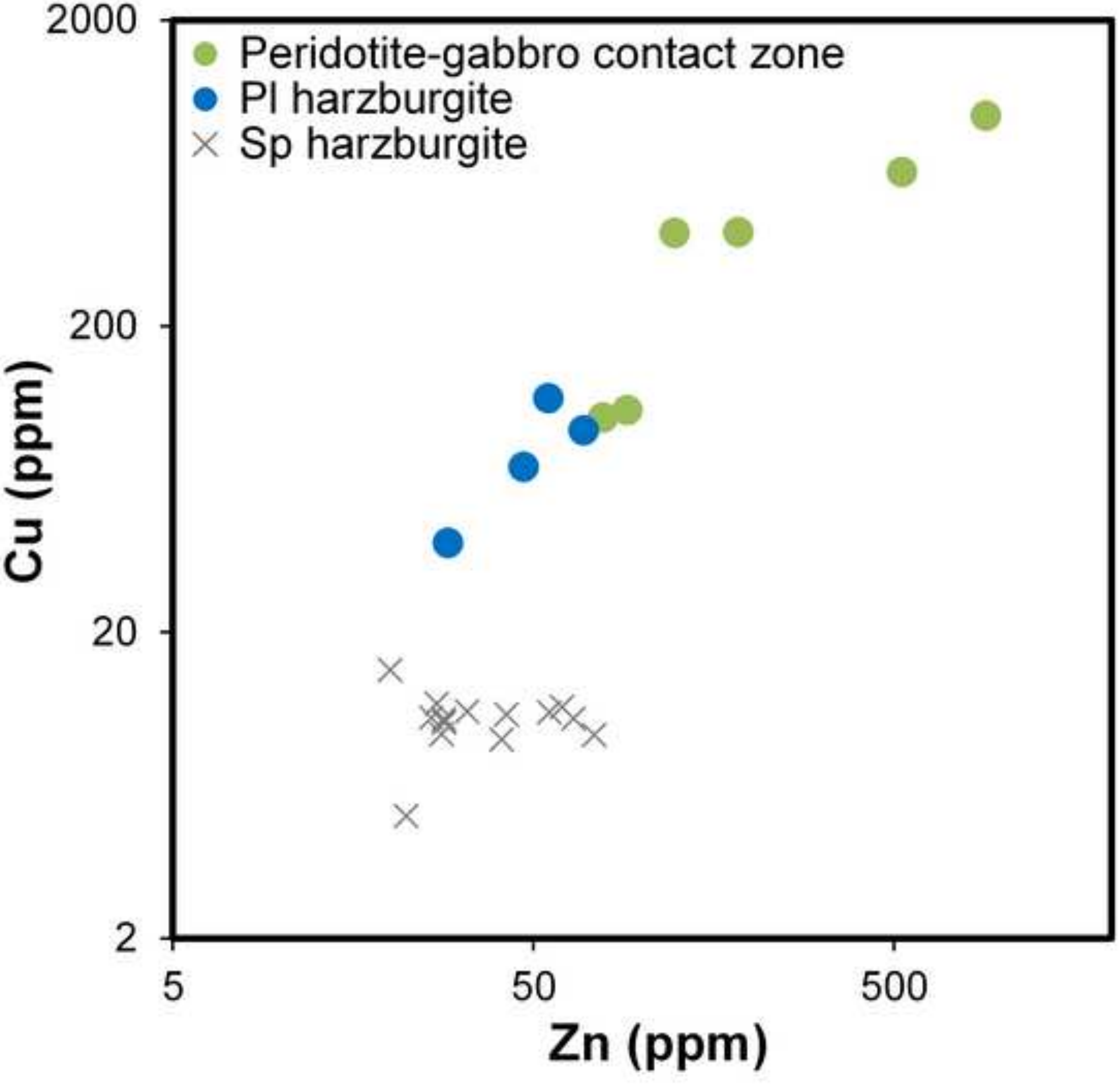
Peridotite-gabbro contact zone
Pl harzburgite
Sp harzburgite
2000
200
20
2
Cu (ppm)
5
50
500
Zn (ppm)

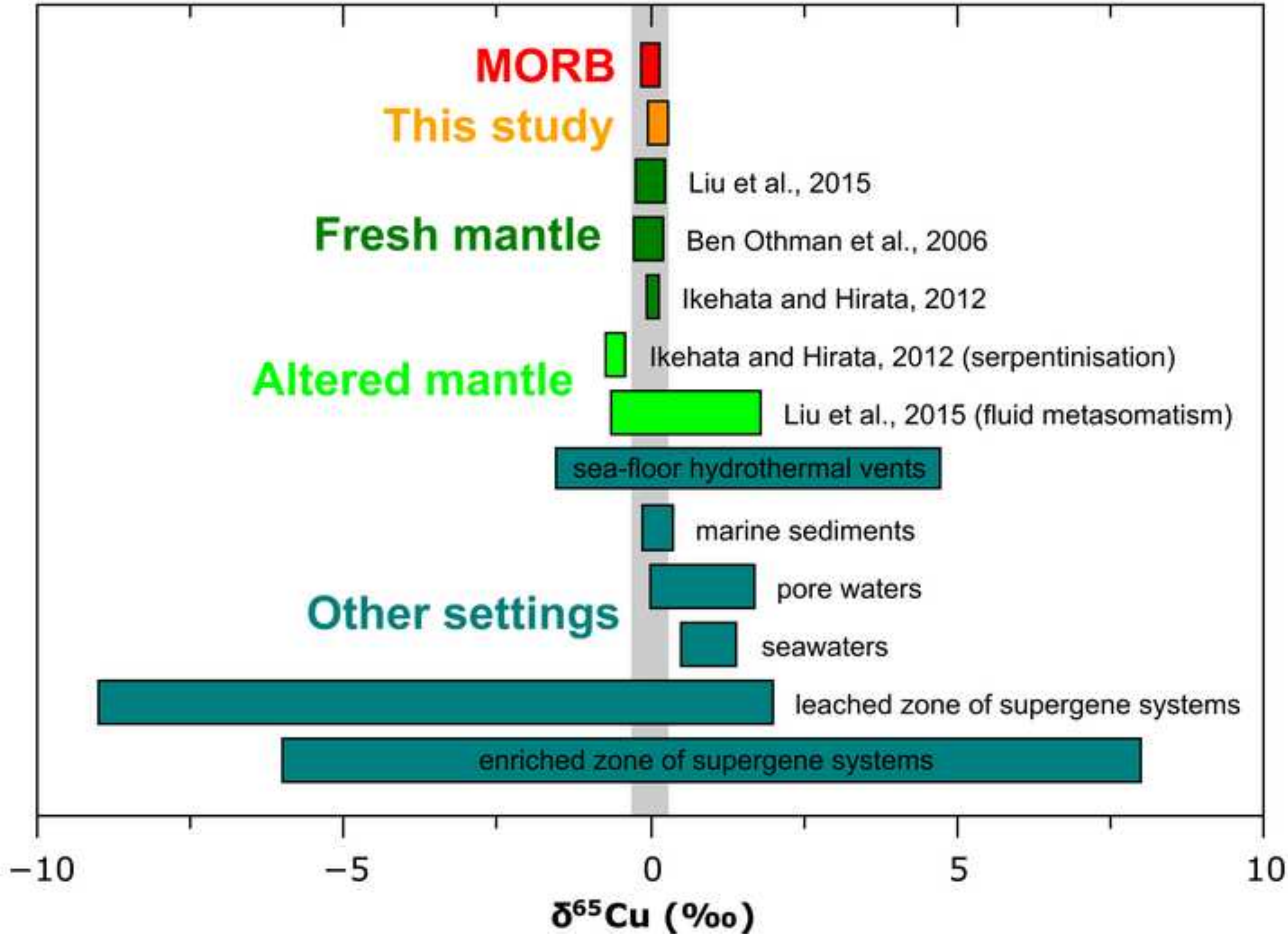
MORB
This study
Liu et al., 2015
Fresh mantle
Ben Othman et al., 2006
Ikehata and Hirata, 2012
Ikehata and Hirata, 2012 (serpentinisation)
Altered mantle
Liu et al., 2015 (fluid metasomatism)
sea-floor hydrothermal vents
marine sediments
pore waters
Other settings
seawaters
leached zone of supergene systems
enriched zone of supergene systems
−10
−5
0
5
10
δ65Cu (‰)